The color of X-rays: Spectral X-ray computed tomography using energy sensitive pixel detectors

Schioppa, E.J.

Publication date
2014
Document Version
Final published version

Link to publication

Citation for published version (APA):
Schioppa, E. J. (2014). *The color of X-rays: Spectral X-ray computed tomography using energy sensitive pixel detectors*. Boxpress.

The color of X-rays

Spectral computed tomography using energy sensitive pixel detectors

Enrico Junior Schioppa

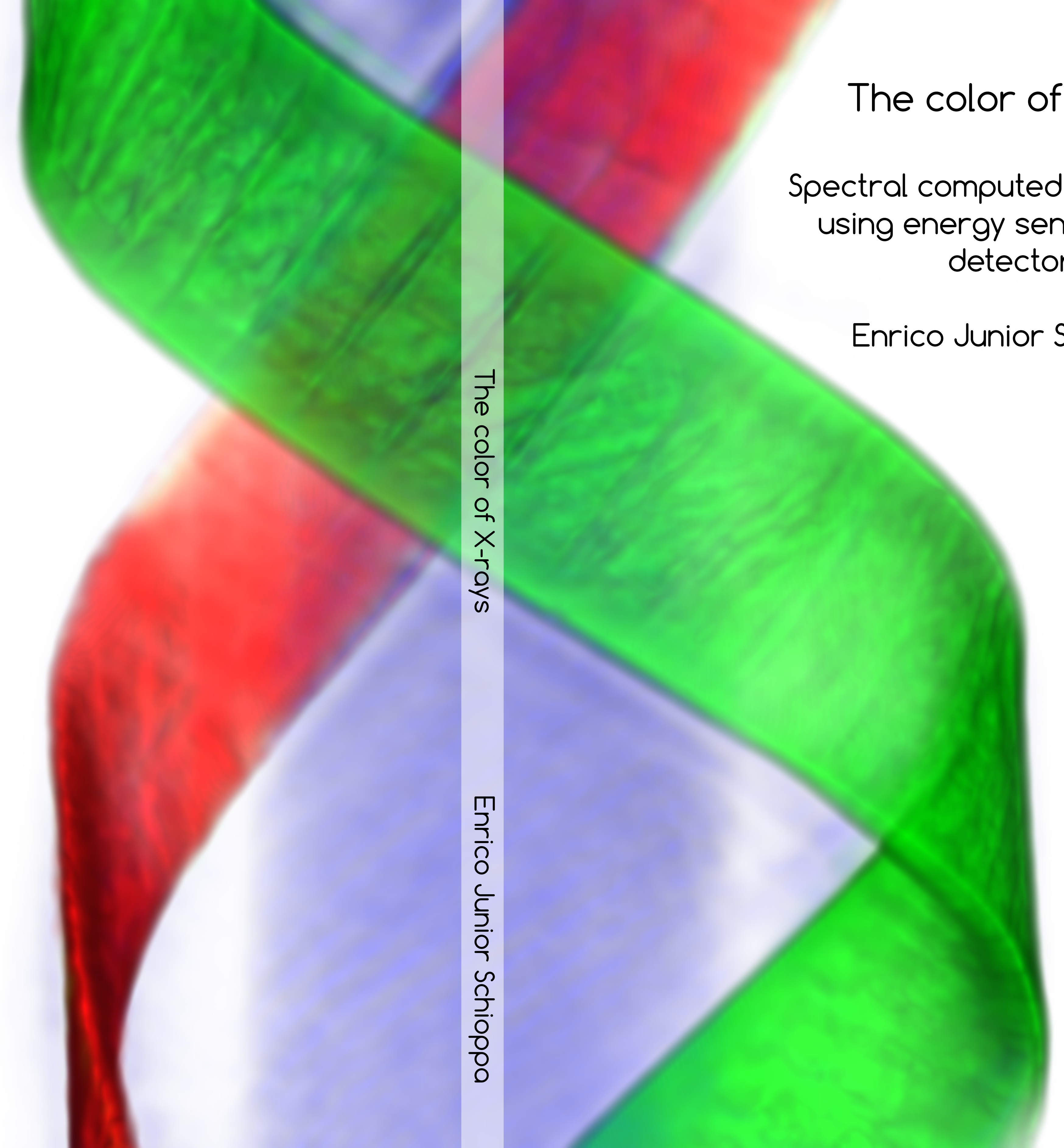

The color of X-rays

Enrico Junior Schioppa

ISBN 978-90-8891-983-1

The color of X-rays

Spectral X-ray computed tomography using energy sensitive pixel detectors

Enrico Junior Schioppa

THE COLOR OF X-RAYS

Spectral X-ray computed tomography using energy sensitive pixel detectors

ACADEMISCH PROEFSCHRIFT

ter verkrijging van de graad van doctor
aan de Universiteit van Amsterdam
op gezag van de Rector Magnificus
prof. dr. D.C. van den Boom
ten overstaan van een door het college voor promoties ingestelde
commissie, in het openbaar te verdedigen in de Aula der
Universiteit
op vrijdag 5 december 2014, te 15:00 uur

door

Enrico Junior Schioppa

geboren te Rome, Italië.

Promotiecommissie:

Promotor: prof. dr. ir. E.N. Koffeman
Co-promotor: dr. J. Visser

Overige Leden: prof. dr. S.C.M. Bentvelsen
dr. A.P. Colijn
dr. E. H.M. Heijne
prof. dr. ir. P.J. de Jong
prof. dr. S.J. de Jong
prof. dr. F.L. Linde
dr. W. Verkerke

Faculteit der Natuurwetenschappen, Wiskunde en Informatica

This work is part of the research program of the Foundation for Fundamental Research on Matter (FOM), which is part of the Netherlands Organization for Scientific Research (NWO). It was carried out at the National Institute for Subatomic Physics (Nikhef) in Amsterdam, the Netherlands. The research has been supported by the Dutch Technology Foundation (STW), which is the applied science division of NWO, and the Technology Programme of the Ministry of Economic Affairs, Project OTP 11956.

ISBN: 978-90-8891-983-1

Cover design by Enrico Junior Schioppa © 2014
Typeset by LaTeX
Printed by: Proefschriftmaken.nl || Uigeverij BOXPress
Published by: Uitgeverij BOXPress, 's-Hertogenbosch

pesa più un litro di paglia o un litro di piombo?[1]

---

[1] Literally, “What is heavier: one liter of straw or one liter of lead?”, a re-elaboration of the riddle “What is heavier: one kilo of straw or one kilo of lead?”. To mean that oftentimes finding the right answer is just a matter of posing the right question.

Contents

Introduction

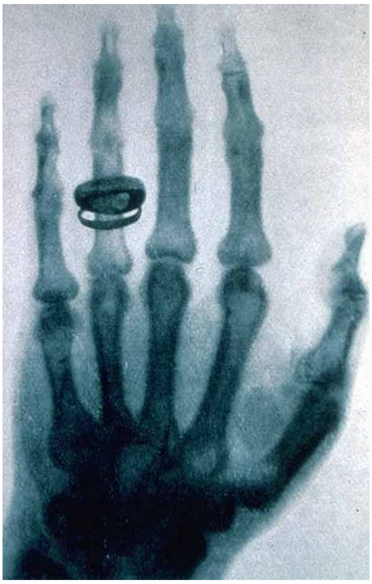

Figure 1: **Radiograph of a hand taken by Wilhelm Röntgen during a public lecture. The grayscale encodes beam intensity: dark = low intensity, light = high intensity.**

Being able to traverse matter, X-rays are a powerful tool to inspect the interior of objects without the need for an invasive intervention. For this reason, since their discovery at the beginning of the 20th century, X-rays are used in several fields of imaging, ranging from medicine to industry. Despite this long history of advancement, further developments of X-ray applications are all but exhausted.

Until very recently, detectors for X-ray radiography were only able to measure one scalar quantity: beam intensity[2]. This gives rise to the grayscale radiographs we are all used to, which in fact are just photon intensity maps (see figure 1).

Although conceptually simple, this approach has made it possible to develop the sophisticated imaging techniques employed today. Among these, Computed Tomography (CT) provides three dimensional X-ray images of objects, reconstructed from a set of two dimensional images taken from

---

[2] Or the total energy released in the detector.

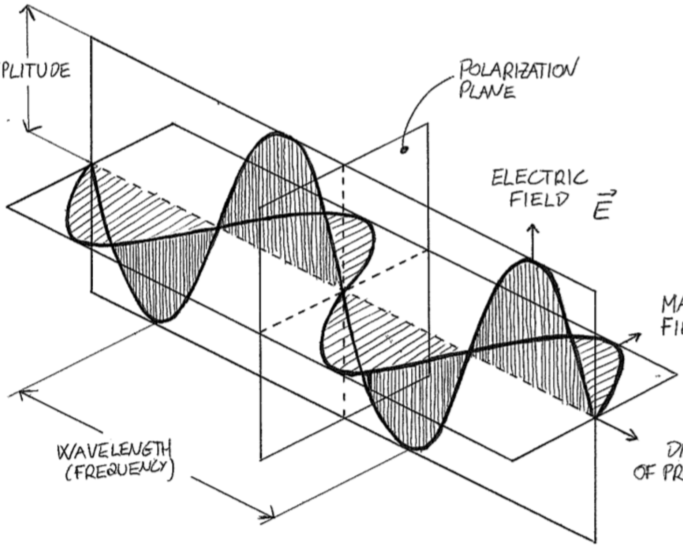

Figure 2: **An electromagnetic wave.**

different directions. Is there a way or a need to improve these already quite sophisticated images?

X-rays are a form of electromagnetic radiation and, as such, an X-ray beam is characterized in terms of not just intensity, but of the usual transverse wave parameters (see figure 2): intensity, frequency, phase and transverse polarization.

When the beam passes through an object, each of these parameters is susceptible to change because of some characteristic interaction with the matter encountered along the path. This means that, when measured, each parameter provides information on the material traversed, thus conveying a complementary piece of knowledge on the object under study.

Irradiating objects (or people!) with ionizing radiation to measure only a fraction of the available information is highly inefficient. This is particularly true in the medical field, where a source of inefficiency is already inherent to the imaging technique itself: of all the X-rays emitted by the source, up to 90%

are usually absorbed by the body of the patient[3].

Leaving aside phase and polarization[4], this thesis will focus on how we can measure the energy of X-ray photons in imaging applications, what we can do with this information and to what kind of improvements this could lead in computed tomography.

Since the absorption properties of matter are strongly dependent on the energy of the radiation, an X-ray spectrum passing through an object gets distorted. In general, low energy photons are absorbed more strongly than high energy photons, and the average energy of the spectrum shifts towards higher values. This effect is thus called beam hardening.

If X-ray imaging systems would make use of monochromatic radiation sources, this effect would not be present. However, up to now, the only sources capable of emitting monochromatic X-ray beams are big and expensive synchrotrons. On the contrary, the majority of imaging applications makes use of X-ray vacuum tubes, characterized by the emission of a continuum spectrum of energies. Even though filtering techniques can be applied, tube spectra always remain polychromatic. As a consequence, when radiographs are taken based only on an intensity measurement, image artifacts appear. In computed tomography, beam hardening effects in the two dimensional images propagate to the 3D reconstruction, giving rise to artifacts that can seriously impair the quality of the image.

With the development of new detector systems, such as the Medipix readout chip for semiconductor pixel sensors, spectral information can be recorded. This information, combined with the high spatial resolution of these detectors, can be exploited to reduce beam hardening effects and achieve material decomposition in X-ray computed tomography. Since different colors can be associated to the different materials which are recognized, spectral CT is often referred to as color CT.

This thesis will present results on spectral computed tomography with semiconductor detectors read out by chips of the Medipix family.

Chapter 1 gives a general overview on computed tomography and it introduces the main image reconstruction techniques used to build a three dimensional representation of the sample from a set of two dimensional radiographs

---

[3] As a matter of fact, 3 cm of water already absorbs half of the radiation emitted from a conventional X-ray tube used in clinical applications (operated at 120-140 kV).

[4] Each would require a separate thesis!

taken at different angles.

In chapter 2 the principles of operation of the Medipix chips are explained, and the main differences between the multiple versions of the chip, together with a summary of the properties that characterize their performance.

Chapter 3 describes the technique adopted to calibrate silicon based Medipix readout devices, necessary in order to define the energy scale of the detected X-ray spectra and to ensure a uniform response of the pixel matrix.

The precise determination of the detector energy response function is addressed in chapters 4 and 5. This task involves the measurement of the charge transport properties of the silicon sensor (chapter 4) and their use for the definition of a numerical model of the response function, whose parameters are tuned by comparing the calculations with data from synchrotron radiation measurements (chapter 5).

Chapter 6 combines all the previous results in the development of the spectral CT reconstruction techniques employed to extract material information from the spectroscopic Medipix data to produce color (i.e. material resolved) 3D X-ray images, free of beam hardening artifacts.

Finally, chapter 7 shows possibilities for a valorisation of this work, namely how the results obtained could lead to applications and how society could possibly benefit from them.

Chapter 1

Introduction to X-ray computed tomography

X-ray Computed Tomography (CT) is a three dimensional imaging technique for non invasive inspection of the interior of objects. Applications of X-ray CT cover several fields, from medicine to industry.

In this chapter the basic aspects of X-ray CT are presented, with focus on image reconstruction methods.

1.1 Computed tomography

Information on the three dimensional inner structure of an imaged sample can be extracted from a collection of two dimensional transmission images taken from different directions, using a dedicated reconstruction algorithm.

The word tomography stems from the ancient Greek *tomos*, “section”, and *graphein*, “write”, and refers to the fact that the 3D image of the object is usually built by reconstructing the data slice-by-slice and by stacking the sections on top of each other.

The set of two-dimensional images (called the projections) can be built by using penetrating radiation or waves that can be transmitted or emitted by the sample, e.g. electromagnetic radiation or acoustic waves. Each technique is suited for gaining contrast in images of specific structures and materials within the object. This means that the type of radiation or wave that must be used depends on the sample and the application.

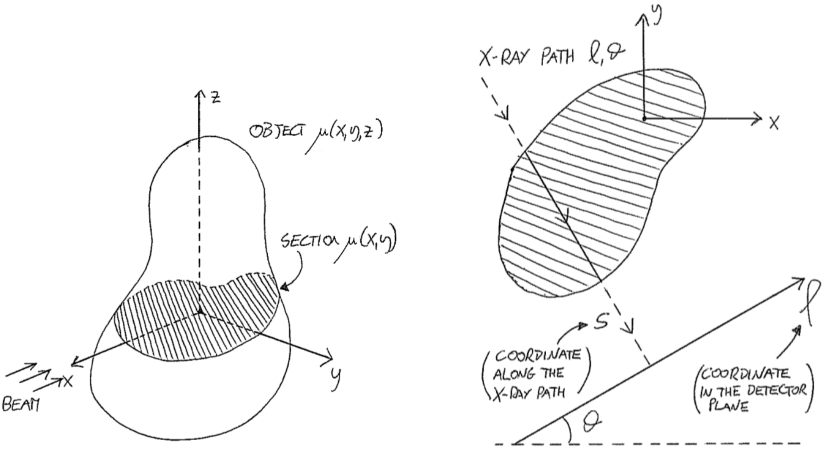

(a) (b)

Figure 1.1: **Principle of X-ray computed tomography.**

Alongside the most famous X-ray based tomography, widely employed in medicine as well as in industry and research, the list of other techniques and applications is long and varied [28]. One example is seismic tomography, that relies on the measurement of pressure waves in geological structures to reconstruct the composition of the Earth crust [48].

Despite such diversity, all the different types of computed tomography are linked by the same fundamental problem: how to pass from the set of two dimensional images to a full three dimensional reconstruction?

1.2 Reconstruction of X-ray transmission data

In this thesis, the focus will be on X-ray transmission tomography. The simplest definition of the problem considers a wide parallel beam of monochromatic radiation of intensity I_0 passing through an object. This can be represented as a scalar field $\mu(x, y, z)$ that gives the value of the photon absorption coefficient μ at position (x, y, z) in space. Figure 1.1a shows a sketch of this situation. The direction of the X-ray beam is chosen to be perpendicular to the z axis, so that the problem is reduced to the treatment of single two dimensional sections $\mu(x, y)$ of the object.

The set of projection data is acquired by imaging the object from different angles θ, defined as the angle between the x axis and the detector plane, as shown in figure 1.1b. Each image is represented by the values of the detected intensity I as a function of the one-dimensional detector coordinate l. An X-ray path is identified by the couple (l, θ) indicating the detector position l reached by the ray and the angle θ at which the image is taken. The intensity I for a given ray path (l, θ) depends on the attenuation of the source beam after traveling through the sample along the coordinate s.

For a thickness t of a homogeneous medium, photon attenuation is described by the exponential (Beer's) law

$$I = I_0 e^{-\mu t}. \tag{1.1}$$

The total absorption coefficient associated to a path (l, θ) is a summation (integral) of all the contributions found along the s coordinate. The attenuation law for a non-homogeneous object thus takes the form

$$I_{l,\theta} = I_0 e^{-\int_{l\theta} \mu(s)ds}, \tag{1.2}$$

where $\mu(s)$ describes the absorption coefficient as a function of the position along the path.

The line integral in formula 1.2 can be isolated by taking the logarithm:

$$R(l, \theta) \overset{def}{=} -\log\left(\frac{I_{l,\theta}}{I_0}\right) = \int_{l,\theta} \mu(s)ds. \tag{1.3}$$

This formula shows that the logarithm of the flat-field corrected projections[1], being equal to an additive quantity, is an additive quantity itself. This property is crucial for the applicability of many CT reconstruction algorithms, that operate on the logarithm of the data rather than on the data themselves.

The function $R(l, \theta) = -\log(I_{l,\theta}/I_0)$ is called the Radon transform, or sinogram, of the section $\mu(x, y)$, after the name of Johann Radon who, in 1917, first proved that equation 1.3 is a one-to-one relation. This means that $\mu(x, y)$ is uniquely determined by giving all the values of $R(l, \theta)$ for all possible paths (l, θ), and the problem of image reconstruction is a problem of inversion of equation 1.3. The solution can be approached in different ways, the most important of which will be introduced throughout the rest of the chapter.

---

[1] The flat field corrected projections are the projections $I_{l,\theta}$ normalized to the open beam image I_0.

1.3 Analytical solutions

The problem of tomographic reconstruction as stated in equation 1.3 has an analytical solution. Among the different approaches (e.g. [17, 18]), Filtered Backprojection (FBP) is the most successfull [58].

In this section, a brief review on backprojection theory and how the Filtered Backprojection formula is derived, are given.

1.3.1 Elements of backprojection theory

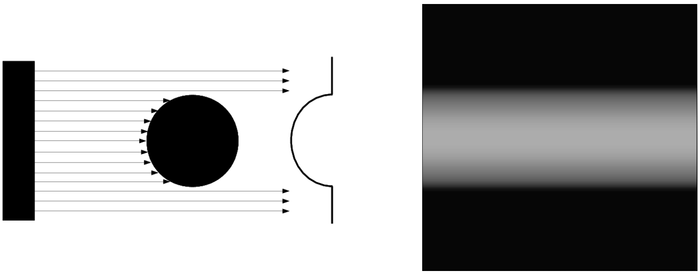

(a) **Image formation. The image on the right already corresponds to the $-\log{(I_{l,\theta}/I_0)}$ term in formula 1.3.**

(b) **Backprojected image, obtained by parallel transporting the data in the bi-dimensional plane.**

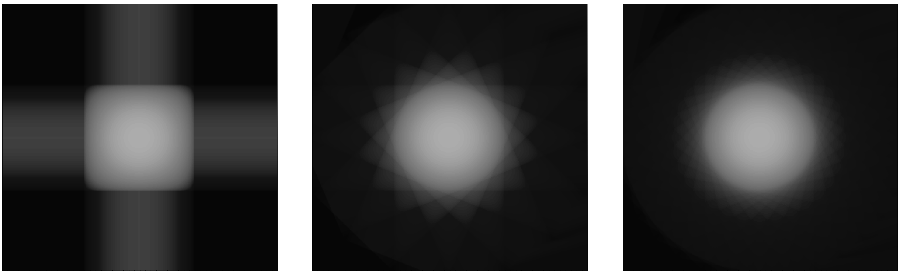

(c) **Superimposition of 2 backprojections.**

(d) **Superimposition of 8 backprojections.**

(e) **Superimposition of 16 backprojections.**

Figure 1.2: **Principle of backprojection for a two dimensional homogeneous cylinder section imaged by a wide parallel beam.**

The idea behind backprojection is sketched in figure 1.2. The reconstruction of a section slice relies on the principle of linear superimposition of the backprojected data. The condition of linearity holds as long as the Radon transform is properly defined, which ensures that the logarithm of the data is an additive quantity. In section 1.8, it will be explained that this assumption is never true for applications in which polychromatic X-ray sources are employed, which in fact constitute the majority of the cases. Backprojection algorithms, as well as any other algorithm relying on the additivity of the data, can still be applied but only provide approximate solutions.

From figures 1.2c, 1.2d and 1.2e, one can see that the more projections are used, the more the reconstruction resembles the true image. However, a number of artifacts appear. In particular a star shaped pattern in figure 1.2d, due to the finite number of projections used, and cupping artifacts, namely the appearance of gradients in structures that should be homogeneous, as in the reconstructions of the cylinder section in figures 1.2d and 1.2e). These effect can be removed (in theory) or reduced (in practice) by pre-filtering each projection using special functions. Hence the name filtered backprojection.

The Fourier slice theorem

The starting point of the filtered backprojection reconstruction method is the Fourier slice theorem, stating that, for a given angle θ, if $M(p)$ is the Fourier transform of the field $\mu(x, y)$ along a line parallel to the detector direction and passing from the rotation axis, and if $\mathcal{R}(p)$ is the Fourier transform of the sinogram $R(l, \theta)$ with respect to the l coordinate, then

$$M(p) = \mathcal{R}(p). \tag{1.4}$$

The possibility to give the field $\mu(x, y)$ a Fourier representation is ensured by the fact that a real object is always limited in space, and can thus be expanded as

$$\mu(x, y) = \sum_{n=-\infty}^{+\infty} \sum_{m=-\infty}^{+\infty} M(m, n) e^{i(mx+ny)}, \tag{1.5}$$

with

$$M(m, n) = \frac{1}{L^2} \int_{-L/2}^{+L/2} \int_{-L/2}^{+L/2} e^{-i(mx+ny)} \mu(x, y) dx dy, \tag{1.6}$$

where L is the size of the square box containing the object.

Equality 1.4 says that, in the Fourier space, each projection is equal to the corresponding parallel slice of the object. If projections are taken at different angles of view, the full two dimensional Fourier representation $M(p, \theta)$ can be calculated analytically, and the original object $\mu(x, y)$ can be reconstructed by reverse-transforming $M(p, \theta)$.

It can be proven that the Fourier slice theorem provides the actual analytical solution $M(p, \theta)$ when the number of projection angles is infinite [35]. So, at least in principle, all the information needed to reconstruct the object is condensed in formula 1.4.

However, in practice the number of Fourier components that can be measured is always finite. Equation 1.5 is thus changed into a Finite Fourier Transform (FFT) expression

$$\mu(x, y) = \sum_{n=-N/2}^{+N/2} \sum_{m=-N/2}^{+N/2} M(m, n) e^{i(mx+ny)}, \tag{1.7}$$

where N is the number of measured spatial frequencies.

The number of measured projections too is always finite. However, if a sufficient number of projections at different angles are taken, the system is diagonalizable (see also section 1.4).

Filtered backprojection

From the computational point of view, the Fourier slice theorem gives $M(m, n)$ through an interpolation process. This situation is illustrated in figure 1.3: for each projection, the corresponding slice is computed according to 1.4, but the collection of all slices builds up $M(m, n)$ only on a corresponding number of radial lines in the Fourier space, while all other values are determined by averaging with the neighboring points.

The Filtered Backprojection (FBP) formula provides a computational implementation that not only solves the interpolation problem, but that is also faster and more efficient, and at the same time yields a cupping artifact free solution.

FBP derives naturally from the Fourier slice theorem itself. Citing from [35]

> *The derivation of this algorithm is perhaps one of the most illustrative examples of how we can obtain a radically different computer implementation by simply rewriting the fundamental expressions for the underlying theory.*

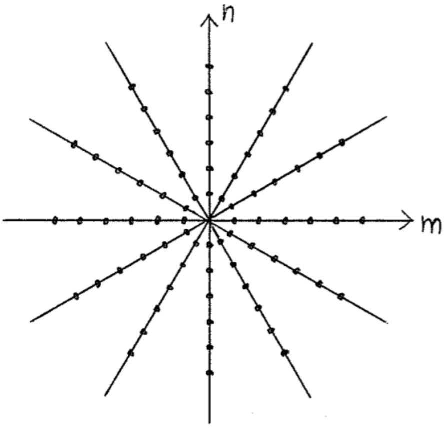

Figure 1.3: **Frequency domain representation of the application of the Fourier slice theorem: the reconstruction is carried out on a set of points along radial directions. All other values result from interpolation.**

Indeed, by writing explicitly the Fourier transforms in equation 1.4, and by rearranging the terms, one obtains

$$\mu(x, y) = \int_0^\pi Q_\theta(x \cos\theta + y \sin\theta) d\theta, \tag{1.8}$$

with

$$Q_\theta(x \cos\theta + y \sin\theta) = \int_{-\infty}^{+\infty} e^{2\pi i l(x \cos\theta + y \sin\theta)} R(l, \theta)|l|dl. \tag{1.9}$$

Equation 1.8 shows that $\mu(x, y)$ is given by the superimposition (backprojection) of functions $Q_\theta(x \cos\theta + y \sin\theta)$, and these functions are computed by weighting the projections $R(l, \theta)$ with the filter function $|l|$, as described by equation 1.9.

The advantage of formula 1.9 is that the filter is completely factorized, and can therefore be optimized separately. This feature is helpful when considering a real-life version of the problem. In fact, the computation of $Q_\theta(x \cos\theta + y \sin\theta)$ according to 1.9 is still ideal, since it requires an integration over all spatial frequencies l. In real life, spatial frequencies are truncated at some maximum value F that, according to the Nyquist-Shannon theorem, is related to the size

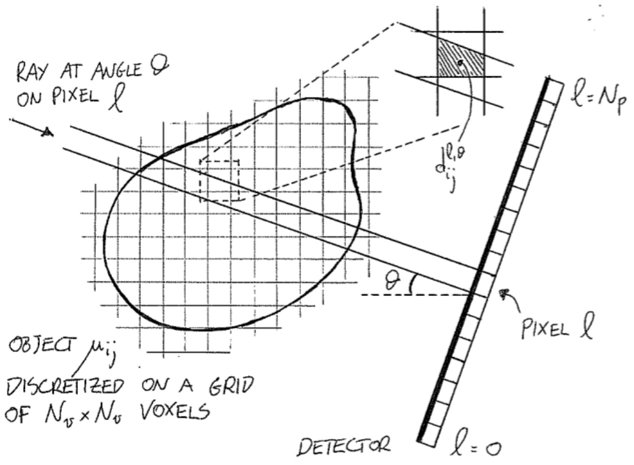

Figure 1.4: **Discretized model of computed tomography.**

δ of the intervals at which the image is sampled (i.e. the pixel pitch) through

$$\delta = \frac{1}{2F} \tag{1.10}$$

Such an approximation gives rise to noise in the reconstruction, that can be minimized by modifying the ideal filter $|l|$ as given in equation 1.9 with appropriate expressions optimized according to the specific situation [35].

1.4 Algebraic formulation

Algebraic algorithms provide a completely different approach to the solution of the tomographic reconstruction problem, where formula 1.3 is rewritten as a set of linear equations [35]. Again, this condition stems from the assumption that the Radon transform is properly defined, which makes it possible to handle the logarithm of the data as an additive quantity.

The starting point is the discretized version of equation 1.3, as shown in figure 1.4. The continuous object distribution $\mu(x, y)$ is substituted with a discrete field μ_{ij}, where the indices (i, j) assume values within a grid of $N_v \times N_v$ square voxels of size $d \times d$, and the coordinate l takes discrete values from 1 up to the number of detector pixels N_p.

In this framework, a single projection at angle θ is given by

$$R(l) = \sum_{i,j} d_{ij}^{l} \mu_{ij} \qquad \left\{ \begin{array}{l} i,j = 1,...,N_v \\ l = 1,...,N_p \end{array} \right. , \tag{1.11}$$

where the coefficients d_{ij}^{l} represent the fraction of the voxel volume that ray l covers at position (i,j).

Equation 1.11 is a set of N_p independent equations in the N_v unknowns μ_{ij}. Since all rays are parallel, the system is inconsistent. The dependence between equations is introduced by merging multiple systems obtained at different values of θ. If N_θ is the number of projections, then one has

$$R(l,\theta) = \sum_{i,j} d_{ij}^{l\theta} \mu_{ij} \qquad \left\{ \begin{array}{l} i,j = 1,...,N_v \\ l = 1,...,N_p \\ \theta = \theta_1,...,\theta_{N_\theta} \end{array} \right. \tag{1.12}$$

The problem of tomographic reconstruction is now turned into a problem of inversion of a system of equations, whose solution exists as long as the necessary condition $N_p N_\theta \geq N_v^2$ holds. This condition sets the limit on the resolution that can be achieved in the final reconstruction. If L is the linear size of the image, then in the best case the voxel size will not be smaller than $L/\sqrt{N_p N_\theta}$.

1.5 Iterative methods

In iterative methods, the reconstruction is performed by means of a recursive algorithm in which the estimation of the final image is improved at each step until a specific convergence criterion is reached.

Most of these algorithms rely on the expectation maximization technique, where each iteration includes a phase in which the calculated data is compared to the measurements in order to both update the estimation and assess the status of the convergence [5].

1.5.1 Expectation maximization

The term "expectation maximization" refers to a general category of algorithms developed within the theory of estimation of maximum likelihood functions, used to solve problems of parameter estimation in case of hidden or missing data [19]. Computed tomography can be viewed as such a problem: find the best estimate of $\mu(x,y)$ from the incomplete data set of its projections $R(l,\theta)$.

General formulation

An incomplete set of data is a collection of observations $\vec{x}$ that only partially reproduces the true sample $\vec{y}$. Given a set of parameters $\vec{\eta}$, the measured probability density $P^{meas}(\vec{x}|\vec{\eta})$ is connected to the true probability density $P(\vec{y}|\vec{\eta})$ via an integration of the form

$$P^{meas}(\vec{x}|\vec{\eta}) = \int_{Y(\vec{x})} P(\vec{y}|\vec{\eta}) d\vec{y}, \tag{1.13}$$

where $Y(\vec{x})$ is the space of the possible values of $\vec{y}$. The problem is then a maximum likelihood one: find the value of $\vec{\eta}$ that maximizes $P^{meas}(\vec{x}|\vec{\eta})$ given the observation $\vec{x}$.

The expectation maximization algorithm comes into action when the analytical approach to the solution of the problem is not feasible, for example when the number of parameters is too high, which is the case in computed tomography. Indeed, one may notice that equation 1.3 is a special case of expression 1.13.

In its most general formulation, the Expectation Maximization algorithm runs as follows:

1. build an initial estimate $\vec{\eta}_0$ of the parameters[2]
2. define the probability density function $P_1(\vec{y}|\vec{\eta}) = P(\vec{y}|\vec{\eta}_0)$
3. expectation step: use $P_1(\vec{y}|\vec{\eta})$ to calculate the expected $P_1^{meas}(\vec{x}|\vec{\eta})$ according to 1.13
4. maximization step: calculate the new set of parameters $\vec{\eta}_1$ that maximizes $P_1^{meas}(\vec{x}|\vec{\eta})$
5. iteration: repeat from 2: use $\vec{\eta}_1$ to build $P_2(\vec{y}|\vec{\eta}) = P(\vec{y}|\vec{\eta}_1)$
6. iterate until a convergence criterion is met

Application to computed tomography

In the work presented in this thesis, tomographic reconstruction on data taken with Medipix based detectors is often conducted using an Expectation Maximization type of algorithm derived from the Shepp and Vardi formulation for

---

[2] Typically a uniform distribution, even though Bayesian estimation for the prior knowledge of $\vec{\eta}_0$ can be applied [59].

the case of emission tomography [59], where the adaption to transmission tomography is done by applying the original algorithm to the logarithm of the data (equation 1.3.).

The algorithm is the following:

1. build an initial estimate μ^0, e.g. by backprojecting the data via superimposition:

$$\mu_{ij}^0 = \frac{\sum_{l=1}^{N_p} \sum_{\theta=\theta_1}^{\theta_{N_\theta}} d_{ij}^{l,\theta} R(l,\theta)}{\sum_{l=1}^{N_p} \sum_{\theta=\theta_1}^{\theta_{N_\theta}} d_{ij}^{l,\theta}} \tag{1.14}$$

2. expectation step: use μ^0 to calculate a set of projections $R^1(l,\theta)$ by summing the CT numbers[3] along each ray path:

$$R^1(l,\theta) = \sum_{ij} d_{ij}^{l,\theta} \mu_{ij}^0 \tag{1.15}$$

3. maximization step: define a set of correction coefficients $c_{l,\theta}^1$ by dividing the obtained projections with the measured ones:

$$c_{l,\theta}^1 = \frac{R^1(l,\theta)}{R(l,\theta)} \tag{1.16}$$

4. backproject the corrections via superimposition to define a new field of corrections c_{ij}^1 in the voxel space:

$$c_{ij}^1 = \frac{\sum_{l=1}^{N_p} \sum_{\theta=\theta_1}^{\theta_{N_\theta}} d_{ij}^{l,\theta} c_{l,\theta}^1}{\sum_{l=1}^{N_p} \sum_{\theta=\theta_1}^{\theta_{N_\theta}} d_{ij}^{l,\theta}} \tag{1.17}$$

5. use the backprojected corrections to multiply μ_0 and update it to a new estimation μ_1

$$\mu_{ij}^1 = c_{ij}^1 \mu_{ij}^0 \tag{1.18}$$

---

[3] The raw values of a reconstructed CT section are referred to as CT numbers. Even if a specific reconstruction algorithm is formulated to provide an explicit expression for the solution $\mu(x,y)$, the units of the CT numbers are generally undefined. Although a grayscale visualization of the images in the CT numbers space already provides an immediate representation of the inner structure of the sample, quantitative information can only be extracted once the CT numbers have been calibrated. Examples of calibrations are the conversion into Hounsfield units typical of medical applications or, similarly, the signal-to-thickness calibration described in appendix A.

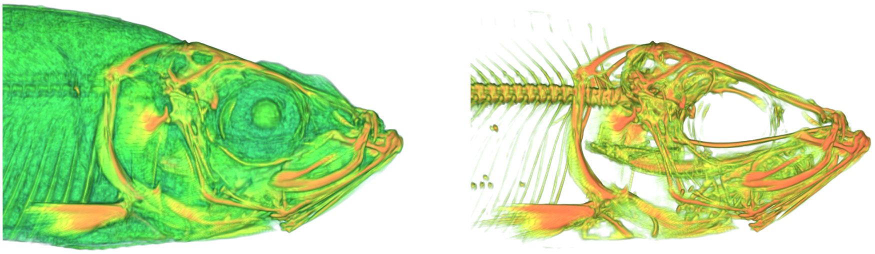

(a) **Full range.**

(b) **After suppressing low absorbing components.**

Figure 1.5: **X-ray computed tomography reconstruction of a frozen fish from data taken with a Timepix quad detector at Nikhef. The color scale is only for visualization purposes.**

6. iteration: repeat from 2: use μ_1 to calculate the projections $R_2(l,\theta)$
7. iterate until convergence criterion is met

In this version of the algorithm, the initial estimation of the μ^0 field is done by a first backprojection of the data. In other variants, μ^0 can be initialized in different ways, for example as a uniform distribution. In general, independently from the initialization choice, iteration n can be expressed in a compact form as

$$\mu_{ij}^{n+1} = \mu_{ij}^{n} \frac{\sum_{l=1}^{N_p} \sum_{\theta=\theta_1}^{\theta_{N_\theta}} d_{ij}^{l,\theta} \frac{\sum_{ij} d_{ij}^{l,\theta} \mu_{ij}^{n}}{R(l,\theta)}}{\sum_{l=1}^{N_p} \sum_{\theta=\theta_1}^{\theta_{N_\theta}} d_{ij}^{l,\theta}} \tag{1.19}$$

1.5.2 Ordered subsets

From the computational point of view, iterative algorithms are much more expensive if compared, for instance, to backprojection algorithms. This is the reason why, although iterative algorithms usually give better results than backprojection techniques, these latter are still employed when reconstruction time is a main concern, as it is in medical applications.

To limit both the overall processing time and the convergence speed in iterative reconstruction algorithms, several acceleration techniques have been developed over the years. One of these is the Ordered Subsets Expectation Maximization (OSEM) algorithm, as introduced by Hudson and Larkin [32] for the case of emission tomography, that can be applied to transmission tomography on the logarithm of the data. In an OSEM algorithm the dataset of projections at angles $\theta_1, \cdots, \theta_N$ is grouped into M subsets $S_1, \cdots, S_M$ where each subset S_i contains the projections corresponding to the sub-group of angles $\{\theta_{i1}, \cdots, \theta_{iM_i}\}$. The Expectation and Maximization steps are performed on the M subsets subsequently, with the advantage that the forward-projection and the back-projection operators are only applied on a smaller amount of data than the full dataset, at each step. This results in a reduced computation time, but also in a faster convergence. It can be proven that the greater the number of subsets, the faster the convergence [32].

Figure 1.5 shows the X-ray computed tomography of a frozen fish from data taken with a Timepix detector at Nikhef and reconstructed using the Ordered Subsets version of the Expectation Maximization algorithm described in the previous section.

1.6 Statistical approach

All the aforementioned reconstruction techniques are based on the assumption of monochromatic radiation source, which ensures that photon attenuation can be written as 1.2, hence the validity of equation 1.3. Extension of these algorithms to account not only for spectrum polychromaticity, but also for scattering and fluorescence, is difficult, if not impossible. However, these processes play a relevant role in many situations, and not accounting for them leads to a degradation of the image quality. Implementing all this information in the reconstruction phase is therefore a crucial aspect for the advancement of X-ray computed tomography. The work described in this thesis has been carried out with the aim of demonstrating how the addition of spectral information is beneficial for the quality of the reconstructions.

Algorithms based on models of the statistical nature of photon detection offer a framework where more complex features can be implemented in an intuitive way if compared to other methods. This difference will be clear in chapter 6 where it will be shown how the inclusion of spectral information in the reconstruction process requires a complex machinery for the case of the OSEM algorithm, while it is straightforward in a statistical algorithm.

In the statistical concept, a digital X-ray image of an object is considered as the result of a stochastic process where the value in each pixel is distributed according to a well defined probability density function. The overall image (or set of images) is then interpreted as the most likely result of the full X-ray imaging chain of processes, and the problem of tomographic reconstruction is to find the $\mu(x, y)$ field that is most likely to have generated the observed data. That is to say, the problem of tomographic reconstruction is equivalent to a likelihood maximization problem [21, 53][4].

1.6.1 Maximum likelihood formulation

The statistical nature of the photon transmission and detection processes can be modeled starting from the discretized version of the attenuation law 1.2 (see also figure 1.4), that now takes the form

$$I_{l,\theta} = I_0 e^{-t \sum_{i,j}^{l\theta} \mu_{ij}}. \tag{1.20}$$

where $\sum_{i,j}^{l\theta}$ means that the summation over the indices (i, j) has to be performed only along the ray path (l, θ).

$I_{l,\theta}$ is the beam intensity, namely the number of X-ray photons per unit time, that are seen by pixel l after the source intensity I_0 has been transmitted through the sample object at angle θ. This number can be considered as the most probable value of a stochastic process governed by Poisson statistics. In this view, the actual photon counts from ray (l, θ) are random variables $C_{l,\theta}$ distributed according to

$$P(C_{l\theta}|I_{l\theta}) = \frac{(I_{l\theta})^{C_{l\theta}} e^{I_{l\theta}}}{C_{l\theta}!}, \tag{1.21}$$

where $I_{l,\theta}$ is the expected value.

In this simplified model, where no sources of correlations between different paths are present[5], the total probability density function for the whole dataset is

$$P(\vec{C}|\vec{I}) = \prod_{l,\theta} \frac{(I_{l\theta})^{C_{l\theta}} e^{I_{l\theta}}}{C_{l\theta}!}, \tag{1.22}$$

with $\vec{C}$ and $\vec{I}$ being the vectors of all $C_{l,\theta}$'s and $I_{l,\theta}$'s respectively.

---

[4] It should be noted that a likelihood-based technique is, in essence, an iterative algorithm, because the minimization engine works in successive iteration steps. As a consequence, it will never compete with backprojection in terms of speed.

[5] Such as scattering or fluorescence, that cause photons to deviate from the ray path and being detected by a pixel $l' \neq l$

Following the maximum likelihood principle, the unknowns μ_{ij}, hidden in the formulation of the expectation values $I_{l,\theta}$ through equation 1.20, can be determined as the field that maximizes $P(\vec{C}|\vec{I})$ or, equivalently, that minimizes the negative log-likelihood function

$$\mathcal{L}(\vec{C}|\vec{I}) = -\log[P(\vec{C}|\vec{I})] = -\sum_{l,\theta} [C_{l\theta} \log(I_{l\theta}) + I_{l\theta}] \,. \tag{1.23}$$

Notice that the term in $C_{l\theta}!$ has been dropped, since it does not depend on the μ_{ij}'s and thus it does not contribute to the gradient of $\mathcal{L}(\vec{C}|\vec{I})$.

Due to the high number of free parameters, minimization of $\mathcal{L}(\vec{C}|\vec{I})$ is a challenging problem. Even more so if one considers that, in the most general case, a computed tomography dataset is incomplete in the sense discussed in section 1.5.1. Nonetheless, the statistical approach is of major interest because it provides a framework where the physics of the various steps involved in the process of image formation can be implemented in an direct way. One of these features is the polychromaticity of the source spectrum and the energy dependency of the variables that characterize the transmission and in the detection phases, which opens the way towards a formulation of a reconstruction technique suited for spectral tomography.

1.7 Artifacts

The algorithms introduced so far constitute the basis for most of the reconstruction techniques employed in computed tomography. Although all of them are widely used in many applications, CT reconstructions suffer from a series of artifacts that degrade the quality of the images [49].

While some artifacts depend on faults during data taking (such as motion of the object or defects of the detector), other are generated by the reconstruction algorithm. Figure 1.6 shows some examples for the case of medical X-ray computed tomography. Among the most common, one finds

- streak artifacts (image A), usually caused by faults in the sampling of the object, such as under-sampling or data corruption, or to the motion of the sample during the data taking (image B);
- ring artifacts (images D and E), caused by noisy detector elements;
- beam hardening artifacts (images C and F), arising from the fact that spectral information is not measured and/or not accounted for in the reconstruction phase.

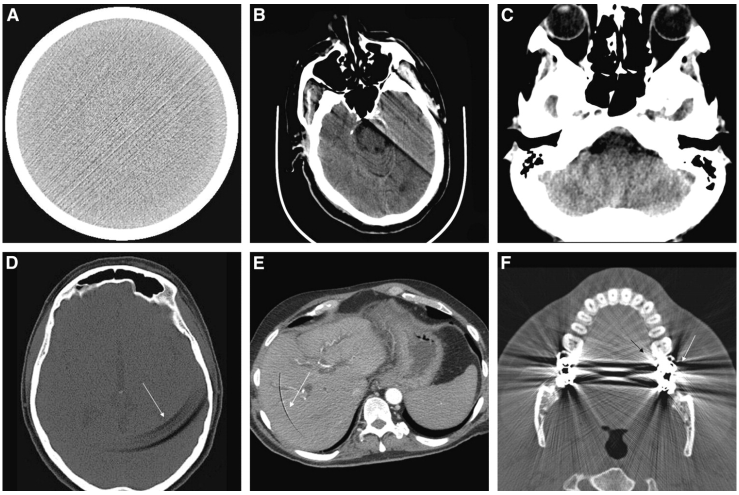

Figure 1.6: **Typical artifacts in medical computed tomography. Image credit [49].**

1.7.1 Beam hardening artifacts

The X-ray tube sources employed in the majority of imaging applications emit a polychromatic spectrum. Due to the energy dependence of the attenuation coefficient, attenuation through the sample material results in strong spectral distortions, as shown in figure 1.7. Since, in general, the attenuation coefficient is monotonically decreasing as a function of energy[6], the mean value of the transmitted spectrum is shifted towards higher energies, namely the spectrum becomes “harder”.

In imaging applications, beam hardening causes an unequal illumination of the sample, thus giving rise to artifacts in the X-ray images. The effect is particularly evident when the material composition of the object is very heterogeneous. Typical examples of beam hardening artifacts in medical computed tomography were shown in figure 1.6. In image C, a dark band appears in the center of the skull, caused by the strong beam hardening undergone by the source spectrum in the hard tissue of the bones, compared to the soft brain tissue. The effect is even more evident in image F, where streak artifacts are caused by the presence of metal dental implants in the patient’s jaw.

---

[6] Monotonicity is broken by characteristic absorption edges, as the ones in figure 1.7a.

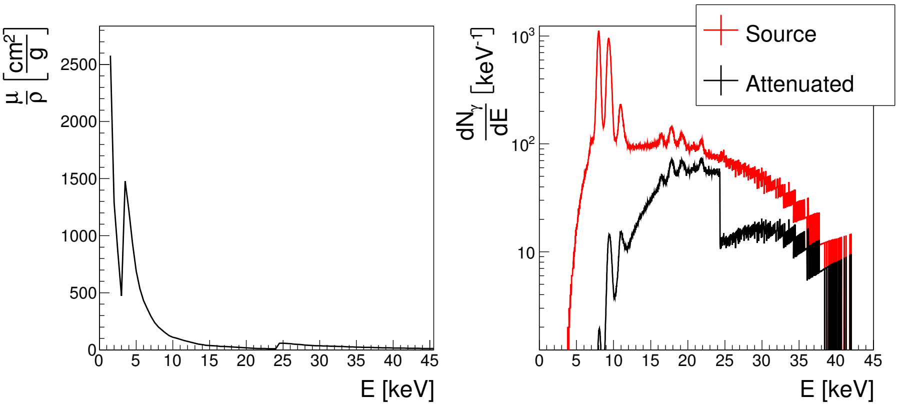

(a) **Mass attenuation coefficient for palladium.**

(b) **Attenuation of the source spectrum by a 0.001 inch thin palladium foil.**

Figure 1.7: **Beam hardening.**

1.8 Energy sensitivity

In the reconstruction techniques so far described, it was always assumed that photon attenuation follows formula 1.2. This assumption is crucial to ensure that the Radon transform of the projections is an additive quantity, and hence to derive the Filtered Backprojection formula 1.9 (analytical solution), the linear system of equations 1.12 (algebraic solution) and the expectation maximization algorithm 1.19 (iterative solution).

However, formula 1.2 only holds in the very special case of monochromatic radiation. To account for the energy dependence of photon attenuation, formula 1.2 has to be replaced by

$$S_{l,\theta}(E) = S_0(E)e^{-\int_{l\theta}\mu(s,E)ds}. \tag{1.24}$$

Here $S_0(E)$ represents a generic X-ray source spectrum and $S_{l,\theta}(E)$ is the corresponding transmitted spectrum. The energy dependence of the attenuation process is explicit in the energy dependence of the attenuation coefficient $\mu(s, E)$.

The detected intensity is given by the integral of the transmitted spectrum[7]

$$I_{l,\theta}^{th} = \int_{E_l^{th}}^{\infty} S_0(E) e^{-\int_{l\theta} \mu(s,E)ds} dE, \tag{1.25}$$

where the superscript th is the threshold index for the detector element at position l. The corresponding open beam intensity is

$$I_0^{th} = \int_{E^{th}}^{\infty} S_0(E) dE. \tag{1.26}$$

From formulas 1.25 and 1.26 it follows that equation 1.3 is no longer valid, namely the Radon transform is not properly defined:

$$R(l,\theta) \neq \int_{l,\theta} \mu(s) ds. \tag{1.27}$$

As a consequence, algorithms relying on the additivity of the data only provide an approximate solution, where beam hardening artifacts can strongly affect image quality.

Accounting for the polychromatic nature of the source spectrum is a non trivial problem. Many techniques developed for reducing beam hardening effects consist of pre- and/or post-processing methods [63, 45]. An example is the signal-to-thickness calibration described in appendix A, which will be employed to get some of the results presented in this thesis.

However, these techniques only aim at correcting the artifacts, while the most appropriate solution to prevent them is the implementation of spectral information in the reconstruction algorithms themselves, i.e. spectral CT, which is possible when using energy resolving imaging detectors, such as Medipix based devices.

---

[7] In the most general case one would write

$$I_{l,\theta}^{t} = \int_{E_l^{t}}^{\infty} S_0(E) w(E) e^{-\int_{l\theta} \mu(s,E)ds} dE,$$

where $w(E)$ is an energy weighting factor. For an energy integrating detector, it would be $w(E) = E$, while one has $w(E) = 1$, i.e. formula 1.25, in the case of a photon counting detector (see section 2.2.1). Different expressions for $w(E)$ can be chosen in order to enhance contrast in X-ray images [26].

Chapter 2

The Medipix chip

In conventional X-ray detection systems, the measurement of the energy of single photons is possible only at the expense of spatial resolution. Today, deep sub-micron technologies for integrated circuit design enable complex electronic readout schemes and processing of signals for individual small ($< 100\ \mu$m) pixels.

An example of these devices are the Medipix and Timepix chips, that can be used to readout semiconductor pixel sensors to realize energy sensitive detectors for X-ray imaging applications.

2.1 X-ray detectors

The principle of X-ray detection is the same as for any other type of radiation: choose a sensor material in which particles deposit energy, and convert this energy into a measurable signal.

In the energy range of X-rays[1], the most probable process of energy loss in matter is the photoelectric effect, where the energy of a single photon is converted at once. This implies that a measurement of the signal produced by a single quantum is also a direct measurement of its original energy.

The first devices ever used to detect X-rays were photographic films, employed since the discovery of X-rays by Röntgen in 1895 [62]. As in all the fields of imaging, the invention of the Charge Coupled Device (CCD) [12] can be regarded as the start of the transition from the analog to the digital era. Nowa-

---

[1] Roughly, from 100 eV to 100 keV

days, the most frequently employed X-ray detector is the flat-panel detector, based on Active Matrix Liquid Crystal Display (AMLCD) technology [8, 50].

All these detectors are energy integrating systems, where the signal is a direct measure of the total energy released by all the X-ray quanta that are converted during the exposure. The transition from energy integrating to photon counting has been possible only with the emergence of active pixel devices, i.e. chips where each pixel incorporates an active electronic circuitry, able to perform all the functions that are required to process raw signals, including energy discrimination.

2.2 Medipix based detectors

Medipix chips are integrated circuits for spectroscopic readout of pixellated sensors. These devices are designed by an international collaboration based at the European Center for Nuclear Research (CERN). Since the establishment of the collaboration in the late 90's, different versions of the chip have been developed.

The prototype chip was the Medipix1 [13], a 64×64 matrix of 170×170 μm^2 size pixels, designed in 1 μm SACMOS technology. Detectors were built by connecting the Medipix1 to semiconductor sensors and tested in different applications, such as X-ray imaging [1], particle detection [7] and synchrotron light detection [71]. Medipix1 proved the benefits of a high dynamic range, provided by the 15-bit digital counter implemented in each pixel, in X-ray imaging applications, where materials with very different absorption capability could be imaged in a single exposure.

The success of the Medipix1 chip triggered the design of the Medipix2 [43], that would address the limitations encountered in the prototype run [72], among which the large pixel size. By employing 0.25 μm CMOS technology, the pixel area was reduced to 55×55 μm^2.

In the course of the years, spectroscopic X-ray detectors based on the Medipix2 readout have been employed in a wealth of applications[2]. Further chip designs followed afterwards, among which Timepix, Medipix3 and Timepix3. Before going into details on the chip design and functionality, few general features of Medipix based detectors are outlined.

---

[2] Some of the publications on results obtained with Medipix are listed in the website of the collaboration [16].

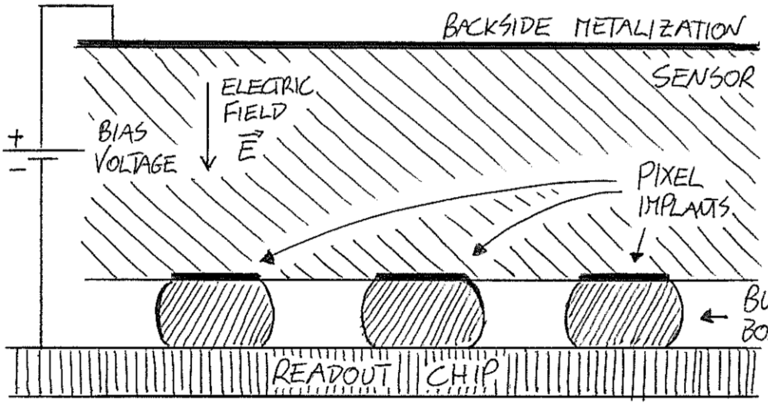

Figure 2.1: **Principle of operation of a hybrid semiconductor pixel detector.**

2.2.1 General features

Medipix chips are designed for electronic-noise free direct detection in single-photon counting mode with spectral capability at small pixel sizes. Each of these features represents a potential improvement with respect to conventional detector technologies.

Hybridization and direct detection

Medipix and Timepix based detectors are hybrid devices. Hybrid means that the detector itself (the sensor) and the readout (the electronic chip) are manufactured separately before being connected to each other. As a consequence, the two can be optimized individually, and moreover the readout chip alone remains available for a wealth of other possible applications.

As a matter of fact, detectors based on Medipix and Timepix readout chips have found applications in several fields outside X-ray imaging as well, where sensor materials other than semiconductors have been applied. A few examples are the family of Gridpix gaseous time projection chambers [14] for 3D tracking of high energy particles, or the micro channel plate based detectors for applications in mass spectrometry [34].

Integration of a semiconductor sensor is achieved with bump-bonding of each pixel from the sensor to the readout. The principle of operation of such a device is shown in figure 2.1.

An advantage of using semiconductors as X-ray detectors is that the sensor is used as a direct detector. This means that the photon is converted in the sensor itself, without the need of a preliminary conversion into visible light, as in indirect detectors, where this is a major cause of degradation of the spatial resolution.

Photon counting

Electronic noise free operation in Medipix and Timepix devices is ensured by the presence of a discrimination logic in each pixel (see section 2.3.1). Thanks to it, only signals that are higher than a certain threshold are selected, while lower ones are disregarded. If the threshold is sufficiently high, the noise is completely suppressed. As a consequence, potentially less dose is required to achieve the same signal-to-noise ratio with respect to a conventional flat panel detector. This feature represents a considerable potential improvement for medical applications.

The discrimination logic also allows for operation in photon counting mode (see section 2.3.1). In a photon counting device each detected quantum is equally weighted. This is not true for energy integrating detectors, where each photon is weighted proportionally to its energy, with the effect that low energy quanta, that contribute more to the image contrast, are weighted less than high energy quanta. It has been shown that contrast can be maximized by determining the optimal energy dependence of the weights [26]. This is possible thanks to spectroscopic detectors, where the detection of each quantum is also accompanied by a measurement of its energy.

2.3 Medipix2

Most of the results presented in this thesis have been achieved using a Medipix2 [43] chip for the readout of silicon based pixel sensors.

Medipix2 is designed in 0.25 μm commercial IBM CMOS technology. The 55 μm square pixel area hosts about 500 transistors. The full ASIC is a matrix of 256×256 pixels, with a total active area of 1.982 cm^2, which represents 87.35% of the area of the full chip. The remaining 12.65% is formed by the peripheral circuitry (see figure 2.2).

The small pixel size makes the Medipix2 chip competitive in terms of spatial resolution with a common film screen radiographic system, where the typical pixel pitch is in the order of fractions of a millimeter. The minimization of

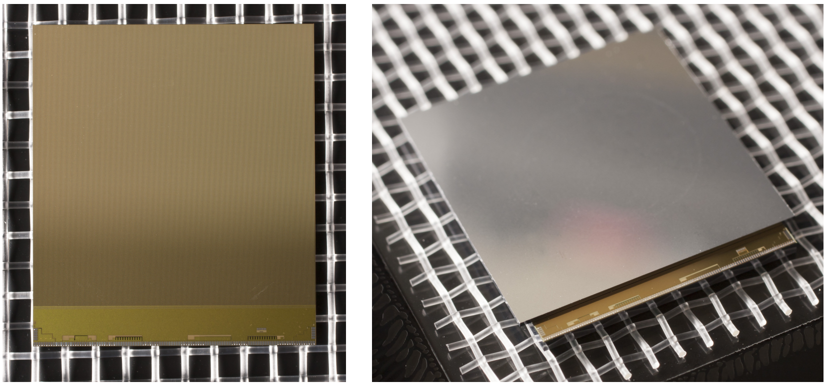

Figure 2.2: **On the left, a bare Medipix2 chip, where the periphery extending at the bottom of the pixel matrix is visible. On the right, a typical assembly with a conventional 300 μm silicon sensor. Notice that the surface of the sensor exceeds the borders of the readout chip. Image credit Jan Koopstra, Nikhef.**

the dead area at the edges of the sensor remains the only obstacle towards a fully tilable system in view of a large area Medipix based detector (see, for example, [44]).

2.3.1 Chip layout

The chip is organized in two main parts: the matrix of pixel cells and the periphery.

Pixel cell

Figure 2.3 shows the scheme of the Medipix2 pixel electronics, a detailed description of which is given in appendix B. The main features of the pixel cell are the presence of a double discrimination logic and of a 14-bit digital counter. In Medipix2 each pixel is provided with two simultaneous discriminators, where the incoming signal is compared to two different thresholds. In order to correct for inter-pixel mismatches in the threshold position, a 3-bit current adjustment circuitry is implemented for each discriminator.

The chip can be operated in two modes: single threshold or double threshold (energy window). In single threshold mode, the digital counter is incremented

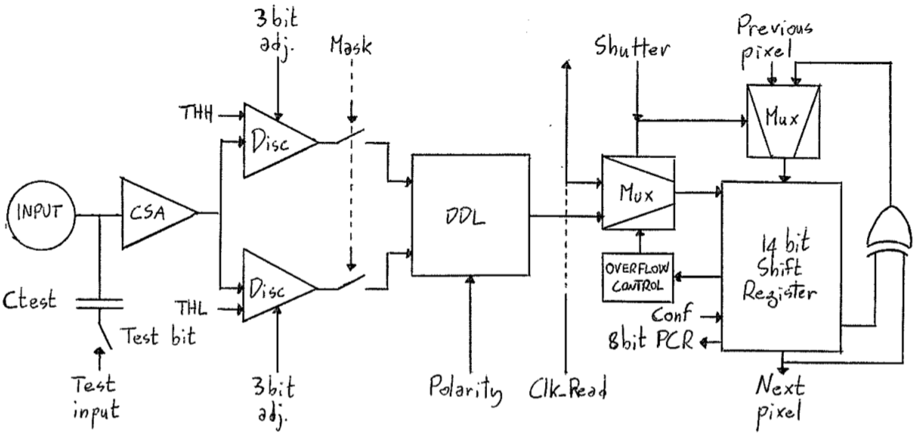

Figure 2.3: **Schematics of the Medipix2 pixel logic. For details, see appendix B.**

by one unit each time a signal exceeds the threshold during the period in which the shutter is open. The same happens in energy window mode, but only if at the same time the signal does not cross the second (higher) threshold. Thanks to this strategy, Medipix2 achieves single photon counting capability and full suppression of the electronic noise, which is filtered out by the discrimination logic.

Periphery

This part of the chip contains the supplies of the analog biases and the generators of the digital control signals, as well as the input/output (I/O) circuitry and the pads for the wire bonds. The analog part of the periphery comprises the 13 8-bit Digital-To-Analog-Converter (DAC) that the user can set in order to operate the chip in the preferred mode, among which the two threshold DACs.

The periphery is situated on one side of the pixel matrix with a width of about 2 mm. Since the other sides are free, the chip is buttable on three sides.

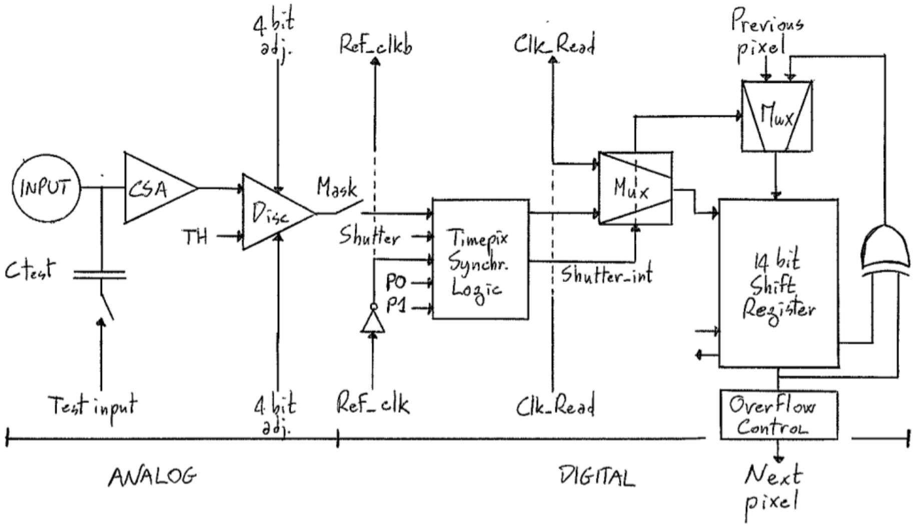

Figure 2.4: **Schematics of the Timepix pixel logic.**

2.4 Timepix

The Timepix chip [42] was originally conceived after successes with application of gas as a sensor to Medipix2 chips. The goal of the Timepix chip was then to provide time of arrival information to allow for 3D tracking of ionizing particles in a small volume time projection chamber [69].

Even though this thesis focuses on the application of detectors of the Medipix type, Timepix has been used in auxiliary experiments.

Being derived from Medipix2, the Timepix chip shares many of its features. Again, 55 μm square pixels are organized in a 256×256 matrix plus a periphery at one of the sides, ensuring three side buttability. The main differences arise in the pixel logic.

2.4.1 Pixel logic

The diagram of the Timepix pixel logic is shown in figure 2.4. Differently from Medipix2, the analog circuitry hosts only one discriminator with a 4-bit local threshold adjustment scheme.

Timepix can be operated in three possible modes (see figure 2.5): Medipix

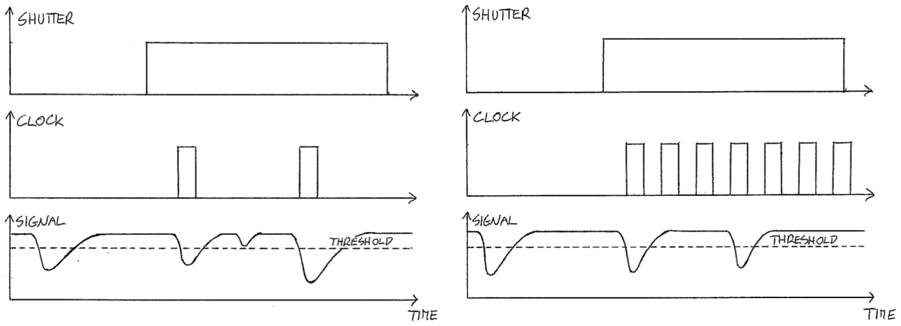

(a) **Medipix mode** (b) **ToA mode**

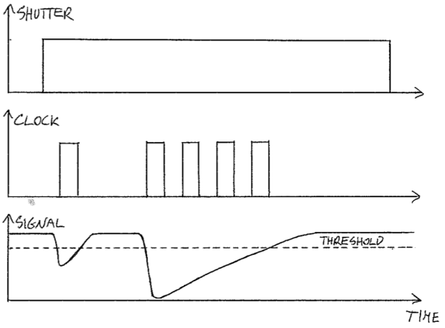

(c) **ToT mode**

Figure 2.5: **Timepix operation modes.**

(single threshold photon counting, same as Medipix2, shown in figure 2.5a), Time-of-Arrival (ToA) and Time-over-Threshold (ToT). The operation mode can be set via the two configuration bits P0 and P1 in the Timepix Synchronization Logic (TSL). ToA and ToT both make use of an external reference clock (Ref_Clk) distributed globally when the shutter signal is enabled.

In ToA mode, the 14-bit Shift Register starts counting upon the arrival of the first signal above threshold, using Ref_Clk as a clock, and stops at the end of the shutter. This principle is illustrated in figure 2.5b.

In ToT mode (figure 2.5c), the counter is activated the moment the signal goes above threshold, and it stops when the signal falls back below threshold. If multiple successive signals exceed threshold during the same shutter time, their counts are summed. Since the time over threshold is proportional to the input charge, ToT provides a direct estimation of the integrated energy detected during the shutter time.

2.5 Medipix3

Medipix3 [3, 51] was designed to overcome the two main limiations of Medipix2:

1. sensitivity to different energies can be achieved only by repeating the measurement while varying the threshold(s);
2. when connected to a semiconductor X-ray sensor, the detected spectrum is strongly distorted by charge sharing effects.

Charge sharing is a typical phenomenon occurring in finely segmented detectors, where the cloud of charge carriers generated in a given detector element is shared with the neighbouring elements, as a consequence of the fact that the thickness of the sensor is significantly larger than the size of the electrodes (see section 3.1.3).

This effect is particularly strong in Medipix based detectors, due to the small pixel size compared to the typical size of the lateral diffusion of the charge cloud. For a 300 μm silicon sensor operated at 100 V bias voltage, the typical size of the charge cloud after diffusion through the full sensor depth is in the order of 20 μm FWHM. More details on the diffusion process and its influence on chare sharing effects will be given in section 4.1.

The impact of charge sharing for Medipix and Timepix detectors stands out when considering that spectral sensitivity in both pixel logics derives from the measurement of the amount of charge that is collected by the pixel. For these detectors, charge sharing is the major source of spectral distortion.

The availability of the 0.13 μm CMOS circuit integration technology allowed the implementation, in Medipix3, of more functions within the same area, with respect to Medipix2 and Timepix, in particular two independent 12-bit digital counters. Moreover, thanks to the presence of an inter-pixel comunication logic, the chip can be operated in two main modes: spectroscopic and charge summing.

2.5.1 Spectroscopic operation mode

When the Medipix3 chip is standardly bump-bonded to a semiconductor sensor, it operates in the so called Fine Pitch mode and in fact it works like a Medipix2 chip with 55 μm pixel size. Alternatively, by connecting only one of four pixels in a 2×2 cluster, the detector operates in Spectroscopic Mode.

Effectively, the detector is now a matrix of 110 μm pitch square super-pixels. Since each pixel incorporates two discriminators and two independent counters, the super-pixel is an individual detector element with eight simultaneous thresholds. This implies that multiple images in different energy windows can be acquired within a single exposure. Although this is achieved at the expense of spatial resolution, 110 μm pixel pitch is still a very competitive size for medical imaging in most applications.

2.5.2 Charge summing operation mode

Charge Summing mode is made possible by the inter-pixel comunication logic, and can be enabled in both Fine Pitch and Spectroscopic mode. In Charge Summing configuration, the charge in a 2×2 cluster of pixels (or super-pixels in the case of spectroscopic operation) is summed and assigned to the pixel (super-pixel) where most of the charge was deposited. This is done asynchronously on an event-by-event basis.

Preliminary measurements have already shown the benefits of the charge summing logic on the spectral performance of Medipix3 based X-ray detectors[27], demonstrating that charge sharing effects are practically eliminated.

2.6 Performance of Medipix and Timepix

The performance of Medipix and Timepix chips is limited by the characteristic properties of the pixel electronics components and by space constraints in the implementation of functions in the small pixel area.

2.6.1 Frame rate and flux capability

One of the main performance parameters of an imaging detector is the frame rate, depending on the readout time. The possibility to read out the detector at high frequency implies that less time is required to perform the measurement (provided that a sufficiently intense radiation source is available). In many applications this feature is of crucial importance. For example, the opportunity to perform a full CT scan in the least achievable time would minimize motion artifacts in the reconstructed images, like those caused by the heart beating of the patient.

In Medipix and Timepix chips the frame rate is constrained by the matrix readout time. The effective frame rate then also depends on the speed of the full readout chain. In Medipix2 and Timepix, the fastest scheme is realized when the pixel matrix is read out in eight parallel blocks and frame rates over 1000 fps are achieved.

Medipix3 presents one mode of operation with virtually zero dead time, called Continuous Read Write. In this case one of the two pixel counters is read out while the other is working in counting mode. The time it takes to read out each counter depends on the counter depth, which can be set by the user. This value sets the maximum frame rate (or, equivalently, the minimum shutter time) that can be achieved with zero dead time.

Higher frame rates also imply that in order to obtain the same signal-to-noise ratio, the radiation flux has to increase accordingly. However, a detector has a limited flux capability. In Medipix and Timepix chips this is given by the dead time of the pixel preamplifier, which, for Medipix2 and Timepix is less than 1 μs for an injected charge below 20 ke$^-$, corresponding to maximum fluxes above 1 MHz/pixel ($>$ 30 GHz/cm^2) for photons below $\sim$70 keV. The flux capability could be increased in future designs by reducing the size of the pixels, which, however, will make charge sharing effects more relevant.

2.6.2 Energy resolution

A crucial property of a spectroscopic detector is the energy resolution, which is substantially driven by the sensor material. To the intrinsic resolution of the sensor, one has to add the noise from the threshold fluctuation and, in the case of Timepix, the clock frequency in the Time-over-Threshold measurement.

Values of the energy resolution for a typical 300 μm thick silicon read out by Medipix or Timepix are in the order of 1.5 keV FWHM for energies below 40 keV. In Timepix, the energy resolution of the ToT mode of operation is between 10% and 15% in the energy range from 5 to 30 keV (see also section 3.5.1).

2.6.3 Time resolution in Timepix

For Timepix, an important performance parameter is the time resolution, which affects the uncertainty on the energy measurements in ToT mode and on the time of arrival measurement in ToA mode. This latter directly influences the error on the z coordinate determined in a time projection chamber [14] or on the mass-to-charge ratio in a time-of-flight mass spectrometer [34].

The time resolution is defined by the frequency of the Timepix clock and by the effect of time walk. The maximum clock speed of 100 MHz corresponds to a 10 ns resolution. The challenge of bringing the time resolution down to 1.6 ns has been addressed in the design of Timepix3 [29]. Furthermore, in Timepix3 Time-of-Arrival and Time-over-Threshold information can be measured simultaneously, giving the possibility to correct for time walk.

2.6.4 Noise floor

The position of the noise floor determines the minimum energy value at which the threshold can be set. For Medipix2, this value is at around 3.9 keV, with a threshold variation throughout the matrix of 430 eV. For Timepix, the minimum threshold is at 2.7 keV, with a threshold variation of 126 eV.

For X-ray imaging applications, having a low noise floor is especially advantageous when the sample contains X-ray soft material, for which contrast is obtained via the low energy part of the source spectrum.

2.6.5 Dynamic range

In many applications, the radiation flux reaching the detector is strongly dependent on the position. Given the same exposure time, the number of quanta detected by different pixels may vary over several orders of magnitude. In X-ray imaging applications, this happens when the sample presents a very heterogeneous material composition and distribution, causing substantial differences in the absorption of the incoming spectrum depending on which part of the object is traversed by the radiation.

The dynamic range of a detector is a measure of how it is capable to handle this situation. If the dynamic range is low, the most exposed pixels will saturate before the less exposed ones could have reached a sufficient statistics.

The dynamic range of Medipix and Timepix is defined by the depth of the pixel counters. In Medipix2, up to 11810 single quanta can be counted during a single exposure. This property represents one of the strongest improvements with respect to conventional X-ray technologies. In the future, the possibility to increase the density of the electronic components in the pixel area could be exploited to extend the counter depth even further.

Chapter 3

Spectral sensitivity

Spectroscopic X-ray imaging detectors that will be used in this thesis consist of a semiconductor pixel sensor readout by a Medipix or Timepix chip.

In order to explain how signals are formed in the sensor, this chapter begins with an overview on the principles of charge formation and transport. Successively, the benefits of spectral capability in X-ray imaging applications are presented. The focus then moves to technical aspects of threshold calibration of Medipix based semiconductor detectors and of the Time-over-Threshold calibration in Timepix, using fluorescence X-ray emission from metal targets.

3.1 Semiconductor detectors

3.1.1 Principle of operation

When energy is released in a semiconductor by the interaction of an ionizing particle, electrons-hole pairs can be created. In contrast to gaseous detectors, where charge multiplication is needed in order to produce a detectable signal, in semiconductors the amount of charge that is generated can be detected by an appropriate front-end amplifier. In silicon, the average energy needed to create a pair is 3.6 eV, which means that one thousand charge carriers are created on average already by X-rays of 3.6 keV of energy.

However, if nothing is done to prevent the charges to recombine, no signal is formed. This can be avoided by applying an external electric field, which separates the two carrier types by drifting them in opposite directions. The overall motion of charges induces an electric signal on the electrodes, which can be measured and processed by the readout electronics. To suppress dark currents created by the thermal generation of electron-hole pairs, a pn junction structure can be produced in the crystal volume by doping the material with donor and acceptor impurities. By reverse biasing the junction, the depletion layer can be extended to enlarge the sensitive area of the detector. When all the sensor volume is depleted, increasing further the bias voltage results in an increase of the electric field, thus in a decrease of the drift time, which makes the detector faster.

3.1.2 Charge carriers transport

The shape of the signal seen by the front-end electronics is determined by the physics governing the motion of the charge carriers created in the sensor material. This motion is described in the framework of the theory of transport in terms of a few fundamental phenomena.

Thermal motion

The physics at thermal equilibrium gives an idea of the order of magnitude of the quantities involved in the description of the carrier motion.

At equilibrium, charge carriers in the sensor medium can be approximately considered as free moving, and can be treated as a non-interacting Boltzmann gas of particles with effective mass m^*, randomly scattering with the lattice sites. Electron and holes are described in terms of two separate mass values, m_n^* and m_p^* respectively.

At temperature T, the absolute velocity v of the particles is distributed according to the Maxwell-Boltzmann probability density function

$$f_{MB}(v) = \sqrt{\frac{2}{\pi}} \left(\frac{m^*}{k_B T} \right)^{3/2} e^{-\frac{m^* v^2}{2 k_B T}} v^2, \tag{3.1}$$

where k_B is the Boltzmann constant. This yields an average thermal velocity

$$v_{th} = \sqrt{\frac{3 k_B T}{m^*}}. \tag{3.2}$$

This formula means that the kinetic energy $1/2 m^* v_{th}^2$ equals the thermal energy $3/2 k_B T$. On average, the net distance traveled by an ensemble of many carriers is zero.

In case of silicon, v_{th} for both electrons and holes is of the order of 10^5 m/s at room temperature. Since the mean free path between two consecutive collisions is around 100 nm, this corresponds to a relaxation time (i.e., mean time between two consecutive collisions) in the order of 1 ps [56].

The transport equation

Deviations from equilibrium can be caused by the presence of electric fields and concentration gradients. These conditions are described by five equations [57]:

- the Poisson equation

  $$\nabla^2\phi(\vec{x}) = -\frac{Q(\vec{x})}{\epsilon} \tag{3.3}$$

  relates the electric potential $\phi(\vec{x})$ to the free charge density $Q(\vec{x})$ through the dielectric constant ϵ and describes the effect of the space charge electrostatics;

- the expressions of the electrons and holes current densities as a function of the diffusion constants D and the drift mobilities μ:

  $$\vec{J}_n(\vec{x}) = eD_n\vec{\nabla}n(\vec{x}) + e\mu_n n(\vec{x})\vec{\mathcal{E}} \tag{3.4}$$

  $$\vec{J}_p(\vec{x}) = -eD_p\vec{\nabla}p(\vec{x}) + e\mu_p p(\vec{x})\vec{\mathcal{E}} \tag{3.5}$$

  in an electric field $\vec{\mathcal{E}}$, where $n(\vec{x})$ and $p(\vec{x})$ are the electron and hole concentrations and e is the elementary electric charge;

- the continuity equations, stating that the divergence of the current densities must be balanced by the volume recombination and generation rates $r(\vec{x})$ and $g(\vec{x})$:

  $$\vec{\nabla}\cdot\vec{J}_n(\vec{x}) = e\left[r_n(\vec{x}) - g_n(\vec{x})\right] \tag{3.6}$$

  $$\vec{\nabla}\cdot\vec{J}_p(\vec{x}) = -e\left[r_p(\vec{x}) - g_p(\vec{x})\right]. \tag{3.7}$$

The transport equations for electrons and holes are obtained by applying the continuity conditions 3.6 and 3.7 to equations 3.4 and 3.5 respectively:

$$D_n\nabla^2 n(\vec{x}) + \mu_n\vec{\mathcal{E}}(\vec{x})\cdot\vec{\nabla}n(\vec{x}) + n(\vec{x})\mu_n\vec{\nabla}\cdot\vec{\mathcal{E}}(\vec{x}) - \left[r_n(\vec{x}) - g_n(\vec{x})\right] = 0 \tag{3.8}$$

$$D_p\nabla^2 p(\vec{x}) - \mu_p\vec{\mathcal{E}}(\vec{x})\cdot\vec{\nabla}p(\vec{x}) - p(\vec{x})\mu_p\vec{\nabla}\cdot\vec{\mathcal{E}}(\vec{x}) - \left[r_p(\vec{x}) - g_p(\vec{x})\right] = 0 \tag{3.9}$$

The full solution of the problem of transport is found by solving equations 3.8 and 3.9 together with the Poisson equation 3.3. However, this cannot be done analytically. In the following paragraphs each term of the transport equations will be treated separately, and each process will be described individually.

Carriers generation and recombination

The right hand sides of equations 3.6 and 3.7 describe the change in time of the concentrations of electrons and holes respectively, due to the interplay of the generation and recombination processes. With a simple model, it can be shown that, at equilibrium, the recombination process for each carrier type is described by two separate equations [61, 56]:

$$\frac{d(\delta n)}{dt} = -\frac{\delta n}{\tau_n} \tag{3.10}$$

and

$$\frac{d(\delta p)}{dt} = -\frac{\delta p}{\tau_p}, \tag{3.11}$$

where the two characteristic times τ_n and τ_p are defined through the recombination rate r as

$$\tau_n = \frac{1}{rp} \tag{3.12}$$

and

$$\tau_p = \frac{1}{rn}. \tag{3.13}$$

This result shows that as soon as the generation process ends, the thermal equilibrium is reached again as the consequence of a transient state in which recombination causes the exponential decrease of the concentration of carriers. If no driving force is present that separates the electrons from the holes, these would recombine within a time interval of the order of τ_n and τ_p respectively, that, according to relations 3.12 and 3.13, depend on the intrinsic carriers concentration. In a depleted pn junction, the charge carriers are driven away from the depletion region, and recombination is suppressed.

Although this simple model is useful for forming an idea on the basics of the generation and recombination processes, the real case is much more complicated.

For example, other processes involving intermediate states in the band energy gap (due to imperfections and impurities) play a role, acting as generation-recombination centers, and in indirect semiconductors (such as silicon) the shift between the conduction and the valence band in the reciprocal lattice has to be taken into account.

Diffusion

Once created, the charge carriers are affected by the presence of a concentration gradient, and tend to move towards the region in which the concentration is lower. Diffusion takes place in the low concentration regime[1] according to Fick's law:

$$\vec{J}_{diff} = -D\vec{\nabla}C. \tag{3.14}$$

This equation corresponds to the intuitive representation of the phenomenon that the diffusion current $\vec{J}_{diff} \propto \vec{v}$ describes a flow of particles at velocity $\vec{v}$ in the direction opposite to the gradient of the concentration $C = C(\vec{x}, t)$, where $C(\vec{x}, t)$ is the concentration at a given position $\vec{x}$ at time t. The diffusion constant D specifies the strength of the effect of the gradient on the current.

Although this model strictly concerns the situation of particles suspended in a fluid, it can also be applied in the case of charge carriers within a crystal lattice in the approximation of an isotropic and homogeneous medium.

The most general solution of equation 3.14 can be worked out by requiring mass conservation, i.e. by applying the continuity equations 3.6 and 3.7. The evolution of the carrier concentration in space and time, starting from an initial distribution $C_0(\vec{x})$, then takes the form[2]

$$C(\vec{x}, t) = \frac{1}{8\,(\pi D t)^{3/2}} \int C_0(\vec{x}')e^{-\frac{(\vec{x}-\vec{x}')^2}{4Dt}}\,d^3x'. \tag{3.15}$$

A special case is given when the initial size of the charge cloud is so small that the concentration at time $t = 0$ can be approximated by a Dirac distribution around the generation point $\vec{x}^0$:

$$C_0(\vec{x}^0) = \delta(\vec{x} - \vec{x}^0). \tag{3.16}$$

---

[1] If concentrations are high, the problem is that of the dynamics of two fluids [40].

[2] See, for example, [40] for the derivation of 3.15 from 3.14.

Then 3.15 reduces to

$$C(\vec{x}-\vec{x}^0,t)=\frac{1}{8\left(\pi Dt\right)^{3/2}}e^{-\frac{\left(\vec{x}-\vec{x}^0\right)^2}{4Dt}}, \tag{3.17}$$

showing that, in absence of any external force, the particles diffuse isotropically according to a Gaussian distribution whose spread

$$\sqrt{\langle x^2\rangle}=\sqrt{2Dt} \tag{3.18}$$

increases with the square root of time.
An order of magnitude evaluation of the effect can be carried out by setting $t=\tau$, $\sqrt{\langle x^2\rangle}=\lambda$ and $v_{th}=\lambda/\tau$, where τ and λ represent the relaxation time and the mean free path respectively. For the diffusion constant this gives

$$D=\frac{1}{2}v_{th}\lambda, \tag{3.19}$$

which, through equation 3.2, shows the dependence of D on the temperature.

Typical values of the diffusion constant D in semiconductors at room temperature are in the order of few tens of cm^2/s, thus yielding a standard deviation $\sqrt{\langle x^2\rangle}$ in the order of few micrometers [56].

Drift

The presence of a force field is another means of altering the thermal equilibrium. This situation is typical in particle detection systems, where the application of an external electric field in the sensitive volume is necessary in order to drive the charges to the collection electrode.

The effect of the external force is to accelerate each carrier along the field lines between two consecutive collisions. After an average distance λ the particle will scatter with the lattice and in this process it will release almost all the energy acquired during the acceleration. Overall, the particle will appear as moving at a constant drift velocity $\vec{v}_{drift}$.

A simple way to treat the drift mechanism is to model it as a uniform acceleration with a friction term [9, 39], in which case the Langevin equation holds

$$m^*\frac{d\vec{v}}{dt}=\pm e\vec{\mathcal{E}}-K\vec{v}, \tag{3.20}$$

with $\vec{\mathcal{E}}$ being the electric field vector, $\vec{v}$ the instantaneous velocity of the particle and K the friction constant. The sign ± must be chosen according to the electric charge of the carrier: + for the holes, - for electrons.

Equation 3.20 defines a characteristic time scale through the ratio $\tau_d = m^*/K$ that can be interpreted as the average time between two successive collisions. In the $t \gg \tau_d$ limit the velocity saturates at

$$\vec{v}_{drift} = \pm \frac{e\tau_d}{m^*} \vec{\mathcal{E}}. \tag{3.21}$$

This relation states that the observed drift velocity $\vec{v}_{drift}$ is proportional to the electric field

$$\vec{v}_{drift} = \pm \mu \vec{\mathcal{E}}, \tag{3.22}$$

with

$$\mu = \frac{e\tau_d}{m^*}. \tag{3.23}$$

The μ parameter is called the scalar mobility of the carriers, and in the low field regime it is constant. Definition 3.23 shows that the mobility is a function of τ_d and m^*, so depending on the temperature and on the properties of the medium.

For a rough idea of the orders of magnitude, for pure silicon at 300 K the mobility is $\mu_n = (1415 \pm 46)$ cm^2/(Vs) for the electrons and $\mu_p = (480 \pm 17)$ cm^2/(Vs) for the holes [56].

This model is a good approximation as long as low intensity fields are considered, in which case only classical elastic scattering between the carriers and the lattice occur and equation 3.20 is valid. As the electric field is increased, a quantum mechanical treatment is required, where the interaction with the crystal lattice is described in terms of scattering with phonons. As a result, the mobility is not constant [56].

Coulomb interactions

Charge carriers interact among each other through electrostatic forces. The cloud of electrons (or holes) that is drifting towards the collection electrode thus expands more rapidly than if just diffusion alone is considered.

To incorporate Coulomb interactions, the transport equations must be solved simultaneously with the Poisson equation. This corresponds to the inclusion of an additional term

$$\frac{\partial Q}{\partial t} = -\frac{\mu Q}{4\pi\epsilon r^2} \frac{\partial Q}{\partial r} \tag{3.24}$$

to the transport equation [25]. Here $Q(r,t)$ is the charge density in radial coordinates, μ is the carrier mobility and ϵ is the dielectric constant of the medium. The charge density is related to the concentration through the elementary charge of the carrier: $Q(r,t) = qC(r,t)$.

If N_p is the total number of carriers, the solution of equation 3.24 is

$$C(r,t) = \begin{cases} \frac{\epsilon}{q\mu t}, & \text{if } r < r_0 \\ 0, & \text{if } r > r_0 \end{cases}, \tag{3.25}$$

with

$$r_0 = \sqrt[3]{\frac{3\mu q N_p t}{4\pi\epsilon}}. \tag{3.26}$$

Formula 3.25 shows that at any time during expansion the charge density always has a constant value inside a sphere of radius r_0. The net effect of electrostatic repulsion is to increase the spread of the charge carriers distribution with respect to that expected from pure diffusion. In several papers it was proven that this effect cannot be neglected in a number of circumstances (see for example [25] and [22]).

Energy resolution and the Fano statistics

The number of charge carriers created by the interaction of an ionizing particle is of statistical nature and is therefore subject to fluctuations. Since the amount of charge created is ultimately a measurement of the released energy, these fluctuations determine the intrinsic limit on the spectral resolution of the detector.

It turns out that, if calculated on the basis of a purely statistical approach, the energy resolution of a detector is worse than the one that can be measured experimentally. The reason for this was first explained by U. Fano as due to correlations of different mechanisms through which the energy of the particle can be transferred to the medium [23].

Intuitively, this corresponds to the fact that if an amount of carriers $N - \delta N$, different from the expected value N, are created in a certain position in the sensor, then the exceeding part δN has to be statistically averaged out in the next collisions. The effect is strong for the case of photoelectric conversion of photons, where the number of carriers created has to fulfill the constraint that all the initial energy has to be used[3].

This results in the definition of the Fano factor

$$F = \frac{\sigma_p^2}{N_p}. \tag{3.27}$$

In this formula N_p is the number of pairs created and σ_p^2 is the associated variance. The Fano factor is an indication of how much the width of the distribution deviates from the ideal Poisson limit $\sigma_p^2 = N_p$, corresponding to $F = 1$. Typical values for semiconductors are in the order of $F = 0.1$ [56].

3.1.3 Signal formation

The instantaneous current induced on the electrode can be calculated with the weighting field method according to the Shockley-Ramo theorem [60, 52, 30]. The Shockley-Ramo theorem demonstrates that the instantaneous charge induced on the electrodes only depends on the location of the space charge and on the geometry of the electrodes, but neither on the geometrical distribution of the carriers, nor on the voltage applied to the electrodes[4]. When applied to semiconductors, the theorem also shows that the total signal created from the motion of electron and holes in opposite directions is the sum of the signals associated with either carrier types.

Measurement of energy

The principle of energy sensitivity in spectroscopic pixel readouts for semiconductor detectors, such as Medipix and Timepix, relies on the assumption that the amount of charge induced on the readout electrode corresponds to the energy released by the ionizing particle in the sensor. This assumption is correct only if all the charge that is initially created contributes to the formation of the signal.

This condition does not hold anymore if part of the charge is lost during the drift process. Recombination and trapping centers can be present in the detection volume for example due to imperfections of the crystal lattice that are caused by the non-optimal processing of the sensor material or to damages

---

[3] Not all the initial energy, though, is converted into electron-hole pairs. The difference between the excitation energy (3.6 eV per pair, on average, in silicon) and the band-gap energy (1.1 eV in silicon) is converted into heat.

[4] As a matter of fact, some detectors can be operated without an applied sensor bias.

induced by radiation effects. If these centers are not localized, but they are present in all the drift volume, the amount of charge that is lost depends on the length of the drift path: the longer the carriers have to travel in the sensor, the more likely the chance is that they will recombine or get trapped. As a consequence, a detector relying on the estimation of charge to infer the energy released in the sensor measures a different energy according to where the interaction takes place [56].

If one excludes radiation damage, the occurrence of imperfections in silicon sensors is very low, thanks to the fact that the production of silicon crystals is a very well established process, and very high quality wafers can be grown. Among the results that will be presented in chapter 4, it will be shown (figure 4.13) that charge loss is not an issue for the 300 μm thick silicon sensors employed to build Medipix based spectroscopic X-ray detectors. This means that with these devices energy measurement can be performed reliably.

Signal induced on segmented electrodes

If the size of the electrode is much larger than the sensor thickness, then one talks of a pad detector. The resulting weighting potential grows linearly as a function of depth, which eventually implies that the charge induced on the electrodes is the same independently from the position of the carriers along the drift path. At the same time, the instantaneous induced current changes according to the variation of the drift velocity as a function of the value of the electric field.

The situation is different for the case of finely segmented electrodes, as in pixel detectors[5], where the size of the collection electrode is comparable or smaller than the sensor thickness. In this case the weighting potential is close to 1 only in a region in the vicinity of the segmented electrode, while it rapidly approaches zero in the rest of the sensor volume. The high weighting potential region is smaller as the aspect ratio of the electrode (i.e. the pixel size compared to the sensor thickness) becomes smaller.

This situation gives rise to the so called small pixel effect, characterized by two features: 1) the major contribution to the induced signal arises from the last part of the drift process, namely when the charge is located close to the collection electrode, and 2) the contribution to the signal from the charge carriers of the other type, i.e. those drifting towards the other electrode(s), is negligible.

---

[5] The following considerations also apply to strip detectors

Small pixel effects are particularly relevant in the case of energy sensitive detectors, where a significant amount of charge can be lost before the carriers approach the collection electrode, i.e. the region where the largest fraction of the signal is induced [56].

Charge sharing

Another consequence of segmentation is that, as long as the charge carriers are still located far from the pixel electrode, they induce a measurable signal also on neighboring electrodes. This signal changes in sign as soon as the charge enters the vicinity of the collection electrode. As a consequence, only the pixel where the charge was created measures a net charge, while the neighbors see a null signal integral.

If the front-end electronics is provided with a charge sensitive preamplifier (as in Medipix and Timepix), charge sharing from induced signals has no effect, as long as the integration time is sufficient to cover the full signal development[6]. However, if the pixel size is small, namely if it is comparable with the transverse size assumed by the distribution of the charge carriers due to diffusion, charge sharing can be caused by the actual migration of charge from one pixel to its neighbors.

The effect is important for spectroscopic pixel detectors. Charge sharing, in fact, may cause less charge to be detected in a given pixel, which results in a lower value of the estimated energy. At the same time, the rest of the charge, which has leaked into the neighboring pixels, might be lost if it is not enough to exceed the detection threshold. This means that even re-summing the charge in a pixel cluster might not be enough to recover the original value of the deposited energy.

In the case of Medipix based semiconductor detectors for X-ray imaging, charge sharing produces serious distortions of the incoming spectra. The origin of these distortions can be understood by studying the charge transport properties of the sensor, which will be done in chapter 4.

3.1.4 X-ray detection vs photon detection with a hybrid pixel device

Figure 3.1 shows the principle of operation of a hybrid pixel semiconductor detector, in the case of the collection of holes. This type of detectors is the default device used for the measurements presented later.

---

[6] Collection times for a typical silicon detector are in the order of few nanoseconds [56].

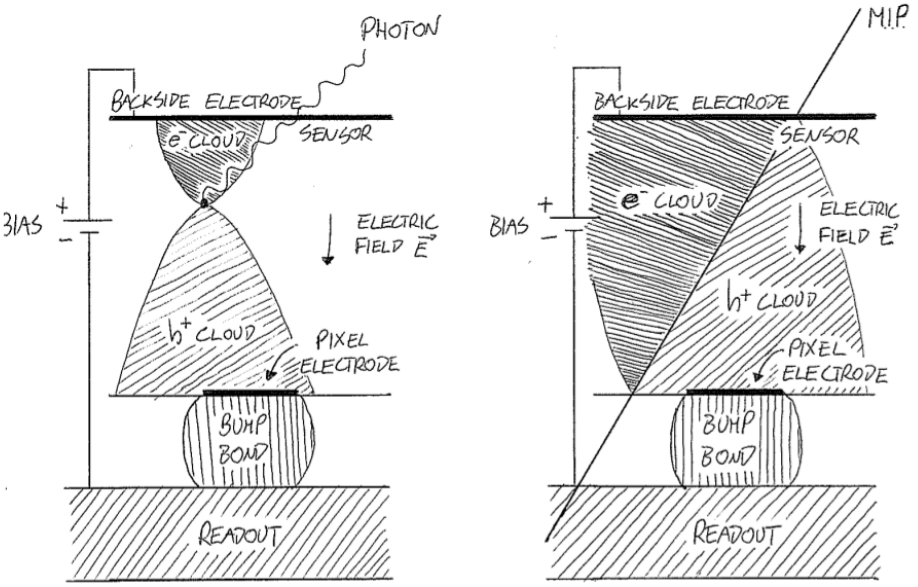

Figure 3.1: **Sketch of the detection principle for photons (left) and relativistic charged particles (right) in a hybrid semiconductor detector.**

The sensor carries a uniform back-metalization structure that serves as the anode, while the cathode is segmented in order to match the pixels of the readout chip. Connection between sensor and readout is done via bump bonding.

The two images show the difference between the detection of an X-ray photon and the detection of a relativistic charged particle. In the former case, when photoelectric effect takes place, all of the initial energy of the photon is used to excite an electron to the continuum, which then induces the creation of electron-hole pairs by ionizing the medium. Since the range of the photoelectron is usually in the order of a few microns, the initial cloud of charge carriers can be usually considered as point-like.

In the case of relativistic charged particles the energy loss is governed by the Bethe-Bloch ionization mechanism. The particle releases part of its total energy at each interaction with the sensing medium, resulting in the creation of a trail of electron-hole pairs along the full path. Minimum ionizing particles create an average of 70 pairs per micron in silicon.

If the spatial resolution of the detector is sufficient, the original trajectory of the particle in the sensor can be reconstructed from the data. This strategy is at the basis of the analysis that will be presented in chapter 4.

3.2 Spectral X-ray imaging with Medipix

The principle of the spectral sensitivity of chips of the Medipix and Timepix family is the possibility to preset a threshold on the signal induced by the detection of a single particle or photon. The height of the signal is proportional to the amount of charge reaching the pixel electronics, and corresponds to the energy released by the ionizing particle in the sensor.

In the case of low energy X-ray quanta, where the most probable type of interaction is the photoelectric effect, the detected signal is proportional to the energy of the photon[7]. As a result, the Medipix programmable threshold provides a selection on the photon energy. This feature makes spectroscopic readout chips, like Medipix and Timepix, unique. X-ray images can be taken at different energy thresholds (or in different energy bins in the case of energy window operation), thus enhancing contrast for different materials in the sample as a consequence of the different energy dependence of the respective photon attenuation. This result cannot be achieved with conventional energy integrating detectors, where spectral information is lost.

An example of the multiple threshold imaging concept is shown in figure 3.2 for three X-ray images of an operational amplifier, taken with a 300 μm silicon sensor bump bonded to a Timepix chip. The detector threshold was tuned at 5, 10 and 27 keV, respectively. As a consequence, in each image the relative contrast between the different materials (plastic, metal and air) changes, thus enhancing material separation. Despite its simplicity, this example already shows the underlying idea of spectral, material-resolved, X-ray imaging. The multiple threshold imaging approach will be the basis of the spectral CT method that will be developed in chapter 6.

With Medipix2 and Timepix, the multiple images are acquired by repeating the measurement at different thresholds. This means that the total measurement time, as well as the dose delivered to the sample, increases. This problem is solved in Medipix3, where the spectroscopic mode of operation provides eight simultaneous thresholds at 110 μm pixel pitch, which means that eight measurements with eight different threshold settings are performed within a single exposure.

---

[7] At least when no charge sharing effects are considered.

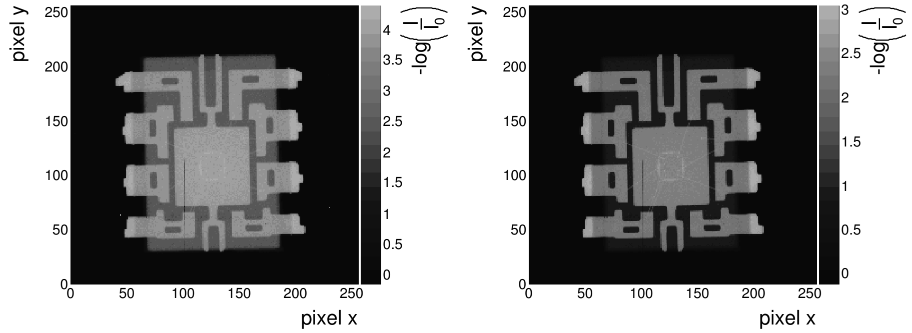

(a) **Threshold at 5 keV.**

(b) **Threshold at 10 keV.**

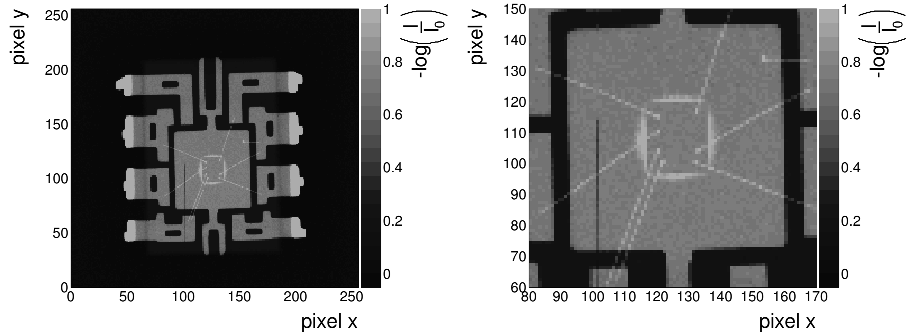

(c) **Threshold at 27 keV.**

(d) **Threshold at 27 keV, zoom on the wire bonds region.**

Figure 3.2: **X-ray images, in units of $-log\,(I/I_0)$, of an operational amplifier taken at multiple thresholds.**

3.3 Threshold calibration

To determine the relation between the threshold setting and the real energy, a calibration procedure is required. Threshold calibration can be performed by exposing the detector to radiation sources of known energy. Among all the possibilities, one could employ natural gamma emitters, synchrotron radiation or fluorescence emission from pure metals excited by an external field.

This latter represents the most convenient method for multiple reasons. First, a fluorescence setup can be easily built by equipping a conventional table-top X-ray imaging system with little additional mechanics. Moreover, since fluorescence yields are relatively high (see appendix C [36, 41, 4]), radiation fluxes at the detector can be high enough to allow for calibration of individual pixels in a reasonable time[8].

Other advantages of using fluorescences is that many monochromatic photopeaks can be detected over a wide range of X-ray energies, from below 1 keV up to above 100 keV, depending on the target material.

3.3.1 Experimental setup

A sketch of a typical fluorescence calibration setup is shown in figure 3.3. The primary beam from a vacuum X-ray tube is directed onto a target material, that re-emits part of the absorbed radiation as X-rays at characteristic energy values. The fluorescence photons are emitted isotropically. To maximize the flux of fluorescence radiation reaching the detector over the flux of the primary radiation, the detector is positioned outside the primary beam, as shown.

The set of targets used for calibration is listed in table C.1 in appendix C, along with some relevant properties. All of them are high purity metal foils, mostly of 0.001 inch thickness.

3.3.2 Model of fluorescence spectra

The photons reaching the detector build up a spectrum $S(E)$ characterized by the presence of fluorescence photopeaks on a background formed by the radiation scattered inside the setup and the radiation backscattered from the target. An analytical model of the fluorescence spectrum is developed to fit the data in order to determine the calibration points.

---

[8] This depends on the power of the X-ray tube

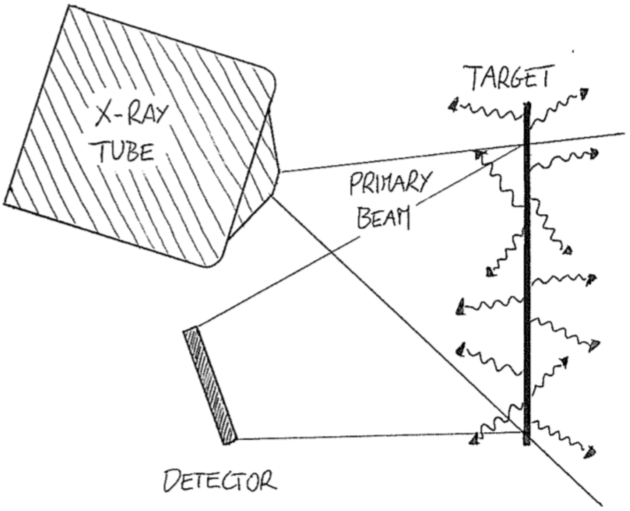

Figure 3.3: **A sketch of the fluorescence calibration setup.**

Figure 3.4 shows an intuitive sketch of the model. An originally monochromatic photopeak (figure 3.4a) at energy E_p is broadened by the detector resolution according to a Gaussian profile (figure 3.4b), i.e.

$$S_p(E) = \frac{dN_p}{dE}(E) = \frac{N_p}{\sqrt{2\pi}\sigma_p} e^{\frac{(E-E_p)^2}{2\sigma_p^2}} . \tag{3.28}$$

Here N_p denotes the number of photons that are detected during the measurement time and σ_p is the width of the distribution.

Due to charge sharing, a fraction f_{cs} of the incoming photons is detected at lower energies. This effect produces a continuous tail in the spectrum at $E < E_p$. In the vicinity of the peak, this tail can be approximated by a constant (figure 3.4c). Taking into account the effect of the energy resolution, the charge sharing component of the spectrum can thus be written as

$$S_{cs}(E) = \frac{dN_{cs}}{dE}(E) = \frac{f_{cs} N_p}{2} \left[1 + \mathrm{Erf}\left(-\frac{E-E_p}{\sqrt{2}\sigma_p} \right) \right] . \tag{3.29}$$

The total spectrum is the sum of S_p and S_{cs}, plus a possible background component $S_b(E)$. In an energy range around of the photopeak this latter can

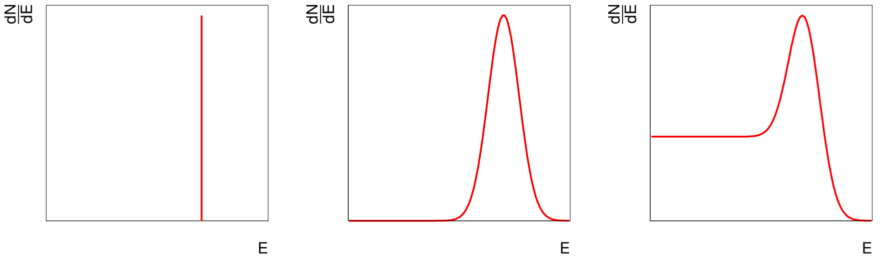

(a) **Monochromatic input**

(b) **Effect of the energy resolution**

(c) **Effect of charge sharing**

Figure 3.4: **The model used to describe the spectral response of a Medipix based semiconductor detector.**

be taken as a constant contribution $S_b(E) = C_b = const.$ Putting all terms together results in

$$S(E) = S_p(E) + S_{cs}(E) + C_b. \tag{3.30}$$

This formula contains 5 free parameters: E_p, σ_p, N_p, f_{cs} and C_b.

Despite its simplicity, formula 3.30 is well suited for fitting the data in the vicinity of the photopeak. A better parametrization of the detector energy response, and in particular of the charge sharing tail, will be addressed in chapter 5.

Inclusion of the K_β component

The energy resolution is such that in many cases the fluorescence spectrum shows the contribution of the K_β peak alongside the more intense K_α line. For a conventional 300 μm silicon sensor on Medipix, this is the case for all the targets with atomic number $Z \geq 32$ (from germanium on in our set of targets), for which the distance between the two peaks is larger than ~1 keV. In such circumstances, the detected spectrum in a close neighborhood of the characteristic lines is given by

$$S(E) = S_p^\alpha(E) + S_{cs}^\alpha(E) + f_{\beta/\alpha}\left[S_p^\beta(E) + S_{cs}^\beta(E)\right] + C_b, \tag{3.31}$$

where now the superscripts α and β are applied on $S_p(E)$ and $S_{cs}(E)$ to distinguish the two peak positions E_p^α and E_p^β, and $f_{\beta/\alpha}$ is the relative intensity of the K_β radiation with respect to the K_α component.

Notice that in first approximation, the σ_p and f_{cs} parameters are shared between the α and β contributions. This choice stems from the assumption that, within the energy range considered, the resolution of the detector and its spectral response do not vary significantly. As a result, despite the increase in complexity, the spectrum 3.31 only leaves 7 free parameters: the energy E_p^α of the K_α peak, the energy E_p^β of the K_β peak, the intensity N_p, the detector resolution σ_p, the charge sharing scalar f_{cs}, the K_β to K_α relative intensity $f_{\beta/\alpha}$ and the background constant C_b.

3.3.3 Calibration procedure

The calibration curve can be built by measuring the fluorescence spectrum from different targets and by correlating the position of the photopeaks with the known emission energies.

A common technique to measure a full energy spectrum with Medipix based detectors is to perform a threshold scan, i.e. monotonically varying the threshold in fine steps during the exposure. The result is a cumulative representation of the source spectrum that can later be retrieved by differentiating the scan. However, differentiation leads to an amplification of the stochastic noise, which in most cases results in a poorly defined spectrum. This is particularly true when considering that the calibration procedure is carried out on a per-pixel basis, where the typical statistics are limited to 100-1000 photon counts at the lowest threshold. To avoid differentiation, the integral expressions of formulas 3.30 or 3.31 can be fitted directly to the raw threshold scan. Notice that the resulting formulas are still analytical.

Convergence of the fit might strongly depend on the initialization values of the parameters. This is especially true when the full 7-parameters model 3.31 is employed to fit both the K_α and the K_β peaks. Manual fine tuning is impractical when the full pixel matrix has to be calibrated.

To maximize the number of pixels for which the fit converges, the fitting procedure is organized in successive steps in which an initial model function depending on few parameters is progressively developed until the final form 3.30 (or 3.31) is reached, and where each step is initialized using the results from the previous estimation. For details about this procedure, see appendix D.

Figure 3.5 illustrates an example of a single pixel calibration of the lower threshold (THL) for a Medipix2 based silicon detector. Figure 3.5a shows the fit of the single peak expression 3.30 to the cumulative spectrum from a nickel target, while figure 3.5b, shows the fit of the double peak expression 3.31 to the

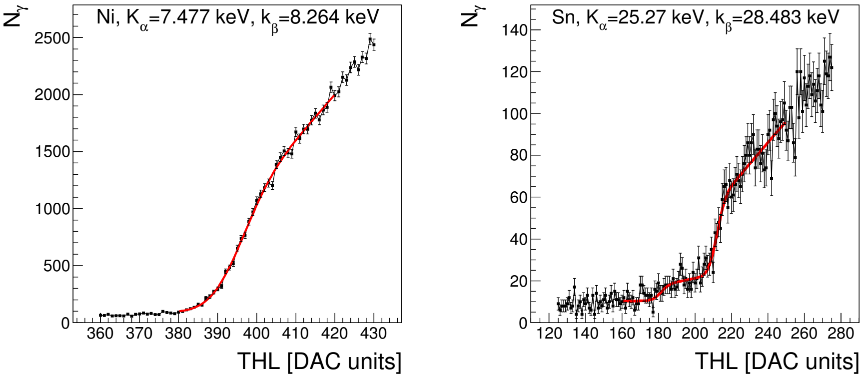

(a) **Fit of function 3.30 to the cumulative spectrum of nickel fluorescence.**

(b) **Fit of function 3.31 to the cumulative spectrum of tin fluorescence.**

χ^2/ndf	70.88 / 84
Prob.	0.84
$N_p f_{cs}$ [keV^{-1}]	0.18 ± 0.05
E_p^β [keV]	181.1 ± 2.0
σ_p [keV]	3.6 ± 1.7
f_{cs}	0.025 ± 0.008
C_b [keV^{-2}]	10.4 ± 0.8
$N_p f_{\beta/\alpha}$ [keV^{-1}]	4.6 ± 0.9
E_p^α [keV]	211.9 ± 0.9

(c) **Results from the fit in figure 3.5b.**

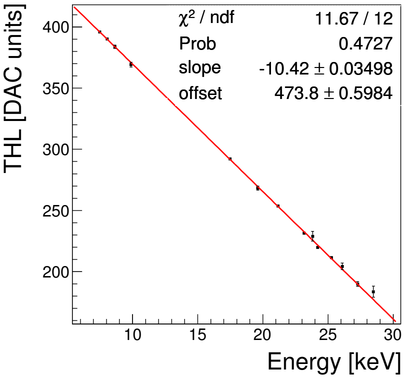

(d) **Calibration curve for the same pixel, fitted with a first degree polynomial.**

Figure 3.5: **Example of the calibration of a single pixel for a silicon Medipix detector.**

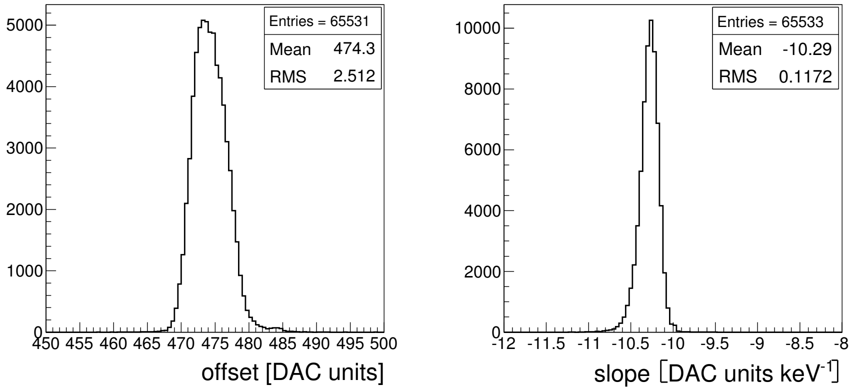

(a) **Offset**

(b) **Slope**

Figure 3.6: **Distributions of the calibration line parameters (offset and slope) for all the pixels in the detector.**

cumulative spectrum from a tin target. The results of this latter fit are shown in figure 3.5c.

Finally, the full calibration curve for the same pixel is shown in figure 3.5d. In this plot each point corresponds to the K_α or the K_β peak from one of the employed targets. The data are fitted with a first degree polynomial. The distributions of the calibration parameters (offset and slope of the calibration line) over the full pixel matrix are shown in figure 3.6.

3.4 Threshold equalization

Although pixels are designed to be exact copies of each other, small variations unavoidably occur because of systematic and environmental causes that affect the manufacturing process. One of the parameters that suffers from inter-pixel mismatches in Medipix and Timepix is the discriminator threshold: while pixels are expected to operate all at the same energy threshold, variations are observed throughout the pixel matrix.

The threshold equalization is the procedure that aims at minimizing this dispersion by fine tuning the threshold in each pixel. This is accomplished by setting the values of the adjustment bits of the discriminator(s) in each pixel (3

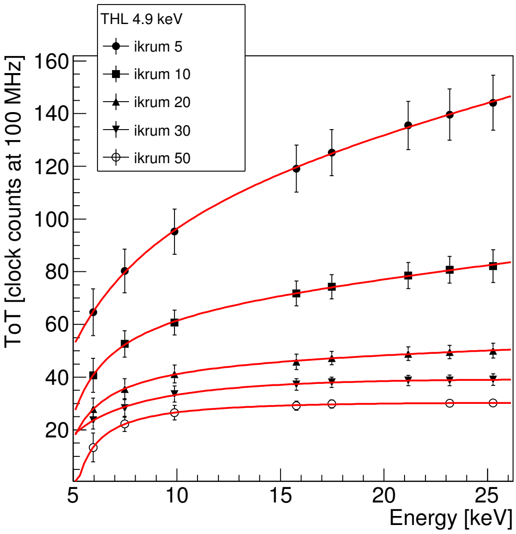

Figure 3.7: **ToT calibration curves for different values of the Krummenacher leakage compensation current (Ikrum, see appendix B).**

bits for Medipix, 4 for Timepix).

By definition, the most effective equalization strategy is the one that exploits the per-pixel calibration to calculate the actual energy threshold of each pixel. However, this procedure is often impractical, since it requires a full characterization of the detector energy scale, which is too time consuming for most applications.

As an alternative, the equalization can be performed by exploiting the position of the noise floor of the pixels. This approach is indeed faster and easy to perform, but the result is effective only as long as the detector is operated at low thresholds. In fact, this method only equalizes the threshold offset, while it doesn't take into account the inter-pixel gain variations. When the threshold is set further and further from the noise floor, the equalization gradually worsens.

3.5 Calibration of the Timepix ToT

When operated in photon counting mode, the Timepix chip is equivalent to the Medipix chip, with the difference that only one threshold is available instead of two (Medipix2) or more (Medipix3 in spectroscopic mode).

However, as far as other applications are concerned, Timepix strongly differs from Medipix in that spectral sensitivity can be achieved by operating the chip in Time-over-Threshold mode. In this case, energy estimation can be performed directly on single quanta by measuring the time the signal stays above threshold.

The calibration of the Time-over-Threshold scale requires a dedicated technique, aimed at minimizing the effect of pile-up, arising from the fact that the Timepix logic is designed in such a way that the Time-over-Threshold values of signals that exceed the threshold within the same shutter time are integrated. This implies that, when multiple signals are detected in the same pixel within the shutter time, the information on the energy associated to individual quanta is lost. Under these circumstances, the possibility of a calibration is hindered.

As with the case of the threshold calibration, the Time-over-Threshold calibration can be performed using X-ray fluorescence. In order to acquire energy information on single photons, the probability of more than one photon being detected in the same shutter time must be as low as possible. The simplest approach is to keep the radiation fluxes at low levels, so that the occupancy in a single frame is in the order of few percent. This implies that the measurements for a ToT calibration, especially when performed on a per-pixel basis, generally take much longer than those required for the calibration of the threshold.

The Time-over-Threshold spectrum can be retrieved by selecting only isolated events. A photon event is considered isolated when it triggers a single pixel and none of its first neighbors. This selection results in the minimization of the effect of charge sharing.

ToT spectra can be fitted directly with a Gaussian function in a range around the photopeak(s). The final calibration curve exhibits the typical shape shown in figure 3.7. The trend of the data can be parametrized in terms of a function of the form

$$ToT = aE + b - \frac{c}{E - E_0}, \tag{3.32}$$

where a and b are line parameters, while c and E_0 are the parameters of the inverse law describing the low energy part of the data.

3.5.1 Limitations of the ToT mode

Contrary to the simple application of a threshold, the Time-over-Threshold mode in Timepix is the only method that provides an actual energy measurement. The question that might arise at this point is: why not always exploit Timepix and the ToT to measure directly the full radiation spectrum in each pixel?

A first reason against this possibility is that the energy resolution in Time-over-Threshold is poorer than the resolution of the threshold itself. While the latter is basically driven by the noise of the discriminator only, the former is determined by a combination of factors, among which the settings of the leakage current compensation circuitry in the amplifier.

The second point is that, as explained in section 3.5, energy estimation on single quanta can be achieved only at the expense of the flux. One possibility to overcome this limitation is to reduce the shutter duration until, even at high fluxes, single signals are isolated within different shutter periods. However, in this situation the measurement period is dominated by the dead time. Even if this would be an acceptable condition, in order for a signal to exceed the threshold and fall back below in such a short time, its falling time should be reduced to such an extent that the resolution of the clock would be strongly impaired.

In addition, as it will be clear in chapter 6, at least in principle the solution of the spectral CT problem just requires the measurement of X-ray projections at multiple thresholds, without the need to determine the full spectrum.

ToT mode still remains a powerful approach for applications where lower fluxes are involved than in X-ray imaging, such as particle tracking or dosimetry. As a matter of fact, the performance of Timepix as a spectroscopic tracker of relativistic ionizing particles will be the key aspect of the sensor characterization analysis presented in section 4.1.

Chapter 4

The energy response function: particle beam data

The energy response function of a spectroscopic X-ray detector is one of the most important features that enter the image reconstruction algorithm in spectral X-ray computed tomography, as will be described in chapter 6.

In the previous chapter, a simple model of the detector response to fluorescence X-rays was introduced. This model is efficient for the purpose of fitting the calibration data in the vicinity of the photopeaks, but cannot fully characterize the energy response over the whole range. In particular, the shape of the charge sharing tail of the spectra is not described properly.

To understand how X-ray spectra are distorted by detector effects, the charge transport properties of the sensor need to be characterized. This chapter presents the analysis performed on data from an experiment with a relativistic charged particles beam, where the evolution of the lateral profile of the charge cloud as a function of the drift distance is determined. This information is used to calculate the spectrum detected from a fluorescence source, and it is at the basis of the model of the response function that will be developed in chapter 5.

4.1 Measurement of charge diffusion using tracks from minimum ionizing particles

The idea of this measurement is to exploit the spectral capability and the spatial resolution of a Timepix based silicon pixel detector and turn a beam of ionizing particles into a microscope to look at the charge transport phenomena taking place within the volume of a single pixel. It will be shown that the precision achieved with this technique is in the order of a few microns in the plane of the pixel matrix, and even less along the direction of the drift motion.

The advantage of this method is that the results are solely based on measurements. This avoids the a-priori introduction of physics parameters, such as diffusion and drift constants, that might bias the outcome of the analysis, as well as the need to know the electric field configuration in the sensor, which would require a complete description of its doping profile.

4.2 Experimental setup

The measurements have been performed with four Timepix chips bump-bonded to a single 300 μm thick p-on-n quad[1] silicon sensor biased at 100 V. The detector is exposed to a beam of 40 GeV negative pions at the H6-SPS experimental area at CERN.

A quad detector is chosen over a single device because of the larger sensitive area. In fact, the exploitation of the full 512 × 512 pixel matrix, for a total of approximately 2.8 × 2.8 cm^2, allows for the detection of long particle tracks at longitudinal incidence. This feature will have an influence on the quality of the final result, since the uncertainty on the parameters of the reconstructed trajectories, which propagates through the steps of the analysis, is in general lower when the particle tracks are longer.

Figure 4.1 shows the setup geometry. The sensor is positioned in the beam such that particles cross it longitudinally and the trajectories are in line with

---

[1] Medipix and Timepix chips can be tiled along the 3 free sides. As a consequence, 2×N arrays of an indefinite number of detectors, or 2×2 matrices, can be built with 100% sensitive area. These latter are referred to as quad modules. A quad detector is built by connecting the 2×2 matrix to a single sensor, in order to avoid any insensitive gap between the chips. Due to technical limitations in the wafer dicing process, a non-zero pixel-to-edge distance in the chips is always present. This causes the effective size of the pixels in the boundary between chips to increase. This feature causes a typical cross shaped artifact to appear in correspondence of the chip boundaries, especially visible in imaging applications, and an off-line correction is required.

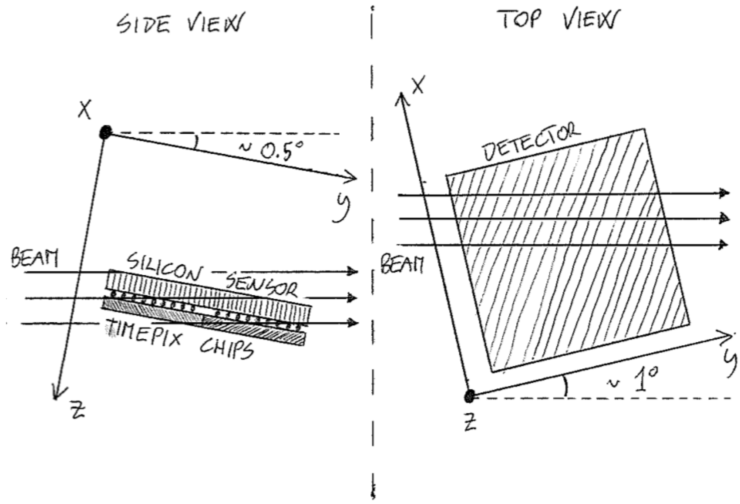

Figure 4.1: **Setup geometry: positioning of the detector in the beam. Also shown are the coordinate axes (x, y, z) defining the reference frame used in the analysis.**

the pixel rows. A small tilt (~0.5°) in the polar angle is applied in order for a minimum ionizing particle to leave a long straight track (200 pixels on average) that, at the same time, has a high probability to be contained within the detector area. The detector plane was tilted as well by ~1° to ensure that tracks would span over multiple pixel columns. Both conditions are fundamental in reaching sub-pixel resolution on the particle track hits.

The Timepix quad is operated in Time-over-Threshold mode (see section 2.4.1). This means that for each pixel traversed by a particle the value of the local energy release is given. A ToT-to-energy calibration has been performed after the beam test period using an Fe-55 source and X-ray fluorescence emission from pure metal targets irradiated by an X-ray tube.

4.3 Raw data analysis

The analysis described in the following is based on the assumption that minimum ionizing particles travel along a straight path while traversing the sensor. However, due to the different interaction mechanisms that a hadron can un-

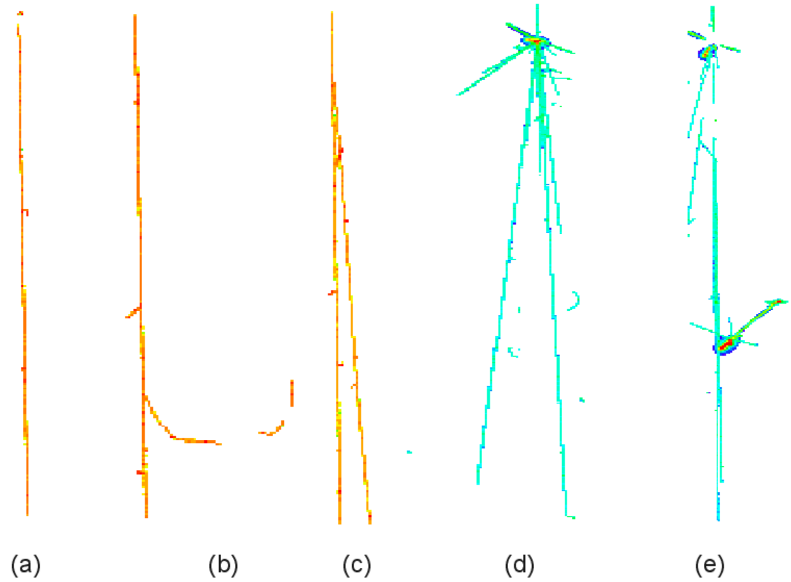

Figure 4.2: **Some examples of the typical track topologies: (a) a straight track from a minimum ionizing particle with few delta electrons, (b) a highly energetic delta emission, (c) production of a high energy secondary particle and (d)-(e) events with nuclear interactions.**

dergo with the sensor material, the set of possible track topologies observed in the data is much wider than just line segments.

4.3.1 Reference frame

The (x, y, z) reference frame was presented in figure 4.1. Pixel coordinates are recorded in the frame of the pixel matrix: from 0 to 511 in x and from 0 to 511 in y. The corresponding values in microns are obtained by multiplying by 55.

Apart from the small detector tilt, tracks develop along the y coordinate. The entrance point of the track in the sensor can be identified as the point with higher y value, while the exit point is the one with lower y value.

The z coordinate (in microns) identifies the depth in the sensor. The sensor backside corresponds to $z = 0$ μm, while the readout side corresponds to $z =$

300 μm.

4.3.2 Track selection and fitting

Tracks are identified in the raw frames as isolated clusters of pixels. In order to take into account dead pixels or pixels where the signal has fluctuated below the threshold, a gap of maximum three empty pixels is allowed.

Figure 4.2 shows a few examples of the most common track types. Each track is a cluster of particle hits where each dot represents a pixel with a non-zero digitized value. The color scale in the picture encodes the unnormalized signal amplitude, namely the Time-over-Threshold value of each pixel before calibration.

Two of the clusters in the figure (clusters (d) and (e)) present clear signatures of nuclear interactions. One of the goals of the track selection algorithm is to remove these type of events, whereas straight tracks left by minimum ionizing particles, such as (a), are kept and processed further.

The routine is not only designed to select straight tracks, but at the same time to remove hits associated with the emission of a delta electron. This condition ensures that the final fit is performed only on those hits that actually belong to the main trajectory, therefore maximizing the precision on the estimation of the track parameters.

After an overall correction of the quad cross artifact and a consequent recalculation of the energy in the involved pixels, the following criteria are applied:

1. **Removal of incomplete clusters.** A major requirement of the analysis is that the first and the last track hits can be identified as the entrance/exit points of the particle in/from the sensor. This is true only if the track is fully contained in the detector area. Clusters that contain pixels at the edge of the detector matrix are rejected.

2. **Removal of short and long clusters.** The cluster length L is calculated as the distance, in number of pixels, between the entrance point and the exit point. Clusters that do not fall within the [150-300] pixels length selection window are removed.

3. **Selection of minimum ionizing particle topologies.** For each track, the

$$\eta = \frac{\sqrt{A}}{L} \tag{4.1}$$

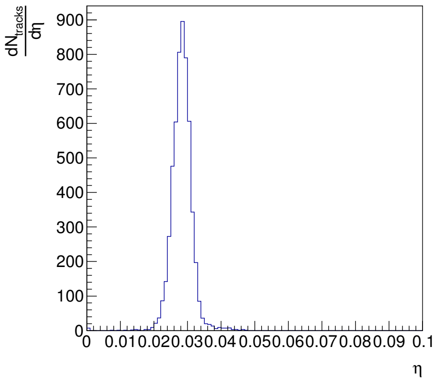

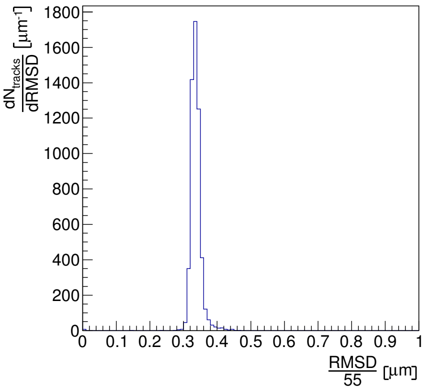

Figure 4.3: **Distribution of the η parameter (formula 4.1).**

Figure 4.4: **Distribution of the root mean square distance (RMSD) of the pixel hits to the fitted track.**

parameter is calculated. Here A is the area (in units of pixels) of the cluster, calculated as the number of pixels belonging to the cluster that have at least one neighboring hit along x. According to this definition, a fully straight track along y would have $A = 0$. More in general, high η values are indicative of the presence of nuclear interaction topologies, while more straight tracks, associated with minimum ionizing particles, assume η values close to zero. In order to select only these latter, clusters with $\eta > 0.05$ are rejected (see figure 4.3).

4. **Topological analysis.** This step, together with the following (the fitting), are illustrated in figure 4.5 for a single track. For each hit in the cluster, two scalar quantities are defined, called η_x and η_y. η_x is the length (in number of pixels) of the sub-cluster formed by all the hits with the same y- coordinate as the pixel being considered. In the same way, η_y is defined as the area of the corresponding sub-cluster along the y direction, with the difference that here a tolerance of up to five empty pixels between two non-empty ones is applied, to account for the possibility that, in the transition between two pixel columns, signals could be undetected because, due to charge sharing, they fall below threshold.

   η_x and η_y are used to identify hits associated to delta electrons, which are labeled as “bad hits”. In fact, if a hit has a too small η_y value ($\eta_y < 2$), i.e. it has few neighbors along y, it most likely belongs to a delta ray extending transversally with respect to the main track. Such a hit is labeled as a bad hit. Moreover, all the hits with the same x coordinate are labeled as bad because at this stage no track fitting has been performed yet, and therefore there is no information on whether a hit belongs to the particle track or to a delta electron cluster. After track fitting, these hits will be re-analyzed to finally assess their status (“bad” or “good”).

The typical track from a minimum ionizing particle is made by the connection of long single line segments along the y direction. In the connection points between segments, charge sharing effects are strong. In these zones, the width of the track is mostly two hits, corresponding to $\eta_x = 1$. Since this is the maximum extension observed along x for good tracks, hits with larger η_x are labeled as bad.

After these steps, it is possible that one or both of the two hits that were identified as first and last hits of the cluster are now labeled as bad hits, because they are part of a delta electron trail. In such a case, the first and last hits are redefined using the set of good hits and the cluster length is recalculated.

At this stage the track cluster in the example, deprived of all the bad hits, looks like the one in figure 4.5b.

5. **Track fit.** Minimum ionizing particles traverse the sensor along a straight path and the corresponding tracks can be fitted with a first degree polynomial in the plane of the pixel matrix. However, in order to properly estimate the original trajectory, the fit has to be performed only on those hits that actually belong to the particle path, while excluding the hits associated to delta electrons. For this purpose, the fit and the topological analysis are iterated according to the following procedure:

    (a) Following the topological analysis, a first fit is performed, in order to give a first estimation of the track parameters.

    (b) Hits farther than three pixels (165 μm) from the estimated track are labeled as bad hits, since they most likely belong to delta rays. A second fit is performed.

    (c) Hits farther than one pixels (55 μm) from the estimated track are labeled as bad hits. A third fit is performed.

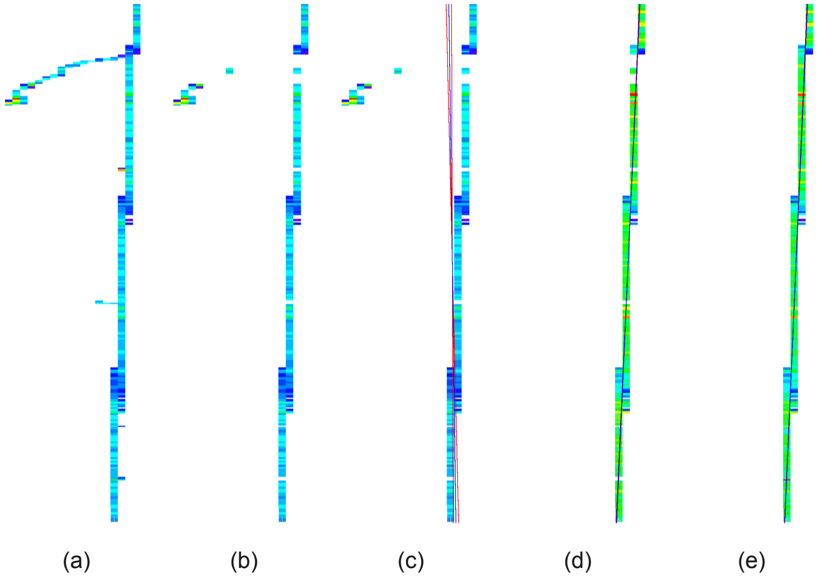

Figure 4.5: **An example of a minimum ionizing particle track going through the steps of the topological analysis and the fit.**

(d) At this stage some good hits are likely to have been labeled as bad hits from the previous cuts, due to the fact that at that point the track was not well estimated. Therefore each pixel is checked again for the η_x and η_y values together with the 1 pixel distance condition, and the good/bad hit label is reassigned. A final fit is performed.

To minimize the uncertainties on the line parameters, all fits are performed in a reference frame where the origin corresponds to the geometric center of the track. An example of these steps is shown in figure 4.5 from c to e.

6. **Track quality selection.** The root mean square distance (RMSD) of the track hits to the fitted line is calculated and tracks with RMSD $> 27.5\ \mu$m (0.5 pixels) are rejected (see figure 4.4).

For each track the two hits corresponding to the entry and exit points are not considered in the rest of the analysis. The reason is that since these pixels are not fully traversed by the particle, their energy value is intrinsically distorted.

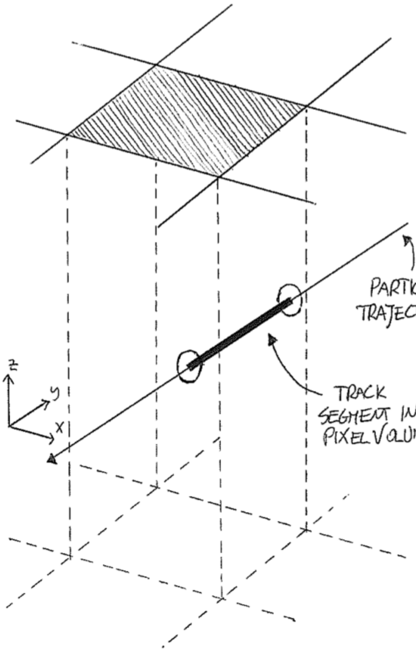

Figure 4.6: **Passage of a minimum ionizing particle in the pixel volume.**

4.4 Determination of track hit coordinates

The result of the selection and pre-processing is a collection of straight tracks where each pixel contains information about the energy released by the particle in its volume. This information can be correlated with the exact position where the particle passed, which can be calculated with a precision well below the pixel size, by using the fit parameters.

Figure 4.6 shows a drawing of a particle traversing a pixel volume. The x coordinate of the pixel hit is calculated as the (signed) distance of the fitted track from the center of the pixel. If the track is parametrized as $x = ay + b$, and if (x_i, y_i) are the coordinates of the pixel, then

$$x_i = \frac{ay_i - x_i + b}{\sqrt{1 + a^2}} \tag{4.2}$$

As figure 4.7 shows, the distribution of the uncertainty $\Delta x/x$, determined

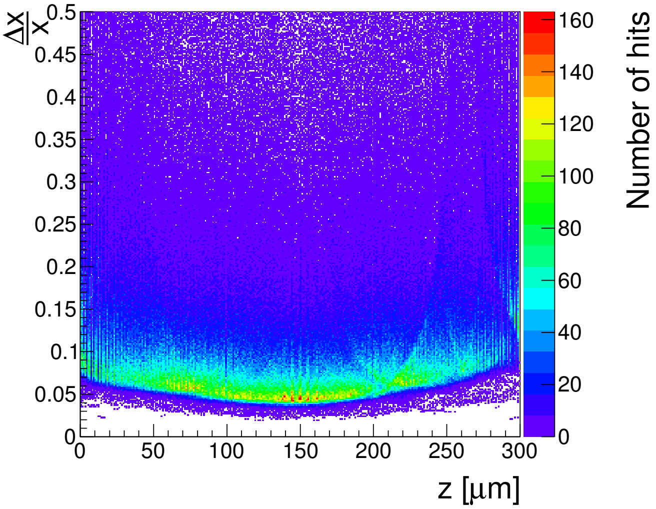

Figure 4.7: $\Delta x/x$ **distribution as a function of the depth in the sensor** z**.**

by propagating the errors, peaks below 5-10%.

The z coordinate is given by

$$z = t\frac{l}{L}, \tag{4.3}$$

where t is the sensor thickness (300 μm) and l is the distance of the current hit from the first track hit. For an average track length L = 200 pixels, this yields an uncertainty Δz below one micron[2].

---

[2] This result is obtained by propagating the error in formula 4.3, which yields

$$\Delta z = \frac{t}{L^2}\sqrt{L^2\Delta^2 l + l^2\Delta^2 L},$$

where $t = 300$ μm is assumed as a parameter. Both l and L are calculated as the distance between two pixels, the first and the last in the case of L. Given a pixel size of 55 μm, this means that $\Delta l = \Delta L = 55/\sqrt{6}$.

Δz is bound by the extreme values assumed when $l = 0$ and when $l = L$, which yield

$$\frac{55t}{\sqrt{6}L} < \Delta z < \frac{55t}{\sqrt{3}L}.$$

For an average track length of 200 pixels, i.e. $L = 200 \times 55$ μm, this results in 0.61 μm $< \Delta z <$ 0.87 μm.

Since the particle beam is almost parallel to the y axis, full translational symmetry is assumed within the pixel volume in this direction.

4.5 Analysis of lateral charge diffusion

After selection and fitting, the whole data set consists of 5522 tracks and a total of more than 1 million pixel hits, each identified by a coordinate vector (x, z) and an energy E given by the calibrated Time-over-Threshold value of the pixel.

Due to the sub-pixel precision with which the hit coordinates are known, these data can be used to study how charge is collected from the sensor to the readout, when generated at different depths and at different positions in the pixel area.

In order to avoid inter-chip mismatches, from now on the analysis is carried out separately for each chip of the quad. The results shown in the following refer to chip 0 (chip 0 and chip 3 were exposed to higher beam intensity). For this chip the data set consists of 3981 tracks and more than 500k good hits.

4.5.1 Charge sharing model

At this point, information on the diffusion of the charge carriers in the sensor can be extracted from the data by correlating the track hit positions in each pixel with the corresponding value of the measured energy, and exploiting charge sharing to retrieve information on the geometry of the process.

To do this, the data are fitted with a simple model of charge diffusion, which is sketched in figure 4.8. The sensor has thickness t and is segmented into square pixels of size p. A fast ionizing particle enters the pixel at position (x_0, z_0) and deposits energy along the y direction through the 55 μm path length, giving rise to an elongated cloud of charge carriers.

By treating transport of charge carriers as a combination of just drift and diffusion, the transverse (namely, along x) cloud profile is a Gaussian whose width $\sigma(z, z_0)$ is growing as a function of z. Notice that there is no need to consider diffusion along z, because this doesn't have an influence on charge sharing. Similarly, due to the translational symmetry in y, diffusion has no net effect in this direction, i.e. the density along y is constant at each moment during the drift.

If Q_0 is the total charge released by the particle in this pixel, the charge distribution at depth z is found by substituting the initial concentration $Q(x, y, z) =$

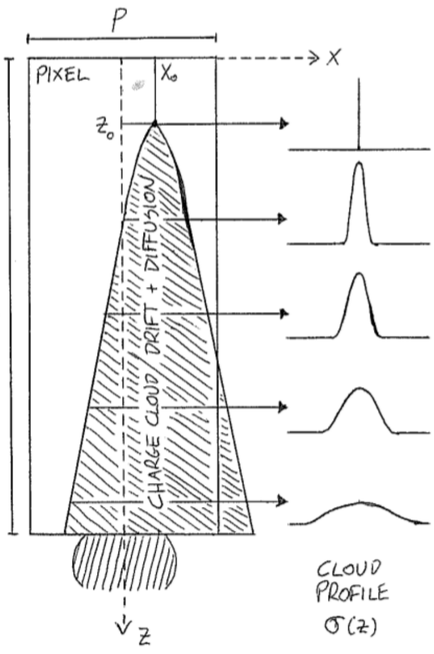

Figure 4.8: **Model of charge diffusion and charge sharing: the cloud is distributed according to a Gaussian profile in the x direction, whose width $\sigma(z)$ increases as the carriers drift towards the collection electrode (at the bottom). The model is fully symmetrical for translations along the y direction.**

$\frac{dQ_0}{dy}\delta(x'-x_0)\delta(z'-z_0)$ into equation 3.15, giving

$$\frac{dQ}{dx}(x,z;x_0,z_0) = \frac{Q_0}{\sqrt{2\pi}\sigma(z,z_0)}e^{-\frac{(x-x_0)^2}{2\sigma^2(z,z_0)}}. \tag{4.4}$$

Assuming that no charge is lost during the drift and that the electric field is uniform through all the sensor depth, the charge collected by the electrode is the integral of the charge density in the pixel area at depth $z = 300\ \mu$m, namely

$$Q(x_0,z_0) = \int_{-p/2}^{p/2} \frac{dQ}{dx}(x,300;x_0,z_0)dx. \tag{4.5}$$

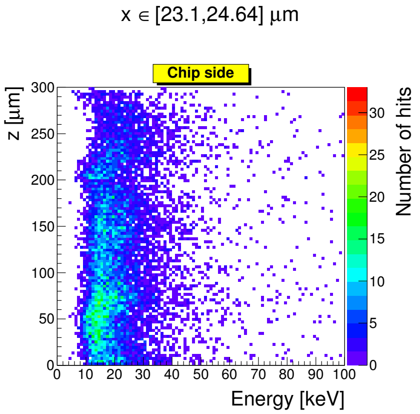

Figure 4.9: **Correlation between z and energy loss for tracks traversing the pixel at $x \sim 24$ μm.**

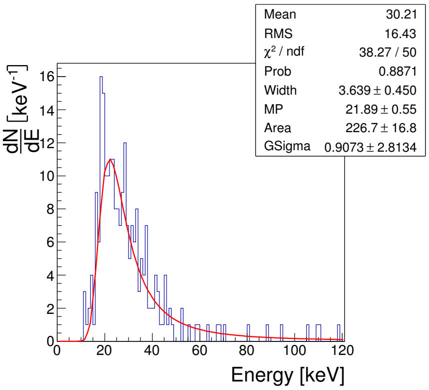

Figure 4.10: **Landau curve fitting the energy distribution of track hits at a specific (x_0, z_0) bin.**

If $\sigma(z, z_0) < p/2$ for all values of z and z_0, when $x_0 > 0$ (as in figure 4.8), the previous expression can be rewritten as

$$Q(x_0, z_0) \sim \frac{Q_0}{2} + \int_{x_0}^{p/2} \frac{dQ}{dx}(x, 300; x_0, z_0)dx, \tag{4.6}$$

which can be worked out to yield

$$Q(x_0, z_0) \sim \frac{Q_0}{2}\left[1 + \mathrm{Erf}\left(\frac{p/2 - x_0}{\sqrt{2}\sigma(300, z_0)}\right)\right]. \tag{4.7}$$

The analogue formula for $x_0 < 0$ is obtained by transforming $x_0 \rightarrow -x_0$. The assumptions used to derive this formula will be validated in paragraph 4.5.3.

Since the collected charge Q is proportional to the energy released by the particle, it fluctuates according to a Landau distribution and Q_0 has a natural interpretation as the corresponding most probable energy loss.

4.5.2 Determination of $\sigma(z_0)$

Formula 4.7 can be used to fit the data in a Q_0 vs x plot in order to retrieve the final charge profile width $\sigma(z_0) = \sigma(300, z_0)$. Such a plot can be made for

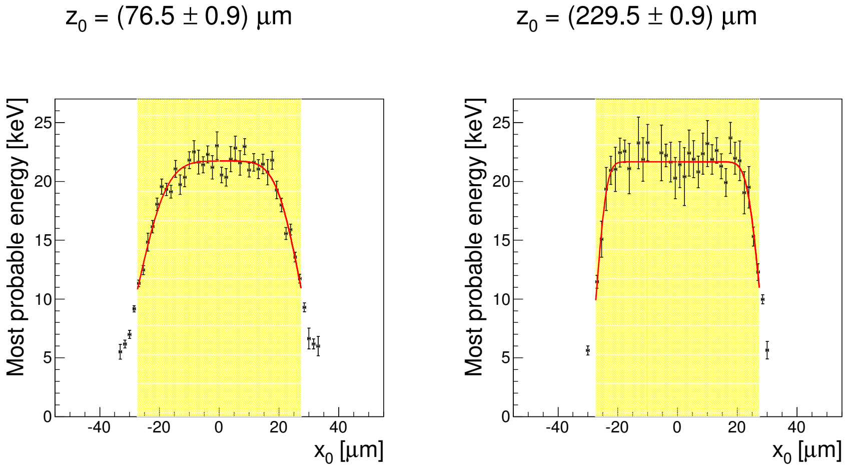

Figure 4.11: **Most probable energy, as obtained from the fit in figure 4.10, versus x_0, for two z_0 bins. The central band highlights the pixel volume.**

different values of the conversion depth z_0. The final result will thus show the dependence of $\sigma(z_0)$ on z_0.

For this purpose, the track hits were binned in 1 μm intervals in z_0 and 1.5 μm intervals in x_0. At each (x_0, z_0) bin a plot of the energy distribution is made as the histogram of the energy values of all the hits falling in this range. A plot of the correlation between z and energy for tracks traversing the pixel in the center ($x \sim 24$ μm) is shown in figure 4.9, while an example of the Landau energy distribution for a given (x_0, z_0) bin is shown in figure 4.10. Within the uncertainty, the average energy of each Landau distribution agrees with the value of 29.5 keV for the Bethe-Bloch energy loss expected for a 40 GeV pion traveling 55 μm (the pixel size) in silicon.

A Landau curve convoluted with a Gaussian profile, multiplied by an error function modeling the onset of the detector threshold at 4.50 keV, was fitted to each distribution and the most probable value for the energy loss was retrieved from the Landau component.

The dataset is now reduced to a 100×300 matrix of energy values (the most probable energy loss) at the corresponding positions in the (x_0, z_0) pixel plane. By plotting the most probable energy as a function of the x_0 coordinate at a given z_0 bin, one obtains graphs of type shown in figure 4.11 as an example.

The central band in the plot highlights the pixel volume, and helps forming a clear idea of the effect of charge sharing. In fact, while the energy values at the center of the pixel are distributed on a plateau at around 21-22 keV (which, again, corresponds to the expected most probable energy loss for 40 GeV pions in 55 μm of silicon, given a Landau distribution), these values decrease more and more as the particle trajectory moves towards the neighboring pixels, due to the fact that part of the charge is shared. Eventually, the energy drops to half the plateau value at the boundary between two pixels, and goes towards zero when $|x_0|> p/2$.

The solid line shows the fit to the data according to function 4.7, plus its counterpart for $x_0 < 0$. Two values of $\sigma(z_0)$ are extracted simultaneously by fitting the data in the left side and on the right side of the plot, and a mean value is computed by averaging the two.

Notice that the total charge Q_0 appearing in equation 4.7 can be determined before the fit, by separately fitting a constant value to the plateau region of the plot in figure 4.11. As a consequence, the only free parameter in equation 4.7 remains $\sigma(z_0)$.

These plots were made for each of the 300 z_0 bins, and the fit was repeated for each distribution. As a result, the full $\sigma(z_0)$ function could be determined, as shown in figure 4.12.

4.5.3 Validation of the model

The charge sharing model used to fit the data was derived from the assumptions that $\sigma(z, z_0) < p/2$ and that charge trapping during the drift is negligible. One possibility to validate these assumptions is to look at how the plateau values evolve as a function of z_0. This is illustrated in figure 4.13. Here the most probable value of the energy released at small distances from the pixel center ($x - x_0 < 10\mu$m), i.e. at the plateau region in the plots of the type shown in figure 4.11, is plotted against z_0. The plot shows that these values are constant throughout all the sensor depth, with the only exception of a shallow region close to $z_0 = 300$ μm, where anyway charge collection inefficiencies are expected due to the distortion of the electric field close to the pixelated electrode.

From these data it can be concluded that

(a) a charge cloud initiated in the center of the pixel is fully contained in the same pixel throughout the whole process of drift towards the electrode (i.e., $\sigma(z, z_0) < p/2$),

(b) the signal contribution is uniform through all the interaction depths.

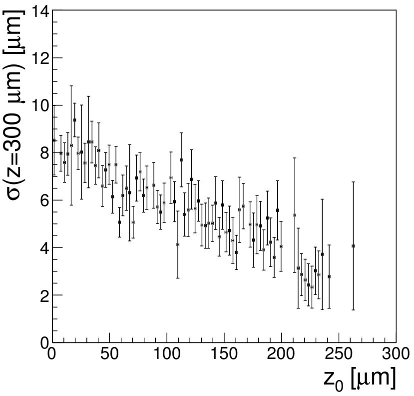

Figure 4.12: **Width of the Gaussian charge cloud profile in x as a function of the drift distance**[a]**.**

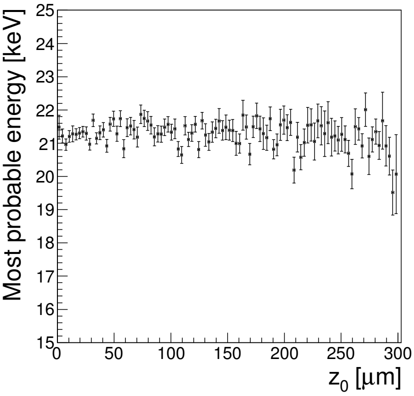

Figure 4.13: **Most probable value of the energy at small distances from the pixel center ($x - x_0 < 10\mu$m), as a function of z_0.**

---

[a] Notice that this plot shows the diffusion width as a function of the drift distance, and not of the time. The $\sqrt{t}$ dependence is thus not visible.

4.6 Generalization of the result

The $\sigma(z_0)$ function as determined from this analysis represents the lateral charge cloud spread at $z = 300$ μm (i.e. at the collection electrode), when a minimum ionizing particle traverses the sensor at a depth z_0.

Starting from the ansatz that this result is in fact generalizable, $\sigma(z_0)$ is also usable to define a function $\sigma(z)$ describing the development of the charge cloud created by any mechanism. At this point, z represents the distance in depth traveled by the charge carriers from the point of initiation of the charge cloud.

4.6.1 Parametrization of $\sigma(z)$

According to the theory of diffusion, the width of the carriers distribution increases as the square root of time. This feature is not visible in the results presented here, since diffusion is studied not as a function of drift time, but of

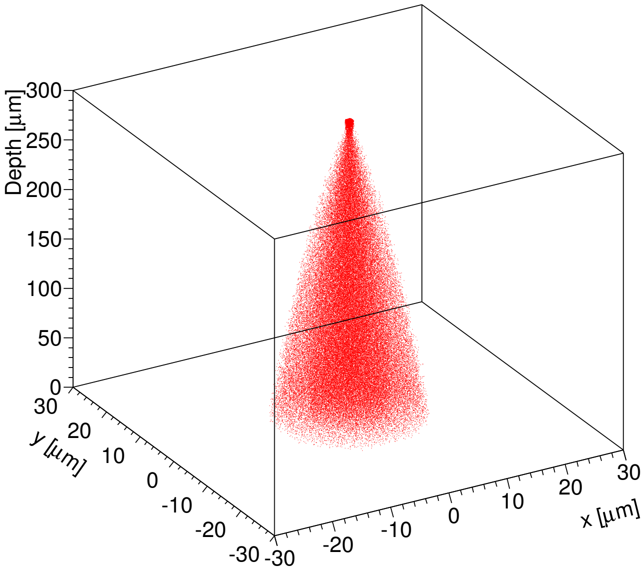

Figure 4.14: **Linear evolution of the diffusion profile.**

the drift distance. Translation into the time domain would require the knowledge of how the drift velocity varies during the process, which in turn requires the knowledge of the electric field, that can be calculated only if the doping profile of the sensor is known precisely.

However, for the scope of this thesis, what matters is just how the width of the distribution of carriers increases as a function of the drift distance, i.e. the plot in figure 4.12. This result shows that, within the experimental errors, the $\sigma(z)$ function can be parametrized by a first degree polynomial. Although this assumption is not physical, it turns out that a linear relation is already enough for obtaining good results when implementing $\sigma(z)$ in a numerical model to calculate the detector energy response. A more detailed study would not lead to a significant change in the results. This issue will be addressed in section 5.6, where a systematic study of the parametrization of $\sigma(z)$ will be undertaken. In the rest of the treatment $\sigma(z)$ will be parametrized with a linear relation.

Figure 4.14 provides an illustration of the full size of the diffusion profile while the carriers are drifting along z according to this parametrization.

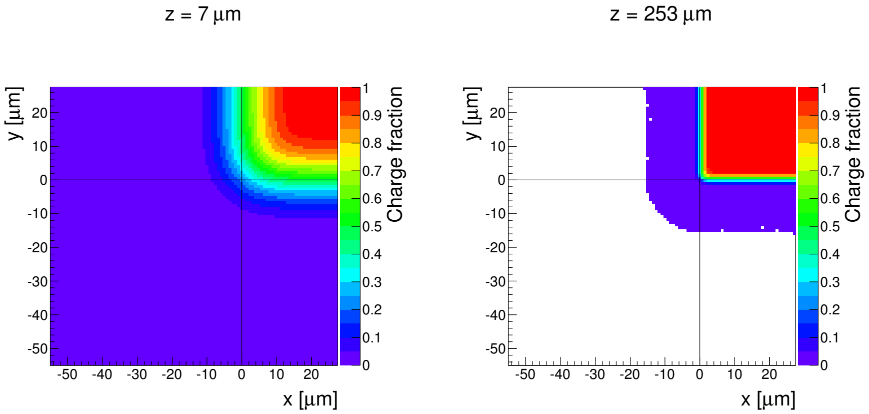

Figure 4.15: **Collected charge fraction for two different values of z computed by applying equation 4.9. The color scale represents the energy fraction seen by the pixel at the top right corner (by symmetry, only one quarter of it is represented).**

4.6.2 Calculation of the detector response to X-ray spectra

As a simple test, $\sigma(z, z_0)$ is implemented in a diffusion model that can be used to compute the energy spectrum detected from a molybdenum X-ray fluorescence source, which is then compared to a measured one.

Given a photon of energy E_0 converted at position (x_0, y_0, z_0) in the pixel volume, the energy (more precisely, the amount of charge) reaching $z_0 = 300\ \mu$m (i.e. the collection electrode) is distributed on the x, y plane according to a Gaussian profile

$$\frac{d^2E}{dxdy}(x, y; x_0, y_0, z_0) = \frac{E_0}{\sqrt{2\pi}\sigma(z, z_0)} e^{-\frac{(x-x_0)^2+(y-y_0^2)}{2\sigma^2(z,z_0)}}. \tag{4.8}$$

Here again only pure diffusion is considered. The energy detected by the pixel is given by the integral over the pixel area

$$E(x_0, y_0, z_0) = \int_{\text{Pixel area}} \frac{d^2E}{dxdy}(x, y; x_0, y_0, z_0)dxdy. \tag{4.9}$$

Figure 4.15 shows the detected energy fractions calculated with equation 4.9,

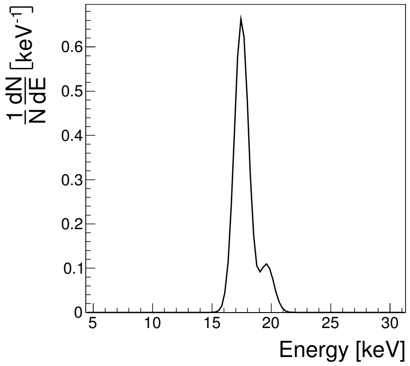

Figure 4.16: **Model of the molybdenum fluorescence source spectrum.**

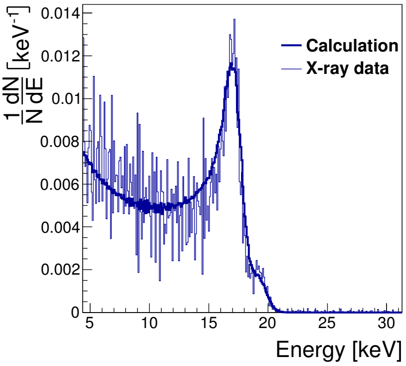

Figure 4.17: **Result of the X-ray test. The molybdenum fluorescence spectrum as calculated using $\sigma(z)$ (solid line) is well reproducing the spectrum measured by the Timepix detector.**

at two different z_0 values as an example. The same calculation is performed for any value of z_0, thus yielding a full 3D map of values.
The probability for a photon of energy E_0 to interact at a given depth z_0 in a sensor of thickness t is given in terms of the exponential attenuation law

$$P(z_0, E_0) = \frac{e^{-\mu(E_0)z_0}}{\int_0^t e^{-\mu(E_0)t'}dt'}, \tag{4.10}$$

where $\mu(E_0)$ is the energy dependent absorption coefficient for the sensor material. Combining 4.10 and 4.9, it is possible to calculate the effect of the detector energy response on the detection of a spectrum $S(E_0)$. More details on these formulas will be given in section 5.1.

4.6.3 Measurement and comparison with the model

The spectrum used for the test is taken from the X-ray fluorescence emission of a molybdenum target irradiated by the primary beam of a tungsten anode

X-ray tube. The same detector used for the test beam, at the same conditions of operation, was employed.

The cumulative spectrum was determined via a threshold scan, as described in section 3.3.3. By fitting the data with function 3.31 (see details in appendix D), the two components of the source spectrum $S(E_0)$, the K_α at 17.5 keV and the K_β at 19.6 keV, each with a width of 0.6 keV, can be retrieved, as shown in figure 4.16.

The energy response of the detector is calculated on $S(E_0)$ using equations 4.9 and 4.10, where the $\sigma(z)$ parametrization is derived by fitting a straight line to the data in figure 4.12.

In a first comparison, the calculated spectrum does not reproduce the data satisfactorily. What can be observed is that in order to adapt the model to the data the $\sigma(z)$ function has to be shifted, namely the offset of the linear parametrization has to be optimized. Indeed, it is reasonable to assume that the initial size of the charge cloud, which determines the offset of $\sigma(z)$, has to be adapted from case to case. The problem of determining the exact parametrization of $\sigma(z)$ as a function of the photon energy will be the topic of section 5.1.

For this measurement, the optimization of the $\sigma(z)$ offset was done by minimizing the root mean square distance (RMSD) between the data and the model. The final result, obtained by shifting $\sigma(z)$ by $\Delta\sigma = (0.49 \pm 0.21)$ μm, is shown in figure 4.17. Here the calculated spectrum is superimposed on the measured one, showing good agreement between the two.

Chapter 5

The energy response function: synchrotron data

To calculate the detected spectrum for any given input spectrum, the energy response function of the detector must be known. The response function at a given energy is the detector response to a monochromatic input at that energy. Experimentally, this can be measured by exposing the detector to mono-energetic radiation sources.

This chapter describes a measurement of the detector response function using synchrotron radiation, and how these data can be used to calculate the detected X-ray spectra.

5.1 Measurement of the energy response function using synchrotron radiation

In section 4.6 it was shown how to use the $\sigma(z)$ function measured from the CERN test beam data to calculate numerically the distortions undergone by an incoming X-ray spectrum during the detection process. In that example it was also stressed that, in order to reproduce the data, a recalibration of the $\sigma(z)$ parametrization was needed to adapt the results from the measurement with minimum ionizing particles to a model of X-ray photon detection.

The principle underlying the model of the energy response function developed in this chapter is based on a similar recipe: calculate numerically the detector effects on monochromatic radiation, using $\sigma(z)$ and formulas 4.9 and 4.10. The determination of the optimal values of the parameters employed to model $\sigma(z)$ can be done by fitting the calculation to direct measurements of the spectral response function at few energies, hence the idea of a synchrotron test beam. Values at other energies can then be computed by interpolation, and the response matrix formalism can be used to calculate the spectral distortion undergone by any incoming spectrum.

5.2 Experimental setup

This experiment is performed with the same detector type used for the CERN test beam, operated at the same conditions: a 300 μm p-on-n silicon sensor set at 100 V bias voltage. The readout is a single Timepix chip on a RelaxD [70] system.

The measurements have been conducted at the X-ray Absorption Spectroscopy (XAS) beam line of the Dutch-Belgian Beam Line (DUBBLE) at the European Synchrotron Radiation Facility (ESRF), Grenoble, France [47].

The white X-ray beam produced by a bending magnet is analyzed by a double-crystal Si(111) monochromator in order to have monochromatic radiation on the detector. The accurate measurement of the beam energy is performed by using a ionization chamber positioned before the detector.

The pitch of the second crystal and the gap between the crystal pair are adjusted for each energy to guide the beam into the ionization chambers. In addition, a vertically collimating mirror before the monochromator and a vertically focusing mirror after the monochromator, each with selectable silicon or platinum coatings, are used to align the beam and to suppress the higher harmonic content. The silicon mirror bare surface is used for experiments carried out in the 5-12.5 keV energy range, whereas the platinum coated mirror is used for the measurements in the 15-32.5 keV range.

The gas mixture in the first ionization chamber is changed as a function of the energy used in order to have approximately 10% absorption at each energy. This, together with the possibility to add different absorption filters (Al and C absorbers of different thicknesses [11]), ensures that the flux reaching the detector is optimized with respect to its expected performance, and does not exceed the value of 10^{11} cm^{-2}s^{-1}, after which pile-up effects become important.

5.3 Dataset

The photon energy is changed in steps of around 2.5 keV, covering the energy range between 5 keV and 32.5 keV. At each energy the beam spot is maximized in size by fine tuning the beam optics, in order to maximize the number of illuminated pixels. The typical spot size is a rectangle of approximately 10×0.5 mm^2 area, from which a large fraction of pixels are selected off line for the analysis.

Care is taken to keep the X-ray beam spot on the same detector area, thus ensuring that the data at different energies are collected by the same pixels.

The cumulative X-ray spectra are measured with the threshold scan method (see section 3.3.3). Multiple short scans (few minutes each) are performed for later integration, rather than a single long one. This minimizes intensity drift effects due to the beam current slowly decaying in time. In fact, beam refill takes place every four hours, with an intensity variation between refills of about 40%.

5.4 Analysis

Pixels exposed to the X-ray beam are selected for analysis by requiring a minimum number of photon counts at a given threshold. Among the selected pixels, only those whose neighbors are also in the selected region are retained. This ensures that each selected pixel does not have in its vicinity an inefficient (or dead) pixel that could distort the charge sharing contribution in the tail of the spectrum at low energies.

5.4.1 Reconstruction of the energy spectra and calibration

At a given photon energy, the different frames are integrated for each threshold and for each pixel in the beam spot the threshold scan is differentiated in energy in order to retrieve the raw spectrum.

An example of a pixel spectrum is shown in figure 5.1a. Such spectra show the typical features already introduced in section 3.3.2: a photopeak in correspondence of the nominal energy of the photon beam plus a continuous tail at lower energies arising from charge sharing effects. Notice that in this plot the horizontal scale is inverted. This is due to the positive polarization of the silicon sensor (hole collection), which causes the threshold units to assume low values for high energy thresholds, and vice versa.

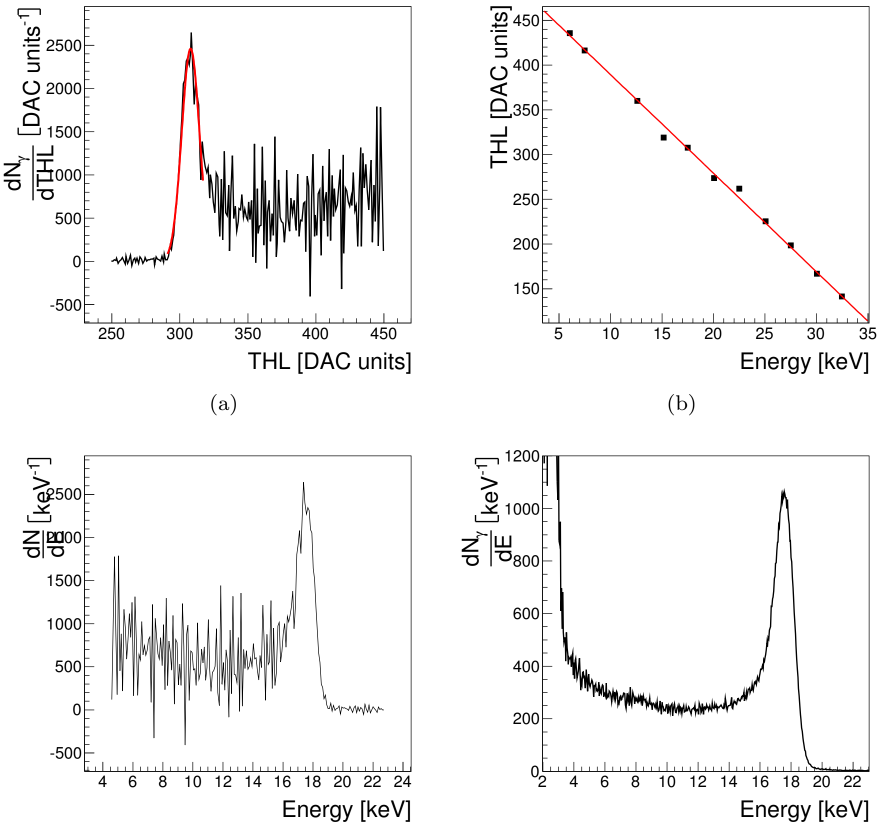

(a)

(b)

(c)

(d)

Figure 5.1: **(5.1a), the 17.504 keV spectrum of pixel (82, 57) obtained by differentiating the threshold scan, together with the Gaussian fit at the peak position; (5.1b), the calibration plot for the same pixel; (5.1c), the calibrated spectrum; (5.1d), the total spectrum at 17.504 keV, namely the sum of the calibrated spectra of all pixels selected from the beam spot at this energy.**

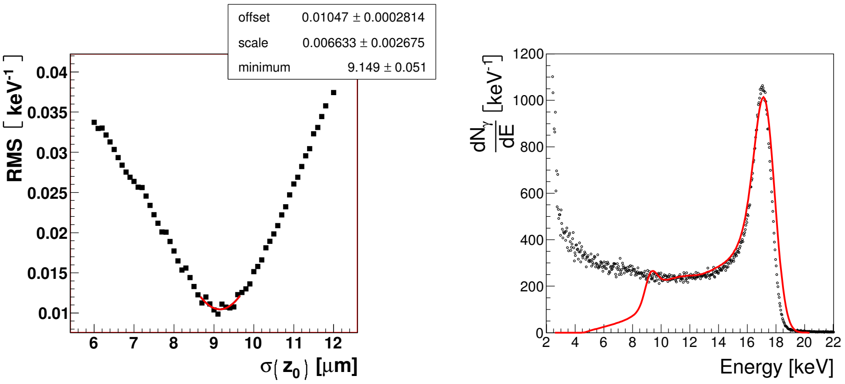

Figure 5.2: **On the left, the determination of $\sigma(z_0)$ at 17.504 keV, via a parabolic fit in the minimum of the RMS curve; on the right, the calculated spectrum (continuous line) at this energy compared to the corresponding measurement (dots).**

The pixel spectra at different energies are first used for calibration of the energy scale. For this purpose, a Gaussian function is fitted to the photopeaks in order to retrieve its position (an example in figure 5.1a). The photopeak positions are plotted as a function of the corresponding nominal energy of the beam, and a straight line is fitted through the points (figure 5.1b). The line parameters are used to calibrate the energy scale of the spectra pixel by pixel (figure 5.1c).

After calibration, a total spectrum is obtained by summing the aligned spectra of all the pixels contained in the beam spot (figure 5.1d).

5.4.2 Fit of the diffusion model to the data

Being measured from monochromatic radiation, each spectrum is a direct representation of the unnormalized detector response at the corresponding energy. For this reason, these data can be used for comparison with the energy response model introduced in section 4.6. This comparison ultimately provides the optimal parametrization of the model, which leads to two results:

1. the possibility to determine the absolute scale of the measured synchrotron spectra at different energies,

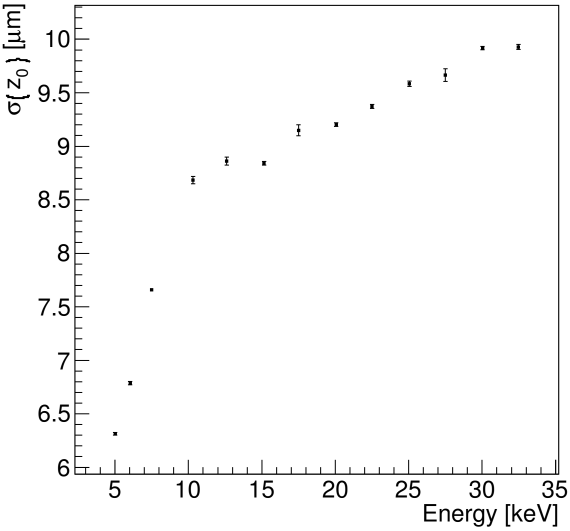

Figure 5.3: **The values of $\sigma(z_0)$ for all the measured energies.**

2. the possibility to compute analytically the spectral response function at any energy in the range of the measurement or, by extrapolation, outside it.

The energy response model starts from the diffusion profile defined in formula 4.8, that is rewritten here for convenience:

$$\frac{d^2E}{dxdy}(x,y;x_0,y_0,z_0)=\frac{E_0}{\sqrt{2\pi}\sigma(z,z_0)}e^{-\frac{(x-x_0)^2+(y-y_0^2)}{2\sigma^2(z,z_0)}}. \tag{5.1}$$

Following the discussion in section 4.6.1, $\sigma(z)$ is parametrized as a first degree polynomial

$$\sigma(z,z_0)=\sigma(z_0)+Az \tag{5.2}$$

The charge that reaches the collection electrode for a given pixel is the integral in the pixel area of the charge distribution at $z=t$, where t is the sensor thickness. In terms of the detected energy fraction $f=E/E_0$, this quantity takes the form

$$f(x_0, y_0, z_0) = \frac{1}{\sqrt{2\pi}\sigma(z, z_0)} \int_{\text{Pixel area}} e^{-\frac{(x-x_0)^2+(y-y_0^2)}{2\sigma^2(z,z_0)}} dxdy. \tag{5.3}$$

Thanks to the Timepix Time-over-Threshold logic, $f(x_0, y_0, z_0)$ represents the actual energy fraction that is measured by the pixel.

For $z = 0$, $\sigma(z_0)$ represents the initial spread of the charge cloud which, in a model of X-ray detection, is affected by the transverse range of the photoelectron. In particular, one expects that $\sigma(z_0)$ is an increasing function of the photon energy, since the higher the energy of the X-ray photon, the higher the energy of the photoelectron, which therefore has a longer range in the sensor. This information can be extracted from the synchrotron data by using formula 5.3 to calculate the expected spectra, that can then be compared to the reconstructed spectra, and the values of $\sigma(z_0)$ can be determined for each of the experimental energies.

For this purpose, the total synchrotron spectra at each energy E_0 are fitted with a Gaussian function in the region around the photopeak. The width of the distribution is used to produce a Gaussian spectrum $S_0(E; E_0)$ that mimics the synchrotron source at energy E_0 convoluted with the detector spectral resolution. The latter has shown no particular dependence as a function of E_0. In fact, an average value of 0.698 keV for the Gaussian width has been adopted for all E_0 values.

By applying 5.3 and using the energy dependent X-ray attenuation coefficient $\mu(E)$ in silicon, the expected synchrotron spectrum, i.e. the energy response function R at energy E_0, is calculated as

$$R(E; E_0) = \frac{1}{V} \int_0^t dz_0 S_0(E; E_0) \left[1 - e^{-\mu(E) z_0}\right] \iint_A dx_0 dy_0 f(x_0, y_0, z_0). \tag{5.4}$$

In this formula A is the area in the x, y plane in which the surface integral is calculated, and V is the corresponding volume extending through the full depth of the sensor. A doesn't simply comprise the pixel where the signal is being read out, but also the neighboring ones. This accounts for the contribution to the pixel signal from the charge cloud leaking into the neighboring pixels.

The spectrum $R(E; E_0)$ calculated with 5.4 is compared to the corresponding one measured at energy E_0. The value of $\sigma(z_0)$ that best fits the data is determined by minimizing the root mean square distance (RMS) between the two spectra[1]. The minimization is restricted to the energy range from $E_0/2$ onwards. In fact, at lower energies the spectrum contains contributions from the charge leaking from the neighboring pixels and can thus be distorted if the efficiency of the pixels is different.

An example of the procedure is shown in figure 5.2 for the 17.504 keV peak. On the left, the determination of $\sigma(z_0)$ via a parabolic fit in the minimum of the RMS curve is shown; on the right, the calculated spectrum at this energy is compared to the corresponding one from the measurement, showing the good agreement between the two.

A plot of the $\sigma(z_0)$ values for all the energies measured in the experiment is provided in figure 5.3. This latter shows a “knee” at around 10 keV, the origin of which is still not understood.

5.4.3 Calculation of the energy response function

Using the result in figure 5.3, the value of $\sigma(z_0)$ for each energy in the measurement range can be determined by interpolation. Two straight lines are separately fitted to the regions before and after 10 keV, where the “knee” of the data is present, and the line parameters are used to calculate $\sigma(z_0)$ at any energy. This also allows for extrapolation at energies beyond the experimental points.

Using this information, the energy response function can be calculated at each energy E_0 using formula 5.4 acting on a Gaussian X-ray spectrum $S_0(E; E_0)$ with a width of 0.698 keV (see paragraph 5.4.2).

Formula 5.4 can be applied on restricted areas A of the detector surface[2], in order to calculate the energy response function separately for a generic pixel and for the pixels in its neighborhood. This choice has an advantage in imaging applications, as illustrated in figure 5.4. Depending on the X-ray path inside the sample, the source spectrum is attenuated by different materials, distributed with different geometries. Thus, in general, each pixel sees a different transmitted spectrum, and as a consequence it contributes in a different amount to the signal detected in its neighbors.

---

[1] Given two generic spectra $S_1(E)$ and $S_2(E)$, the RMS distance is here defined as

$$RMS = \sqrt{\frac{\int_{\frac{E_0}{2}}^{E_{max}} \left[S_1(E) - S_2(E)\right]^2 dE}{E_{max} - \frac{E_0}{2}}}$$

[2] And, accordingly, on restricted volumes V.

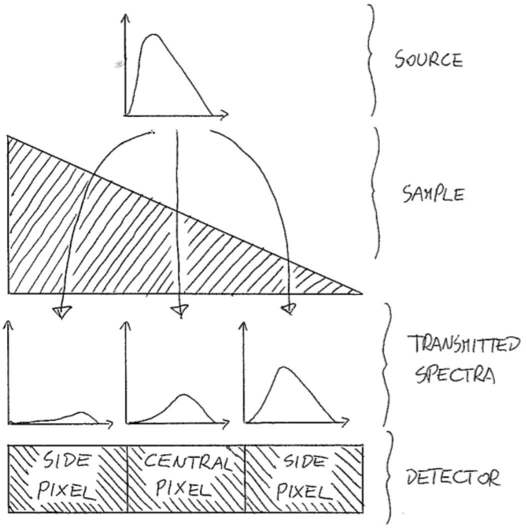

Figure 5.4: **Different spectra reach different pixels due to the sample inhomogeneities.**

A separate calculation of the components of the energy response function is illustrated in figure 5.5, where the comparison of the model to the 17.5 keV synchrotron data is shown. The calculation is performed separately for the central pixel and its 8 neighbors (4 at the sides and 4 at the corners).

Figure 5.6 shows a one dimensional representation of the total response function calculated in the energy range from 2 keV to 50 keV at discrete values of the photon energy.

5.5 Verification of the result

To verify the model, the energy response function is used to calculate the spectrum from an X-ray tube source, which is then compared to a measured one.

The 300 μm p-on-n silicon sensor type, biased at 100 V and read out by a Timepix chip, is exposed to a W-anode X-ray tube operated at 50 kV. A threshold scan is performed and the cumulative source spectrum is retrieved.

Each pixel is calibrated individually using X-ray fluorescence emission from different metal targets exposed to the source beam. The calibration ranges from

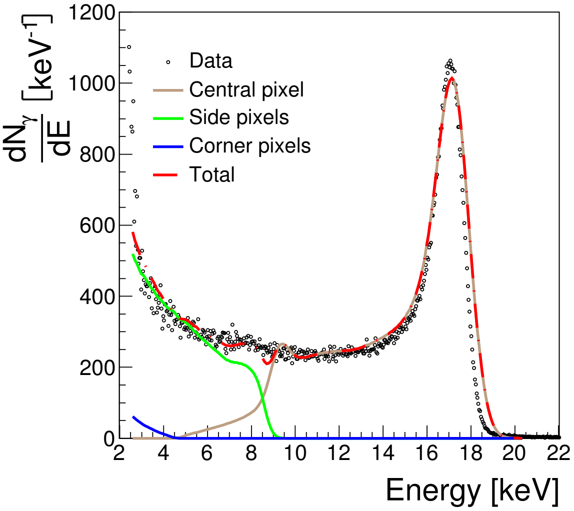

Figure 5.5: **Calculation of the energy response function at 17.5 keV.**

9.89 keV (K_α emission from germanium) to 25.27 keV (K_α emission from tin).

The same spectrum is then measured using a silicon drift detector (Amptek model XR-100SDD), whose energy scale is calibrated using the characteristic peaks of the sealed tube X-ray source spectrum and the K-edge positions in the spectrum transmitted by different metal foils placed between the source and the detector.

The spectrum measured with the silicon drift detector is used to retrieve the true source spectrum $I^0(E)$ by deconvolving the energy dependent absorption in the 500 μm silicon sensor. From this, the distorted Timepix spectrum $I(E)$ is determined as

$$I(E) = \int_0^\infty R(E;E')I^0(E')dE', \tag{5.5}$$

The result is shown in figure 5.7, where the calculated spectrum is superimposed onto the single-pixel spectrum from the Timepix measurement, determined by differentiating the raw threshold scan. The agreement between the two spectra is good for energies above $\sim$ 8 keV, while the mismatch at lower energies might well be due to the extrapolation of the energy scale outside the calibration range.

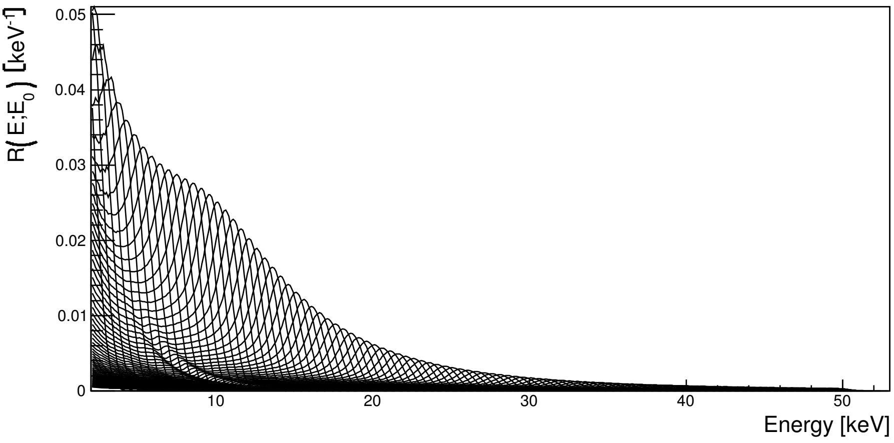

Figure 5.6: **The energy response function $R(E;E_0)$ of a 300 μm thick silicon sensor read out by a Medipix or Timepix chip, for discrete values of E_0 in the range from 2 keV to 50 keV.**

In this case, where each pixel receives the same spectrum, the energy response function $R(E;E')$ used in formula 5.5 can be calculated through formula 5.4 with A being the area of the pixel and its neighbors. In the most general case, where a different spectrum is seen by each pixel, the detected spectrum is determined as the superposition of all the contributions from the neighbors to the main spectrum from the central pixel. Each contribution can be determined by applying formula 5.5 using $R(E;E')$ calculated under the corresponding conditions. This approach will be used in chapter 6, where the energy response function is implemented in a spectral CT reconstruction algorithm.

5.6 Systematic uncertainties on the parametrization of $\sigma(z)$

The energy response function shown in figure 5.6, that is used to obtain the result in figure 5.7, is calculated assuming a linear parametrization of $\sigma(z)$. As already anticipated in section 4.6.1, this assumption is not derived from physical principles, but it turns out to be suitable when $\sigma(z)$ is used to reproduce the

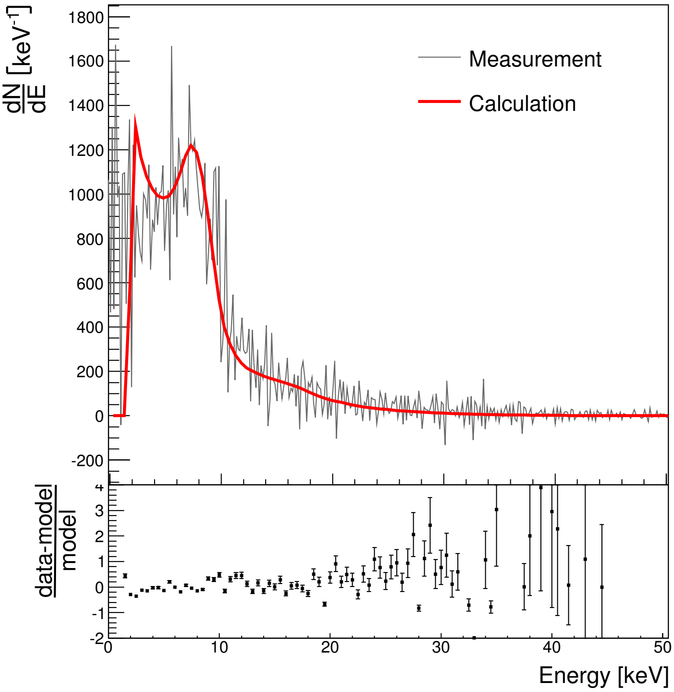

Figure 5.7: **The calculated open beam spectrum superimposed to the measured one.**

results presented in this chapter.

The experimental determination of $\sigma(z)$ from the CERN test beam, presented in figure 4.12, shows a fundamental lack of data in the region $z > 250$ μm. This region will therefore contribute to the systematic uncertainty on the energy response function calculated using $\sigma(z)$ via formula 5.4. In order to establish the magnitude of this effect, the following study has been carried out.

As a first step, the energy response function is re-calculated by truncating the linear parametrization of $\sigma(z)$ at $z = 250$ μm. This extreme situation is studied to determine to what extent the final results can be influenced by this region of the plot. The outcome of this experiment is shown in figure 5.8a, where a clear deviation of the newly calculated spectrum (in blue in the plot)

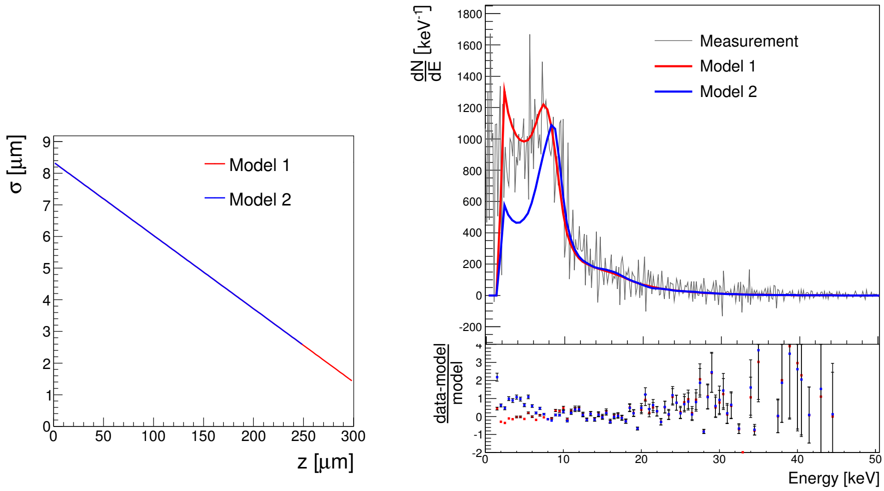

(a) **Model 2: $\sigma(z)$ truncated at $z = 250$ μm.**

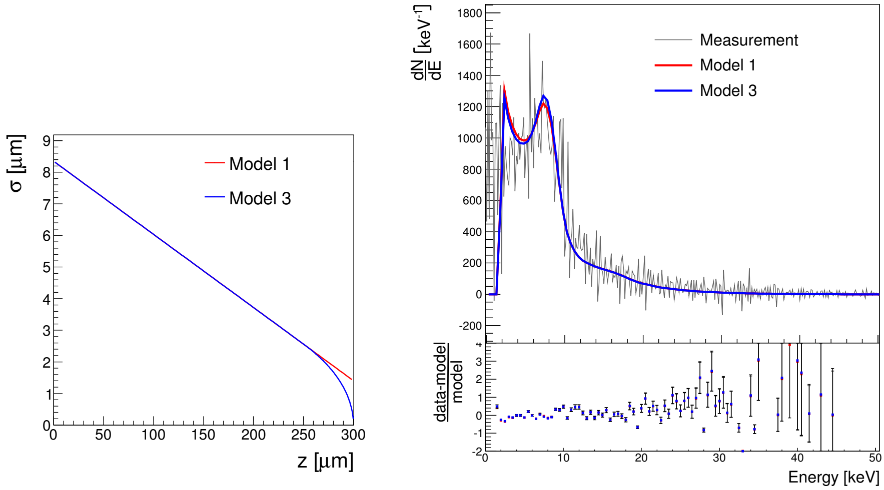

(b) **Model 3: $\sigma(z)$ ending with a $\sqrt{\log}$ function from $z = 250$ μm to $z = 300$ μm.**

Figure 5.8: **Study of the systematic effects of the $\sigma(z)$ parametrization. Model 1 in the legends refers to the full linear parametrization.**

from the data appears at low energies.

Next, the shape of $\sigma(z)$ for z between 250 μm and 300 μm is parametrized as a $\sqrt{\log}$ function according to the model described in appendix E, where the ideal pn junction electric field is considered. The parameters of the $\sqrt{\log}$ function are chosen by requiring that the value of the function and of its first derivative at $z = 250$ μm coincide with the corresponding values from the linear parametrization at $z < 250$ μm.

The spectrum calculated using the new energy response function is shown in figure 5.8b in blue, superimposed to the one calculated using the full linear model of $\sigma(z)$, in red. The two results show a slight difference in the low energy region (E $< \sim$ 8 keV), where the new model fits the data with a χ^2 5 % better than in the other case. In the rest of the energy spectrum, no improvement with respect to the full linear model is observed, meaning that the linear model can be used to parametrize $\sigma(z)$ with sufficient accuracy, and leads to the correct calculation of the energy response function for energies above $\sim$ 8 keV.

5.7 Possible extensions of the model

The numerical model employed to calculate the energy response function is based on a simple geometrical treatment of the diffusion and charge sharing effects. A more accurate description should take into account other effects, among which scattering and fluorescence.

5.7.1 Scattering

Radiation reaching a given pixel might not belong to the X-ray line path originating from the source, but might originate from scattering centers in the measurement setup, in the detector itself or, in case of X-ray imaging, in the sample. The effect of scattered radiation on the detected spectra is to add a continuum component, the shape of which strongly depends on the nature of the scattered radiation.

This situation is not taken into account in the simple model of the energy response function defined in this chapter. However, all the results reported in this thesis are obtained using low energy X-rays, for which the Compton cross section is always negligible by orders of magnitude with respect to the photoelectric cross section. Inclusion of scattering effects will become important when high energy X-rays will be considered or when high-Z sensor materials will be used as detectors.

5.7.2 Fluorescence escape peaks

The effect of fluorescence in the sensor gives rise to escape peaks in the detected spectrum. These appear when part of the energy released by the X-ray photon is not converted into charge, but escapes the sensor through the emission of fluorescence radiation when a vacancy is created in an inner atomic shell.

Since the energy E_i of a fluorescence photon is fixed, the effect on the spectrum is the appearance of peaks at energies $E_0 - E_i$ alongside the main peak at E_0. In silicon the distance of the escape peaks from the photopeak is 1.74 keV for the K_α and 1.83 keV for the K_β.

The intensity of the escape peaks relative to the photopeaks depends on the fluorescence yield of the material, and is therefore higher for high-Z sensors, such as germanium, GaAs and CdTe, where usually the effect cannot be neglected. In silicon, typical values are in the order of few percent at energies around 5 keV, slightly increasing for higher energies (see, for example [67]). Such small values confirm that, at least on first approximation, these contributions can be neglected.

5.8 Summary

The work described in this chapter and the previous one explains how the energy response function of the detector used throughout the rest of the thesis has been determined. To achieve this goal, two measurements at test beam facilities have been carried out, one at CERN with relativistic charged particles and one at ESRF with synchrotron radiation.

From the first measurement, the evolution of the diffusion profile in the silicon sensor has been determined precisely by exploiting the high granularity and the spectral capability of the Timepix readout chip. The results show that the cloud of charge carriers evolves linearly as a function of the drift distance from the initiation point. It has been shown that this information can be used to explain the shape of the spectra measured when the detector is exposed to fluorescence X-ray emission from pure metal targets. In particular the characteristic charge sharing tail can be well reproduced by the model.

The diffusion and charge sharing model has then be used to calculate the energy response function, i.e. the detector response to monochromatic radiation at different energies. To determine the parameters of the model, the calculation has been fitted to the data from the synchrotron measurements. A study on the systematic uncertainties on the parameters has shown that the energy response function thus calculated is well suited to reproduce the detector effects that cause the distortion of X-ray spectra from vacuum tubes. This result is of primary importance for the work that will be presented in the next chapter, since it will be a crucial feature of the spectral CT reconstruction methods that will be there developed.

5.9 Outlook

The results so far presented could be improved in future work. One of the main issues to be addressed regards the stability of the detector. Extensive studies are needed to determine whether the operational parameters of the detector (e.g. the threshold) are stable in time or, if they change, what the magnitude of the effect is, what its causes are and how it can be limited and/or controlled. Time variation of the detector performance might have a significant influence on the validity of the calibration after its establishment, as well as the validity of the energy response function. How can these effects be measured, controlled and compensated?

More work is also needed to understand why the energy response function cannot yet properly describe the data for energies below ~ 8 keV. Is this a miscalibration effect, or is the model too simple? How does the inclusion of other effects, such as scattering and fluorescence, affect the results? Such a study would probably require the use of an accurate simulation framework that could account for all possible physical effects that might give a significant contribution. Such a work would be especially required as soon as high-Z sensor materials rather than silicon will be employed. In this case, the contribution of high energy photons to the detected spectra will be significant, and scattering as well as fluorescence effects will not be negligible anymore.

Finally, for other detector types the energy response function has to be determined. A systematic study of how the energy response function changes as a function of, for example, the pixel size, the sensor material or the readout mode[3], would be of great interest.

---

[3] For example, how does the response function look like for Medipix3 operated in charge summing mode?

Chapter 6

Spectral CT

The different image reconstruction techniques presented in the first chapter were all based on the assumption that the X-ray source is monochromatic and, as a consequence, the derived algorithms only provided an approximate solution to the problem of tomographic reconstruction.

In this chapter, spectral computed tomography is introduced, aiming at the inclusion, in both the detection and the reconstruction steps, of the full information on the polychromatic X-ray tube spectrum and of how this is modified when the beam is transmitted through the imaged sample and then detected.

In this chapter, the detector spectral response determined from the results of chapter 5 is used to implement this information in a reconstruction algorithm that can be applied on data from a silicon detector read out by a Medipix chip.

The results are color three dimensional X-ray images of the sample, in which different materials are represented by different colors.

6.1 Material resolution and color X-ray imaging

Spectral tomography is also referred to as “material resolving” or “color” tomography. The meaning of this can be explained with the aid of figure 6.1, showing the energy dependence of the attenuation coefficient for different elements in the X-ray range. This means that distortions undergone by the source spectrum while traversing the sample carry information about the material content of the object. The fundamental idea of spectral X-ray imaging in general, and spectral CT in particular, is that by exploiting the energy information encoded

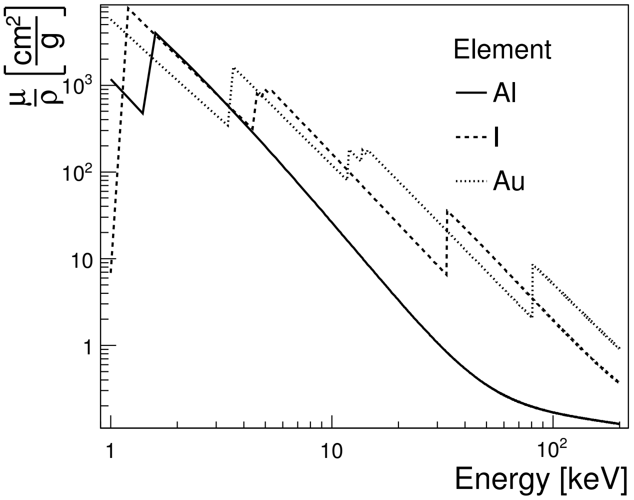

Figure 6.1: **Mass attenuation coefficient for different elements.**

in the data from spectroscopic X-ray detectors, one is able to measure energy dependent features in the image that can be correlated with the presence of a specific element or, more in general, material in the sample.

Once different materials have been recognized and located, different colors can be assigned to each of them, thus leading to color X-ray imaging. The meaning of colors usually employed in conventional rendering of computed tomography reconstructions is fake in the sense that colors do not identify different materials, but they represent an alternative scale to visualize scalar X-ray values.

6.2 Material assignment in CT number space

Contrast in different materials can be achieved by looking at the characteristic dependence of the associated signal at different detector thresholds. This principle is illustrated in figure 6.2, where a calculation is carried out for the case of a Medipix based silicon detector exposed to the beam from an X-ray tube source. This plot shows how the number of photons (in units of $-\log\left(N_\gamma/N_\gamma^0\right)$, where N_γ^0 is the signal from the open beam spectrum) detected at different thresholds, changes for different materials, in this case pure elements. For this calculation,

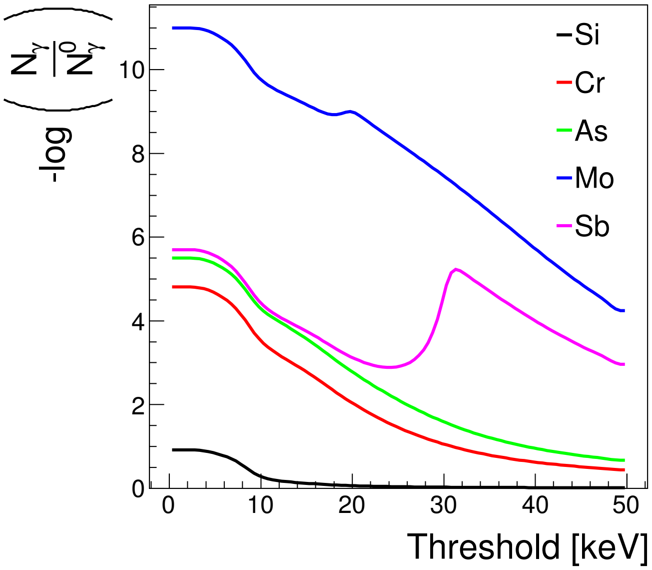

Figure 6.2: **Medipix signal expected from different elements as a function of the threshold position.**

elements are considered at the nominal density, and the thickness is 55 μm for all of them[1]. This situation thus reproduces the case of the 2D images of 55 μm thin foils of different materials.

Each element shows a very characteristic curve. By setting the detector at a specific threshold, in most of the cases every element yields a different value of the signal, thus giving the possibility to identify it. This capability depends on two parameters. First, the statistics of the data, that determines the fluctuations of the signal. Second, the resolution of the threshold, that determines the fluctuations in the energy scale.

To enhance the material separation power, images at different threshold can be compared. This operation can be aided by the presence, especially in high-Z elements, of strong deviations from monotonicity caused by the presence of K-edges in the photoelectric cross section. In figure 6.2, this is visible especially for

---

[1] This thickness corresponds to the voxel size that will be assigned to the reconstructed images later on, matching the size of the detector pixel.

Mo and Sb. Results on material recognition in two-dimensional X-ray imaging using spectroscopic detectors can be found, for example in [65].

The situation presented in this example is, however, very simplified. When different thicknesses and/or densities are involved, the curves in figure 6.2 can get close to each other, to such an extent that the different materials cannot be distinguished. This is particularly true for elements with similar Z, for which the shape of the curve is similar. Furthermore, this example does not account for situations in which different materials overlap. This gives rise to an infinite amount of possible combinations and the corresponding expected signals, which can be very complex to control.

All these issues are resolved in 3D imaging. In computed tomography the sample is reconstructed in a volume of voxels of well defined size. This means that the signal (i.e. the CT value) assigned to a specific voxel corresponds to the signal of a specific material thickness t, the one corresponding to the voxel linear size. Save for variations in density, the CT numbers in the reconstruction represent signals from materials all at the same thickness. Moreover, if the voxel size is sufficiently small, each voxel will possibly contain only one material. These features drastically reduce the signal degeneracy problem of 2D imaging, which can be finally eliminated by including spectral information, e.g. by taking images at multiple thresholds. This makes it possible to correlate the CT numbers with different materials and realize color, i.e. material resolved, computed tomography.

6.2.1 A color CT example

A simple object is prepared for a proof of principle of material resolved X-ray computed tomography with Medipix based detectors. The sample, shown in figure 6.3, consists of a 5 mm plastic rod around which a 100 μm thick cadmium foil and a 40 μm thick copper foil are wrapped.

Dataset

The object is imaged using a micro-focus X-ray tube operated at 70 kV - 10 μA and a quad detector read out by four Timepix chips operated in Medipix mode. The full CT scan is repeated at three different thresholds of the Timepix chip: 4, 17 and 28 keV. These values are chosen in order to enhance the material contrast in the data. In fact, the k-edge positions of copper and cadmium are at 8.98 keV and 26.71 keV respectively, so laying between the chosen threshold

Figure 6.3: **Picture of the sample used for the color CT proof of principle. Copper and cadmium foils are wrapped around a plastic rod.**

values. Figures 6.4, 6.5 and 6.6 show a raw projection at the three threshold values, making visible the change in relative contrast of the three materials.

For this experiment, each scan consists of just 20 projections between 0° and 180°, each corresponding to an exposure time of 10 s. The projections are pre-processed with the signal-to-thickness calibration technique described in appendix A, in order to equalize the detector response and to minimize beam hardening effects, and the quad cross artifact is corrected.

Reconstruction

For each dataset at each threshold, a full tomographic reconstruction is performed using the OSEM algorithm described in section 1.5.1 applied on the signal-to-thickness corrected projections.

The correlation plot for the CT values at each threshold (figure 6.7) shows that the three materials create separate “clouds” in this space. By defining boundary hyperplanes in the plot, voxels can be assigned different colors according to which sub-space they belong to in the CT numbers space.

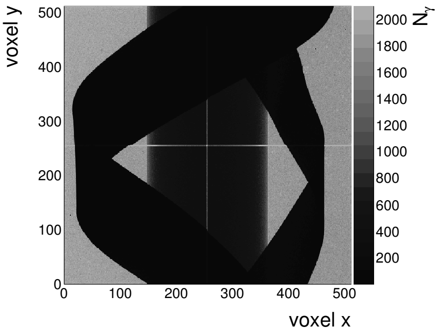

Figure 6.4: **Raw image at 4 keV threshold**

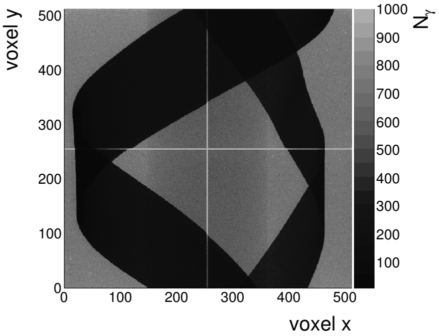

Figure 6.5: **Raw image at 17 keV threshold**

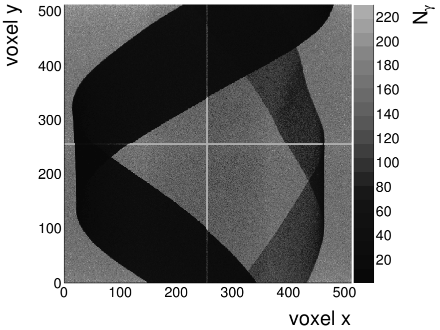

Figure 6.6: **Raw image at 28 keV threshold**

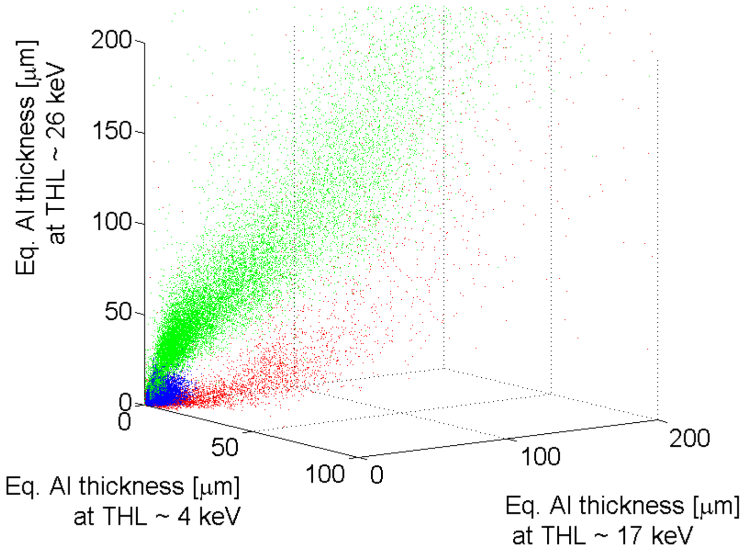

Figure 6.7: **Correlation plot of the voxel values at the three thresholds. The colors (blue-plastic, red-copper, green-cadmium) are assigned a posteriori to guide the eye.**

The final reconstruction, obtained by assigning materials/colors according to this scheme, is shown in figure 6.8, where a snapshot of a final three dimensional view is reported after noise reduction via Gaussian filtering.

6.3 Inclusion of spectral information in OSEM

The method described in section 6.2 exploits the correlations in the CT numbers at different thresholds to assign materials in X-ray tomographic data.

This approach is not complete. By carefully looking at figure 6.8, one may notice that the reconstruction presents voxels with mis-assigned colors. Especially, the two metallic bands are surrounded by a halo of blue voxels, which does not correspond to reality: there is no plastic around the metal strips.

The reason for this can be attributed to the fact that the three reconstructions are separately performed with a conventional algorithm, and the spectral information, although somehow exploited after the reconstruction, is not yet

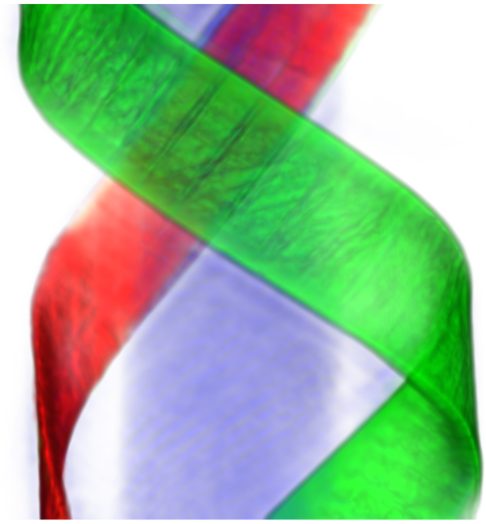

Figure 6.8: **Color tomography: blue-plastic, red-copper, green-cadmium.**

included in this phase.

In the desire to improve the reconstruction, the OSEM algorithm is modified such that spectral information is included. This approach, compared to the more natural statistical approach that will be described in section 6.4, will turn out to be impractical and, in general, at least for the formulation presented hereafter, it will prove to be suitable only for a limited subset of sample geometries. However, this strategy represents a good stepping stone to show the kind of benefits that spectral tomography can produce compared to conventional CT.

6.3.1 A spectral OSEM algorithm

The way to include full spectral information in OSEM is by modifying the expectation step as exposed in section 1.5.1 into a procedure in which the forward projection is calculated by transmitting the actual source spectrum through the estimated reconstruction.

In order to calculate the attenuation of the beam through the sample, the material composition of this latter has to be estimated as well. The new algorithm thus needs to include a further step in the iteration in which, just before the expectation step, the material distribution is determined.

In the following, few examples on simulated data will make the whole procedure clear, and will show the fundamental limitations of this approach.

Simulation of an ideal dataset

As a first test, a simulated dataset is generated using the virtual phantom shown in figure 6.9b and an ideal bremsstrahlung X-ray tube spectrum $S_0(E)$ with energies up to 40 keV (figure 6.9c).

The object is made of three different materials: aluminium, titanium and iron at the nominal densities, whose distributions in the (x, y) plane are discretized in voxels of 55 μm pitch. These materials will be encoded by the colors purple (aluminium), green (titanium) and red (iron) in the following discussion.

Three different datasets at 3 keV, 10 keV and 20 keV thresholds are simulated, including Poisson noise from photon statistics (figures 6.9d, 6.9e and 6.9f). The detector is assumed to be a 300 μm thick pixel silicon sensor with 55 μm pixel pitch. For simplicity, the energy response function of the detector is taken to be an ideal Dirac delta at any energy. In this situation, and using the $d_{ij}^{l,\theta}$ coefficients notation introduced in section 1.4, the detected number of photons at each ray path l, θ is given by

$$N_{l\theta} = \int_{E_t}^{\infty} S_0(E) e^{-\sum_{i,j} d_{i,j}^{l,\theta} \mu_{ij}(E)} dE, \tag{6.1}$$

where E_t is the energy threshold of the detector and $\mu_{ij}(E)$ is the energy dependent absorption coefficient at position i, j, corresponding to the nominal absorption coefficient of the material present in this voxel.

Reconstruction

The crucial phases of the reconstruction algorithm are illustrated in figure 6.10 for the case of iteration 1. For a better view of the individual steps of the reconstruction, these figures are produced for the algorithm run with only one subset corresponding to the full set of projections.

Figures 6.10a, 6.10b and 6.10c show the three images obtained from the first backprojection of the datasets at each threshold.

By looking at the correlations in the CT number space (as explained in section 6.2.1), a first estimation of the distribution of the three materials is produced, as shown in figure 6.10d.

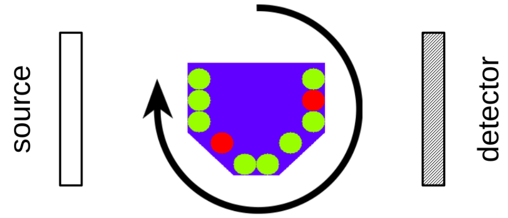

(a) **Setup settings.**

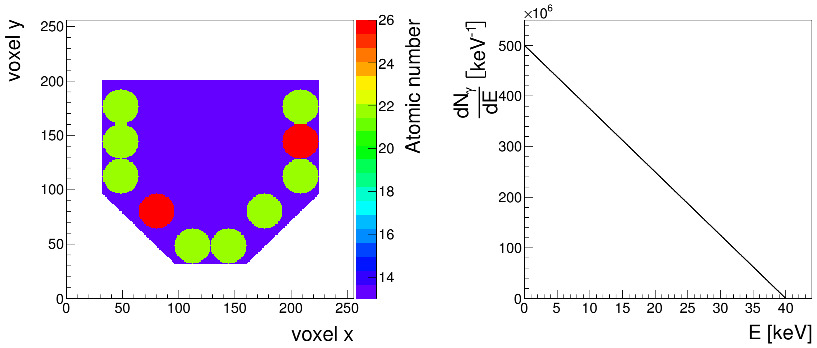

(b) **Virtual phantom: purple-aluminium, green-titanium, red-iron.**

(c) **Ideal bremsstrahlung spectrum.**

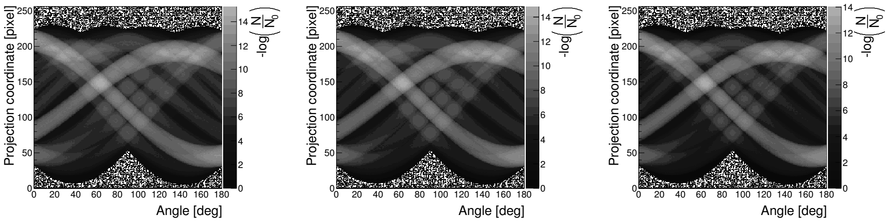

(d) **Sinogram at 3 keV.**

(e) **Sinogram at 10 keV.**

(f) **Sinogram at 20 keV.**

Figure 6.9: **Simulation of an X-ray CT dataset under ideal detection conditions.**

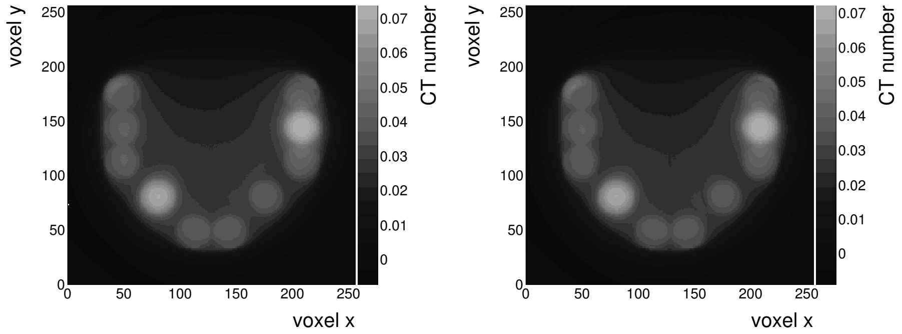

(a) **Backprojection at 3 keV.**

(b) **Backprojection at 10 keV.**

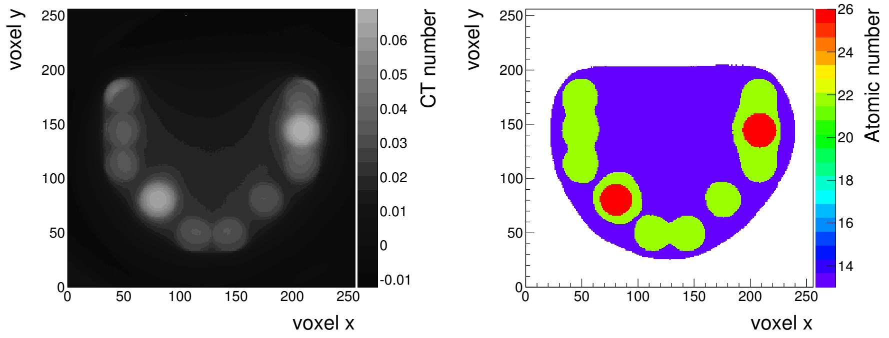

(c) **Backprojection at 20 keV.**

(d) **Material assignment: purple-aluminium, green-titanium, red-iron.**

Figure 6.10: **Iteration 1 of the modified OSEM algorithm.**

Formula 6.1 can now be applied to this data and three sets of projections, one per threshold, are calculated. The new projections are then compared to the simulated measurement, and correction coefficients are determined. These coefficients are finally backprojected and applied to the corresponding images in the CT number space (the ones represented in figures 6.10a, 6.10b and 6.10c).

Using the updated images, a new correlation plot is made, and materials are re-assigned. Iteration 2 can now be performed.

Result

The parameter employed to determine the convergence of the algorithm is the root mean square distance between the computed sinograms and the measured ones in the projection step. When the change in this parameter between two successive iterations is lower than 1%, the algorithm is stopped. In the most general case, when the data is divided into subsets, the first convergence condition can be followed by a new set of iterations on the full set of data, until a better convergence condition is reached.

The final reconstruction is shown in figure 6.11. Here the final image (figure 6.11c) is compared to the equivalent ones obtained by applying the material assignment technique through the CT number correlation plot to the images reconstructed with a filtered backprojection algorithm (FBP, figure 6.11a) and with a conventional OSEM (figure 6.11b).

The mis-assignment of the materials is very strong in the FBP case, and although the OSEM technique leads to a far better result, artifacts are still visible. The reconstruction with the modified OSEM algorithm shows that the effect is drastically reduced.

However, this is only true as long as the three metals are concerned. The boundary regions between the aluminium (purple) and the open beam (white) present clear mis-reconstructions in the regions where sharp edges are located, especially the two topmost corners. Indeed, as it will be clear in the next examples, this formulation of the algorithm only works when applied to very simple geometries, such as cylinder sections.

In the next step, the algorithm is improved from the ideal case by leaving the ideal conditions and by adapting the forward projector to the case of a Medipix based silicon detector.

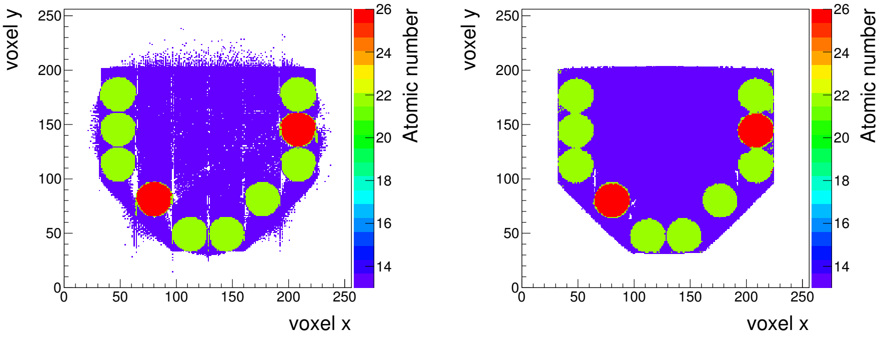

(a) **Material assignment in FBP.** (b) **Material assignment in OSEM.**

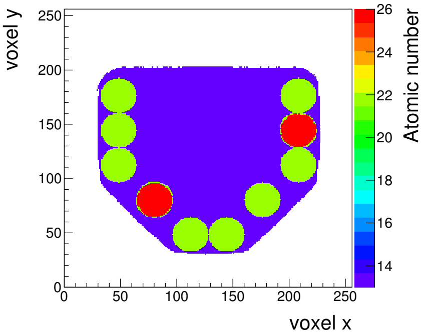

(c) **Final reconstruction from the modified OSEM algorithm.**

Figure 6.11: **Final reconstruction and comparison with FBP and OSEM: purple-aluminium, green-titanium, red-iron.**

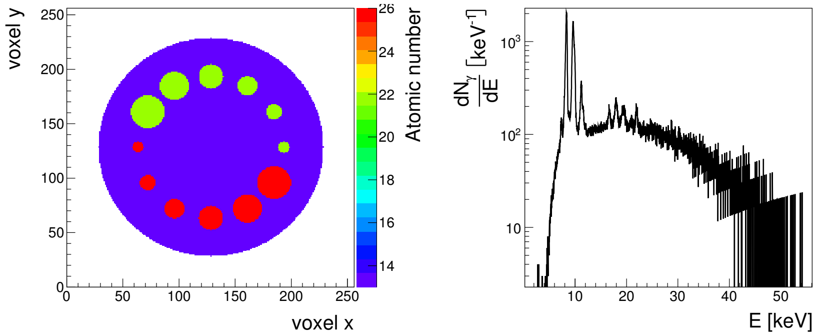

(a) **Virtual phantom: purple-aluminium, green-titanium, red-iron.**

(b) **Source spectrum.**

Figure 6.12: **Simulation of an X-ray CT dataset using a real X-ray tube spectrum and the energy response of a Medipix based silicon detector.**

Inclusion of the detector response function

Another simulation is performed to reproduce a more realistic reconstruction. The virtual phantom, shown in figure 6.12a, contains the same materials as the previous one (aluminium, titanium and iron, represented in purple, green and red, respectively), arranged in cylinder sections of different sizes, on a mesh of 256 × 256 square voxels of 55 μm pitch.

The source spectrum is taken from a measurement from a tungsten anode X-ray tube operated at 50 kV, obtained using a silicon drift detector (the same mentioned in section 5.5). The spectrum, after calibration and deconvolution of the absorption in the sensor (see section 5.5), is shown in figure 6.12b, in logarithmic scale.

Once again, three different tomography scans are simulated at three thresholds: 3, 13 and 25 keV. This time, the energy response function as determined in chapter 5 is applied to the transmitted spectra before integration according to formula 5.5, in order to simulate a 300 μm thick silicon sensor operated at 100 V and read out by a Medipix chip.

Not only Poisson noise is applied to the final images, but also the typical Medipix noise arising from the inter-pixel threshold variation is implemented. This latter is taken from an actual measurement of the threshold dispersion at each threshold value.

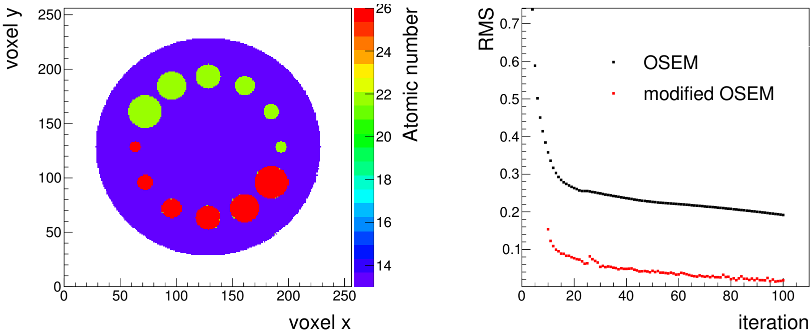

(a) **Final reconstruction: purple-aluminium, green-titanium, red-iron.**

(b) **Convergence plot. RMS is the root mean square distance of the raw sinogram from the calculated sinogram at each iteration.**

Figure 6.13: **Reconstruction.**

The simulated data are first fed into a conventional OSEM reconstruction algorithm. After 10 iterations, the algorithm is stopped and the resulting images are used to initialize the modified spectral OSEM algorithm. After 100 iterations, the reconstructed image looks like the one shown in figure 6.13a. This image differs from the true sample (figure 6.12a) only in few pixels. As the plot in figure 6.13b shows, the convergence of the spectral version of the algorithm is faster than the one of the conventional algorithm.

6.3.2 Limitations

Even though obtained under controlled conditions, the previous results on simulated data show that the inclusion of spectral information in the tomographic reconstruction algorithm leads to a concrete improvement in the quality of the final images.

However, the OSEM scheme, at least in the formulation reported here, is not the proper framework for spectral computed tomography. One of the reasons for this was already clear in the reconstruction in figure 6.11c where, even though the material assignment was properly done for titanium and iron, the procedure fails at the boundaries between the aluminium and the open beam, especially where sharp corners are present.

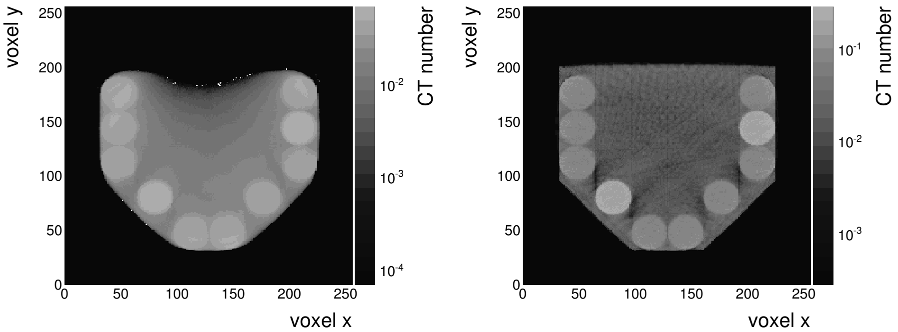

(a) **Spectral OSEM.**

(b) **OSEM.**

Figure 6.14: **Distortion in the CT number space in the spectral OSEM algorithm, and comparison with conventional OSEM, for the 20 keV dataset.**

The reason for this is that in this algorithm the material space and the CT numbers space are decoupled. The effect of substituting the simple algebraic expectation step in OSEM with the projector 6.1 (or the equivalent one after the application of the detector energy response) is that at each iteration the CT numbers are redistributed in order to compensate for beam hardening.

This situation is clarified in figure 6.14. Figure 6.14a shows as an example the final CT space image for the 20 keV dataset obtained with the modified OSEM algorithm, while figure 6.14b presents the corresponding reconstruction via conventional OSEM. In both images the grayscale is logarithmic.

The beam hardening artifacts, appearing as dark shadows in the space between the cylinder sections in the bottom half of the sample reconstructed with conventional OSEM in 6.14b, disappear in the other image 6.14a. However, the modified algorithm introduces inhomogeneities in regions where the CT numbers distribution should be flat. These are particularly visible in the core of the aluminium structure and in the topmost titanium cylinder sections, both regions that appear much more homogeneous in the other reconstruction.

Although this redistribution does not seem to affect the material assignment strategy in the regions of the cylinder sections (and indeed, there was almost no mis-assignment in the reconstruction of the second sample, figure 6.13a, which is made by just convex structures), this effect is completely destructive in the zones where sharp corners are present.

When attempting to apply the algorithm to data derived from samples with

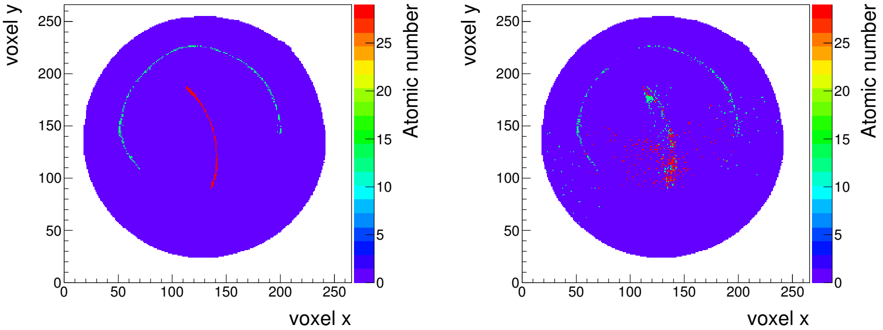

(a) **Virtual phantom.** (b) **Reconstruction at iteration 40.**

Figure 6.15: **Spectral OSEM algorithm applied to an object with concave structures: purple-wax, green-aluminium, red-copper. The convention here is that wax is assigned atomic number 1.**

more complex geometries, the reconstructed images diverge after a few iterations. This situation is illustrated in figure 6.15, for a sample containing concave structures made of metal components (aluminium and copper) in a substrate of low attenuating material, in this case wax (figure 6.15a). The reconstruction after 40 iterations, shown in figure 6.15b, exhibits the divergence from the true image. A possibility to solve this problem is to define new backprojection operators, that would take into account for the material information estimated during the iteration [5]. However, this solution adds complexity to the reconstruction algorithm, while a more natural implementation can be achieved in a statistical algorithm.

6.4 Statistical algorithm

Opposite to all other approaches, the statistical formulation of the tomographic reconstruction problem provides a natural framework for the extension to spectral CT, which makes this approach preferable with respect to OSEM.

6.4.1 Formulation

Extending the maximum likelihood problem introduced in section 1.6.1 to the case of spectral computed tomography requires the substitution of formula 1.20

with a proper expression for the expectation value of the Poisson distributions at each detector pixel. This way, the polychromatic nature of the X-ray source spectrum is taken into account.

The starting point for this extension is expression 1.24, that is hereby repeated by writing the energy dependent absorption coefficient $\mu(x, y, E)$ as the product of the density distribution $\rho(x, y)$ and the mass attenuation coefficient $\mu(E)/\rho$:

$$S_{out}(E, x) = S_{in}(E)e^{-\int \rho(x,y)\frac{\mu(E)}{\rho}dy}. \tag{6.2}$$

This formula defines an X-ray spectrum $S_{out}(E, x)$ resulting from the attenuation of a source spectrum $S_{in}(E, x)$ through the density field $\rho(x, y)$ along the y direction.

$S_{out}(E, x)$ is the spectrum that reaches the detector. The effective spectrum seen by the detector is the result of the distortions undergone by $S_{out}(E, x)$ as a consequence of the energy dependent detector efficiency and other phenomena, such as charge sharing.

All these effects are accounted for in the definition of the energy response function $R(E; E')$. According to formula 5.5, the effective spectrum deriving from $S_{out}(E, x)$ can be written as

$$S_{eff}(E, x) = \int_0^\infty R(E; E')S_{out}(E', x)dE'. \tag{6.3}$$

In order to simplify the notation, this formula will be used throughout the rest of the treatment even if, as discussed in section 5.5, $S_{eff}(E, x)$ will be calculated as the superimposition of the separate contributions from the central pixel and its neighbors.

For a photon counting detector, the signal issued by pixel x, set at threshold $E^{th}(x)$, is finally given by

$$I^{th}(x) = \int_{E^{th}(x)}^\infty S_{eff}(E, x)dE. \tag{6.4}$$

More generally, for a ray path l, θ, the full expression of the associate signal has the form

$$I^{th}_{l,\theta} = \int_{E^{th}_l}^\infty dE \int_0^\infty dE' R(E; E')S_{in}(E')e^{-\int_{l,\theta}\rho(s)\frac{\mu(E)}{\rho}ds}, \tag{6.5}$$

where s is the coordinate along the ray path l, θ. This expression is the new expectation value for the Poisson distribution 1.21.

Notice that no term was added to the model that accounts for detector noise. Such a term is usually introduced as a constant offset in formula 6.4 (see, for example [24]). However, photon counting detectors, such as Medipix based semiconductor detectors, can be operated in electronic-noise free conditions, which makes the addition of such term superfluous.

6.4.2 Definition of the likelihood function

In the maximum likelihood formulation of the tomographic reconstruction problem (see introduction in section 1.6.1), the X-ray projections obtained from the CT scan of the sample are interpreted as a collection of random variables $C_{l,\theta}^{th}$ distributed according to a probability density function

$$P(\vec{C}|\vec{I}) = \prod_{l,\theta,th} \frac{(I_{l\theta}^{th})^{C_{l\theta}^{th}} e^{I_{l\theta}^{th}}}{C_{l\theta}^{th}!}, \tag{6.6}$$

where $I_{l,\theta}^{th}$ is now given by expression 6.5 and $\vec{C}$ and $\vec{I}$ indicate the set of all values of $C_{l,\theta}^{th}$ and $I_{l,\theta}^{th}$ respectively.

Spectral information is included in the definition of $P(\vec{C}|\vec{I})$ at two levels:

1. at sample level, through the definition of the $I_{l,\theta}^{th}$'s via formula 6.5;

2. at detector level, through the inclusion of the th parameter, representing the threshold position.

As a matter of fact, these two points relate to the two different areas of the problem where energy dependencies play a role:

1. the transmission of the source spectrum through the sample, and the distortion of the resulting spectrum in the sensor material;

2. the spectral capability of the detector, achieved by repeating the same measurement at different values of the threshold.

Notice that the formulation of the expectation values according to formula 6.5 takes into account the inter-pixel threshold mismatches, since the energy threshold E_l^{th} for each pixel l appears explicitely. These values can be determined precisely by performing a per-pixel calibration (see chapter 3).

6.4.3 Expansion onto material basis functions

As defined up to now, the solution of the maximum likelihood problem is stated as follows: given the set of observed values $C^{th}_{l,\theta}$, determine the $\mu(x, y)$ distribution that maximizes the probability density function 6.6. However, $\mu(x, y)$ is not sufficient to achieve material separation, because different materials may show the same absorption properties. In order to discriminate between different materials, the density $\rho(x, y)$ must be determined.

One possibility of isolating $\rho(x, y)$ is by following the dual energy formulation and expand the absorption coefficient onto a set of basis functions [2]. The natural choice of the basis functions is the mass attenuation coefficient[2] of the N different materials that are expected to be present in the imaged object. Thus, one can write

$$\mu(x, y, E) = \sum_{n}^{N} \rho_n(x, y) \frac{\mu_n(E)}{\rho_n}, \tag{6.7}$$

where n is the material subscript and ρ_n is the constant nominal density of material n.

The unknowns with respect to which the likelihood function has to be maximized are now the $N \times N_v \times N_v$ values $\rho_n(x, y)$, where N_v is the number of voxels of the reconstructed image.

The implementation can be simplified by rewriting the expansion as

$$\mu(x, y, E) = \sum_{n}^{N} f_n(x, y) \mu_n(E), \tag{6.8}$$

where the $f_n(x, y)$'s are the new unknowns, defining the relative density of material n at voxel (x, y). Substituting this expansion into expression 6.5 yields a final formula for the Poisson expectation values:

$$I^{th}_{l,\theta} = \int_{E^{th}_l}^{\infty} dE \int_0^{\infty} dE' R(E; E') S_{in}(E') e^{-\sum_n^N \mu_n(E) \int_{l,\theta} f_n(s) ds}. \tag{6.9}$$

If material n is present inside the object in uniform and homogeneous clusters that are larger than the voxel size, then the corresponding $f_n(x, y)$ is a discrete field that can take only values: one if voxel (x, y) contains material

---

[2] Following the original dual energy concept, in principle separation of the photoelectric from the Compton cross section could be done as well [2].

n, zero otherwise. In the most general case $f_n(x, y)$ is a continuous function that can take all values between zero and one. It therefore expresses the effective concentration of material n inside voxel (x, y), which reflects two typical conditions:

1. material n is located in small regions that only partially fill the volume of one voxel;

2. material n is "dissolved" into a substrate material, for example it is part of a liquid solution or of a more complex composite material.

Notice that the N materials don't need to be pure elements only. Expansion 6.7 (or 6.8) can be done in terms of mass absorption coefficients and densities of specific compounds or materials, like water, fat and bones, just to mention an example from the medical field.

The multiple energy set of equations is diagonalizable only if N measurements at different energy settings are performed. The difference of the spectral CT formulation with respect to conventional multiple energy CT (e.g. dual energy CT) is that the multiple-energy information is not achieved by simultaneously imaging the sample with several different X-ray sources, but by repeating the measurement at different detector thresholds. This approach has a clear advantage in that only one source is required, meaning that no increase of dose is needed as in conventional multiple energy systems. This can be made possible thanks to new detector readout concepts, like Medipix3, where the N measurements at N different thresholds are performed within a single exposure.

6.4.4 A simulation study

First tests of the algorithm have been conducted through a simulation study implemented in RooFit [68, 54]. The function returning the detected intensity given by formula 6.9 as a function of the X-ray path l, θ and the pixel threshold t is used to calculate the expectation values entering the Poisson probability density function 6.6.

The physics model is based on the energy response function of a 300 μm thick silicon detector read out by an energy dispersive pixel chip of the Medipix family, as determined through the measurements described in chapter 5.

A simulated dataset is generated for a simple object discretized on a 20×20 voxel grid. The sample, shown in figure 6.16, consists of an aluminium cluster (in green) and a separated cluster of iron-filled voxels in air (in red). Iron is also

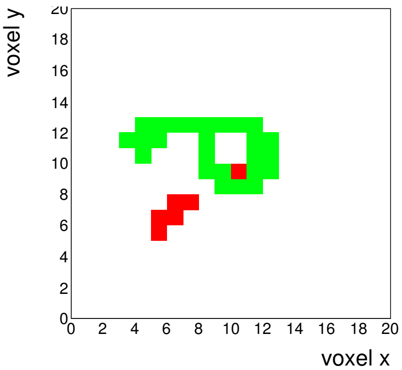

Figure 6.16: **Virtual sample. Small clusters, in red = iron; large cluster, in green = aluminium.**

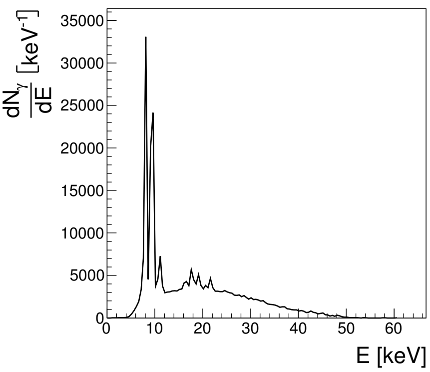

Figure 6.17: **Tube spectrum.**

present inside the aluminium volume. The X-ray spectrum, shown in figure 6.17, reproduces a tungsten anode tube spectrum at 50 kV.

A CT scan is simulated for 60 projections at 3° angle steps. Three simultaneous datasets at 4, 10 and 20 keV detector thresholds are generated (figures 6.18, 6.19 and 6.20).

The resulting reconstruction is shown in figures 6.21 and 6.22, where the aluminium and iron components of the $f_n(x, y)$ field are given.

6.4.5 Discussion

The results presented by this simulation show that the two materials can be perfectly separated. In particular, the sample geometry was chosen to be as more complex as possible in order to study whether specific structures, such as holes, appendices or concavities, could lead to image artifacts or to divergence, as it was in the case of the improved OSEM algorithm.

For this study, the size of the sample could not been extended further than 20×20 pixels, due to the fact that, before being able to handle larger datasets, RooFit needs to undergo few optimizations. The reason for this is that, for the typical applications in high energy physics, RooFit is conceived to work on complex likelihood functions but with a relatively small number of parameters. To give an example, one of the most well known problems in high energy physics

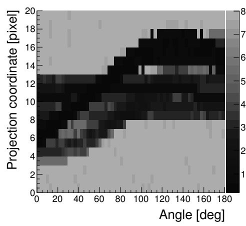

Figure 6.18: **Generated data at 4 keV threshold.**

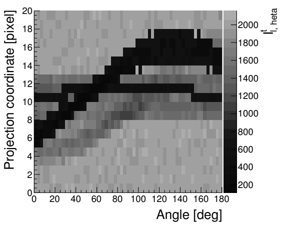

Figure 6.19: **Generated data at 10 keV threshold.**

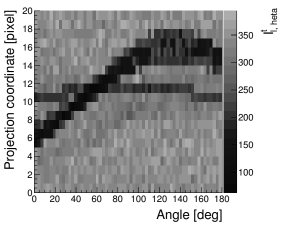

Figure 6.20: **Generated data at 20 keV threshold.**

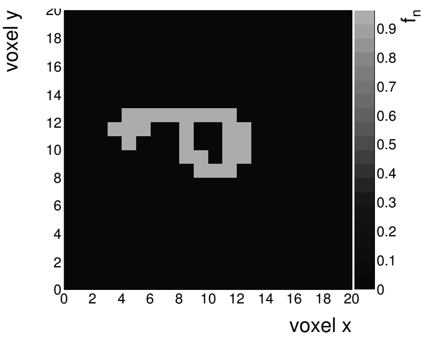

Figure 6.21: **Reconstruction of the aluminium component of the $f_n(x, y)$ field.**

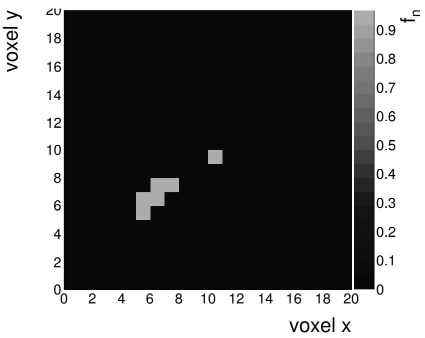

Figure 6.22: **Reconstruction of the iron component of the $f_n(x, y)$ field.**

has recently been the extraction of a Higgs boson signal from the data accumulated at the Large Hadron Collider [15]. For this analysis, the physics models are built in terms of probability density functions combining 23000 functions and 1600 parameters.

The case for computed tomography is rather the opposite. The probability density function, at least in the formulation presented here, is a product of Poissons depending on a huge number of parameters. This is in fact given by the number of voxels times the number of materials to be identified, which easily leads to values in the order of several tens of thousands. If one considers data from a single Medipix chip at full spatial resolution, then one would have $256 \times 256 \times N$ parameters in an algorithm for the identification of N materials and a voxel size of 55 μm. At the same time, the likelihood function would be defined as the product of $256 \times N_\theta \times N_{th}$ Poisson functions, where N_θ is the number of angles at which the CT scan is performed and N_{th} the number of thresholds at which the data are taken.

In order to develop a dedicated framework for the application of RooFit to CT, a working plan has been recently scheduled. As soon as the size of the sample can be scaled up, first tests on real data could be performed, with also the possibility to test the algorithm on biological materials.

6.5 Summary

The results presented in this chapter represent the final step of the work developed throughout the whole thesis. The goal of the project was to show how spectral CT is possible when using energy sensitive X-ray imaging detectors such as silicon sensors read out by Medipix chips. This improves X-ray imaging by leading to a material separation capability that is very hard to achieve in conventional CT, while in spectral CT it follows from the principles of the technique itself. What one obtains are color X-ray reconstructions, where each color represents a different material identified in the imaged object. Moreover, since spectral information is included in the reconstruction algorithm, beam hardening artifacts that usually appear in conventional CT images can be minimized.

The key role in this research line is played by the detector, which provides spectral capability at the level of single pixels. It has been shown that, to achieve material separation, it is not necessary to measure the full detected spectrum, but one only needs to take images at different energy thresholds and look at how the signals from different materials evolve as a function of the threshold value. Although conventional systems, such as dual energy scanners, already exploit this principle[3], spectroscopic pixel devices give this capability at the detector level. This means that multiple images at different thresholds can be taken simultaneously within a single exposure, thus keeping both the measurement time and the delivered dose at ordinary levels or lower levels.

The first result obtained by applying these principles was the one presented in section 6.2, figure 6.8, where it has been shown that materials can be separated when looking at the correlations of the CT numbers in the threshold space. However, this is not enough. This technique, in fact, is applied after the

---

[3] They may use either different threshold settings, or different sources or different detector sensitivity layers.

reconstruction, and not during the reconstruction. As a consequence, artifacts that are produced by conventional algorithms, such as beam hardening artifacts, are still present and produce errors in the assignment of materials.

The solution to this problem is the inclusion of the spectral information in the reconstruction algorithm, which is not done in conventional CT. This feature represents the second key point of spectral CT. In fact, the only valid method to account for spectral distortions and beam hardening artifacts is to incorporate these effects in the reconstruction phase in such a way that the data can be reproduced as truthfully as possible. This possibility, that required the detailed study of the energy response function of the detector presented in chapters 4 and 5, has been investigated in section 6.3, where an iterative spectral CT algorithm, based on an improved OSEM method, has been developed. Here it has been shown that, indeed, beam hardening artifacts can be strongly minimized, resulting in a better material assignment in the final reconstruction than the one obtained with the previous method.

However, at least in the formulation presented here, this algorithm yields good results only on a small subset of sample geometries. Although the method could be generalized[4], it still does not represent the most natural approach where to implement spectral information. For this reason, a different technique has been developed in section 6.4. The physical processes that lead to photon detection and the generation of the image are now accounted for in their statistical nature. Thanks to this, the maximum likelihood principle can be applied and the (vectorial) image can be reconstructed by determining the field that maximizes the associated probability density function. Preliminary studies have been carried out by employing RooFit, an analysis tool largely used in high energy physics, to implement the algorithm itself. The results show that materials can be well separated even for complex geometries.

Altogether, this work has shown the potential benefits arising from spectral CT in addressing the issues that typically appear in conventional CT. As a matter of fact, technologies like Medipix are regarded as the necessary evolution step for the next generation of X-ray imaging machines. In the next chapter, a general outlook will be provided on how this research can possibly be valorised.

---

[4] E.g., by implementing proper backprojection operators

Chapter 7

Future perspectives for spectral CT with Medipix

The work presented so far has been dedicated at investigating how spectroscopic pixel detectors based on readout chips of the Medipix family can be applied in spectral CT imaging, i.e. computed tomography exploiting energy information on single X-ray quanta.

Approaching the problem from the perspective of high energy physics has led us to the full understanding of the properties of our silicon sensor, and to the implementation of an image reconstruction algorithm based on RooFit, a tool widely employed in the particle physics community, which has proven to have potentials for spectral CT. In this chapter, the results are put in perspective regarding the possibility of applications outside high energy physics, with a discussion on the possible benefits for society.

7.1 Spectral computed tomography with Medipix

Everyone is familiar with X-ray images from the usual radiographs of the human body, where bones features appear light on a dark background because, having absorbed more radiation, they yield a higher value on the corresponding region in the image. In fact, the grayscale value in a specific position on a radiograph is connected to the total absorption of the X-ray beam while traversing the corresponding region in the sample.

However, a serious ambiguity arises, in that the combination of different materials in different proportions can lead to the same image value. This issue is addressed in current Computed Tomography (CT), i.e. three dimensional X-ray imaging, where the internal 3D geometry of the object is reconstructed, giving the possibility to estimate the thickness of the materials traversed by the beam in a specific direction. This information strongly constrains the set of possible material combinations that yield a specific intensity on the detector.

The limitation of conventional CT is that it only produces scalar images, i.e. images where the value assigned to each voxel (a 3D pixel) is still a grayscale number. This number (the CT number) is a measure of the absorption coefficient μ estimated at that position. This information is not yet enough to recognize materials, because different materials may have very similar, or even equal, absorption coefficients. What allows for discrimination is the energy dependence of μ, that is characteristic of each material.

7.1.1 Material separation

In the majority of X-ray imaging applications, the sources employed are vacuum tubes emitting highly polychromatic radiation. As a consequence, the final value estimated at a given voxel[1] position derives from a complex physical process where the incoming spectrum is distorted by the different materials according to their characteristic mass attenuation coefficient. If spectral information is measured instead of just beam intensity (or beam power), material information can be retrieved by deconvolving the relative contributions of the different attenuation coefficients to the detected signal.

An example of this principle is shown in figure 7.1. A color tomography, i.e. a computed tomography reconstruction in which different colors are assigned to different materials, is performed on a sample made of three different materials: plastic, copper and cadmium. The X-ray data are taken using a 512 × 512 pixels Medipix based silicon detector, and spectral information is estimated by repeating the measurement at three different energy thresholds. Material separation is achieved as a post-processing step, where identification of materials is performed after the 3D images at the three thresholds are reconstructed with a conventional algorithm. In this sense, this example cannot be regarded yet as a full representative of spectral CT, since spectral information is not included in the reconstruction phase.

The main work has thus been to develop reconstruction techniques suited for data taken with Medipix based detectors, that would account for spectral

---

[1] A voxel is a three dimensional pixel.

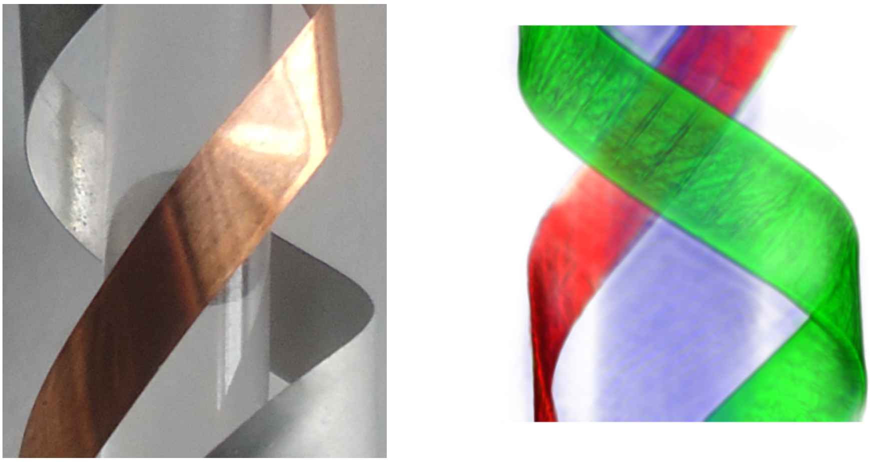

(a) **Picture of the sample. Copper and cadmium foils are wrapped around a plastic rod.**

(b) **Color computed tomography: blue-plastic, red-copper, green-cadmium.**

Figure 7.1: **Color CT proof of principle.**

information. The results show how to apply spectral CT to obtain vectorial 3D images, i.e. CT reconstructions where vectors are assigned to each voxel, whose elements correspond to the relative density of a specific material found at that position.

7.1.2 Reduction of beam hardening artifacts

Spectral CT not only leads to material resolved 3D images, but is also highly beneficial in minimizing the appearance of beam hardening artifacts in the reconstructed images, which are common in conventional CT. Few examples of such artifacts are shown in figure 7.2 for the case of medical X-ray computed tomography.

Beam hardening artifacts appear in conventional computed tomography because, although the X-ray source employed in CT scanners are highly polychromatic, spectral information is not measured by detectors, hence it cannot be accounted for in the reconstruction. Beam hardening is a well known issue that can strongly degrade image quality. Being able to eliminate, or at least mini-

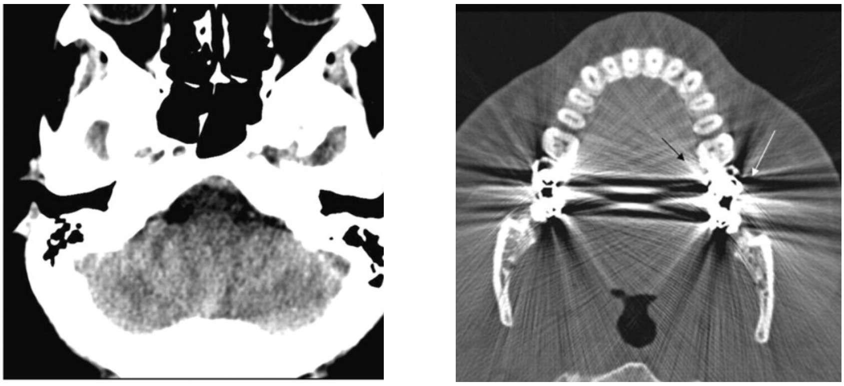

(a) **A dark band appears inside the skull.**

(b) **Streak artifacts are generated by dental metal implants.**

Figure 7.2: **Examples of beam hardening artifacts in medical X-ray computed tomography. Image credit [49].**

mize, the effect would lead to a significant improvement in the medical practice. Although the problem has been extensively addressed throughout the development of many pre- and/or post-processing techniques (see, for example, [10]), only spectral CT provides a direct solution. In this thesis, the strong reduction of beam hardening artifacts has been demonstrated for the case of spectral CT making use of Medipix based detectors.

7.2 Towards medical applications

Computed tomography is a well established technique in the medical practice. Beautiful and useful 3D X-ray images of the human body are reconstructed every day in many hospitals around the world, providing physicians with an invaluable diagnostic tool. So, why is there a need for spectral CT, and where can the Medipix technology, or similar ones, make a real difference?

There are two main reasons that make spectral CT with spectroscopic detectors so appealing. The first is that, for the first time, spectral CT would provide a definitive solution to the problem of beam hardening artifacts, which will improve significantly the quality of the images, and thus their diagnostic power. This would be beneficial, for example, also in treatment planning for radiotherapy, where the presence of artifacts can prohibit the automation of the procedure. Second, the possibility to achieve material separation opens the way towards imaging techniques that have been so far impossible, such as tissue resolved imaging and molecular imaging in X-ray computed tomography.

Tissue separation would be highly beneficial, for example, to distinguish fat from liver in the study of liver diseases. A pilot study has already demonstrated the capability of a Medipix based detector system to distinguish fat from liver in phantom specimens when taking CT data at different thresholds [6]. The application of spectral CT reconstruction techniques for Medipix based detectors, as the ones developed in this thesis, is therefore of high interest, since it may lead to valuable results for the clinical practice.

The other technique, molecular imaging, will make it possible to image specific functional areas in the body in computed tomography. This is achieved by injecting contrast agents chemically bound to cell specific substances which, via the blood circulation, are carried to a target area where they accumulate. If the contrast agent is a high density material (most common are gold nanoparticles, or iodine, or gadolinium), X-ray data will achieve high contrast in correspondence of the location of the region of interest. Medipix detectors are particularly suited for this purpose because, thanks to the availability of multiple simultaneous thresholds (up to 8 in Medipix3), different contrast agents can be used simultaneously, thus enhancing contrast in different target areas within a single X-ray scan.

7.3 Applications other than medicine

One may think of fields of application other than medicine where spectral CT with Medipix based detectors may be beneficial. For example, it has been recently suggested that computed tomography can be applied in quality control chains where industrial products need to be non-destructively inspected for inner defects [38]. Metrological studies could be performed on CT reconstructions of these objects in order to asses the properties of the specimen. Medipix in particular, thanks to its small pixel size (55 μm), would be suited for micro-CT metrology, where small samples need to be imaged.

Conventional CT is not enough for these applications, because beam hardening artifacts distort the images to such an extent that metrological information would be affected. Studies on the influence of beam hardening artifacts have been carried out where measurements before and after a post-processing based correction technique were compared [20, 64]. These results show that beam hardening corrections often introduce other artifacts that distort the geometry and structure of the visualized sample. On the contrary, spectral CT, being able to account for beam hardening in the reconstruction phase, would yield artifact free images. Studies of applications of spectral CT in industrial micro-metrology could possibly show the advantages from using the Medipix technology combined with a dedicated reconstruction algorithm.

7.4 Using RooFit for CT reconstruction: how fundamental research can lead to applications

Discoveries in science are usually done by people who want to satisfy their curiosity. Mr. Faraday and Mr. Maxwell did not disclose the secrets of electromagnetism with the goal of inventing telecommunications, and Mr. Anderson sure did not imagine that his positive electron would later be at the basis of the Positron Emission Tomography (PET) imaging systems widely employed in hospitals around the world.

The history of science is full of these examples. The discovery of the Higgs boson, announced on July 4th 2012, must be regarded as a curiosity driven result. However far from concrete applications it might seem, the technological advancements that almost 50 years of science have brought about since the Higgs mechanism was first conceived [2] are enormous. Such time span was needed to develop the tools that were necessary to finally realize the discovery at the Large Hadron Collider (LHC) at CERN: detectors, accelerators, superconductors, infrastructure, just to mention a few. All developments for which benefits were immediate also outside fundamental research. The most famous example is the World Wide Web, originally developed at CERN to share data and information among the scientists involved in large physics experiments, which soon became the most powerful communication system of the modern era.

The quest for the Higgs boson has also implied the evolution of the computing tools necessary for the treatment of the large amount of data generated by the LHC experiments. Extracting the needle-like signal of a new particle from a haystack of background events requires an analysis framework capable of modeling the underlying physics in the most precise and controlled way. For this reason, the open source ROOT framework [55], and specifically the RooFit

---

[2] The Higgs mechanism was proposed in 1964 to explain the presence of the masses of particles within the gauge invariant Standard Model.

toolkit, have been designed by the high energy physics community [68, 54]. In RooFit, complex probability density functions can be easily implemented and handled, and maximum likelihood fits to experimental data can be carried out efficiently.

From the formal point of view, this is exactly the same problem encountered in X-ray Computed Tomography. When using a statistical model of photon detection, CT data can be treated in terms of a multivariate probability density function, and the problem of image reconstruction is translated into a problem of likelihood maximization: find the values of the parameters (the image) that best reproduce the observed variables (the CT data).

The idea to export RooFit from fundamental research to X-ray CT is attractive since a reconstruction algorithm based on a statistical model provides a natural framework for the implementation of spectral information. The advantage of RooFit with respect to other similar toolkits is that the definition of the physics model and the actual minimization are treated separately. An analysis workspace containing all the necessary parameters and functions can be built once and for all in a very intuitive way. The workspace can be stored separately, and different datasets can be loaded into it when necessary. This saves much of the computation time dedicated to the model definition and allows for the separate optimization of the model. Once the data are loaded, different minimization engines can be chosen in order to run the reconstruction, offering different combination of computational speed and accuracy of the result.

The pilot experiments described in chapter 6 demonstrate the feasibility of the concept, giving a proof of principle that can be seen as a seed for future developments. With a dedicated research effort, RooFit, originally conceived for completely different types of problems, could be optimized also for computed tomography reconstruction, thus becoming competitive as an assessed toolkit for related applications, providing yet another example of how knowledge can be successfully exported from basic science to society.

Appendices

Appendix A

Signal to thickness calibration

The signal-to-thickness calibration is an image post-processing method to equalize the response of an X-ray imaging detector over the full sensitive area, and at the same time to minimize beam hardening effects.

The fundamental idea is to calibrate each detector element (e.g., each pixel) with signals from different thicknesses of a known material. For each pixel, the photon counts are recorded after the transmission of the source spectrum through different layers of this material. This data builds up a signal vs thickness relation for each detector element, as the one shown in figure A.1.

The signal vs thickness relation can be parametrized by simply interpolating the data points or by fitting it with local exponentials [33]. This latter method is based on the approximation that, in small energy intervals, the spectrum attenuation obeys the exponential law 1.1. Thus, at point k in the plot, one can set that the signal s is related to the thickness t via

$$s = A_k e^{B_k t} + C_k, \tag{A.1}$$

where A_k, B_k and C_k are the free parameters, to be determined for each point k.

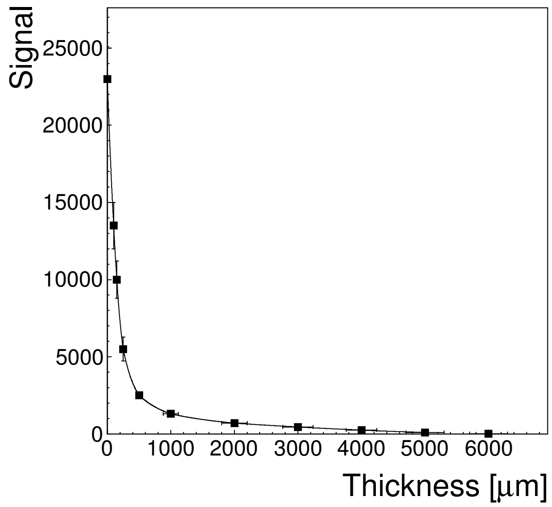

Figure A.1: **Signal-to-thickness calibration plot with aluminium as calibration material.**

This formula can be inverted to yield

$$
\begin{aligned}
t = {} & \frac{s - s_{k+1}}{B_k \left(s_k - s_{k+1}\right)} \log\left(\frac{s - C_k}{A_k}\right) + \\
& \frac{s_k - s}{B_{k+1} \left(s_k - s_{k+1}\right)} \log\left(\frac{s - C_{k+1}}{A_{k+1}}\right),
\end{aligned}
\tag{A.2}
$$

which gives the thickness t associated to a signal s laying between the calibration points k and $k+1$.

Formula A.2 can be used to calibrate the X-ray images taken with the same detector under the same experimental conditions (same settings of the detector and same X-ray spectrum) as in the taking of the calibration data. The resulting images are therefore corrected for systematic differences in the sensitivity of the detector elements. Moreover, beam hardening effects are minimized if the photon absorption coefficients of the different parts of the sample are not too different from that of the calibration material. If the sample is only made of the same material used for the calibration, then beam hardening artifacts are completely removed.

Notice that the calibrated images are expressed in units of equivalent thickness of the calibration material, which is an additive quantity. This means that CT projections calibrated with this method can be fed directly to a filtered backprojection, algebraic or OSEM algorithm (see chapter 1).

An example of the effect of the signal-to-thickness calibration is presented in figure A.2, where the X-ray image of a bee taken with a Medipix quad detector is shown before and after the correction. For this data, the calibration data was taken using different foils of aluminium at several thicknesses. Notice how the calibration enhances the fine details of the sample, including the venation structure of the wings and the hair around the body. The tape holding the bee in place is also visible.

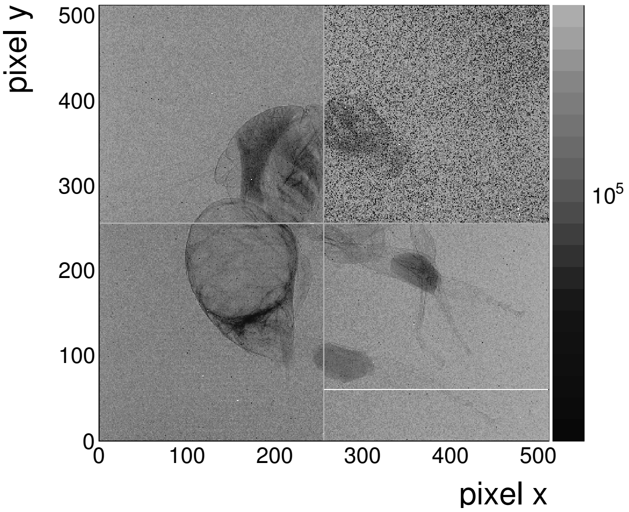

(a) **Raw image. Grayscale in units of photon counts.**

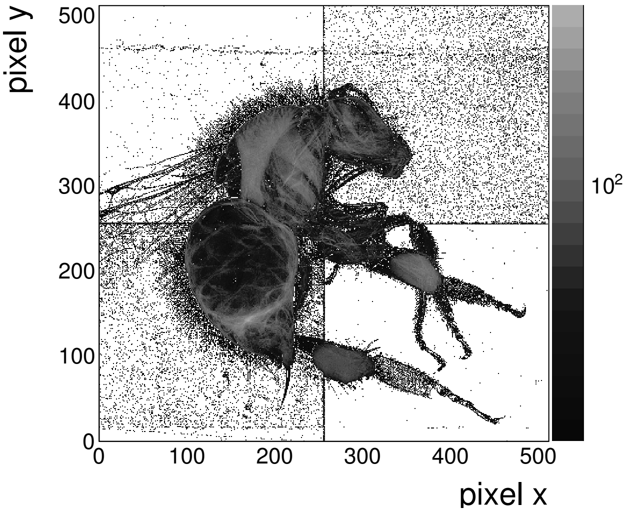

(b) **Calibrated image. Grayscale in units of equivalent thickness of aluminium, in μm.**

Figure A.2: **Application of the signal-to-thickness calibration.**

Appendix B

Medipix2 pixel logic

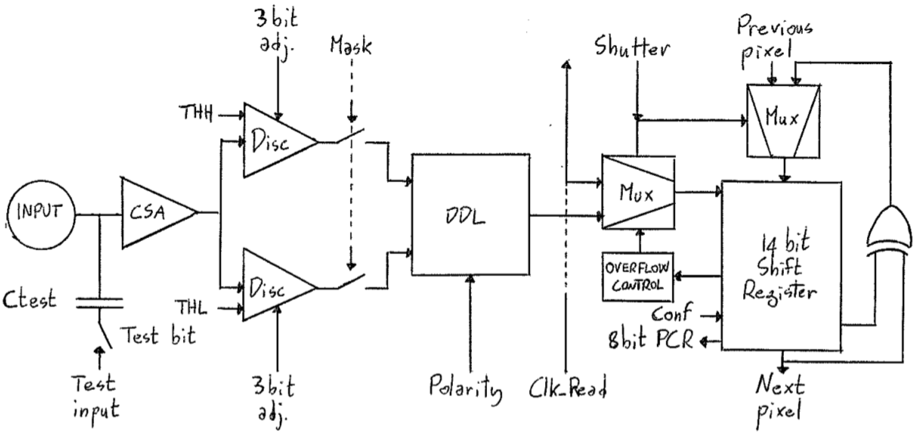

Figure B.1: **Schematics of the Medipix2 pixel logic.**

This appendix provides a more detailed explanation of the Medipix2 pixel cell logic, with reference to figure B.1. The pixel electronics can be separated into an analog and a digital circuitry.

Analog circuitry The charge collected at the input pad or via the test input is amplified and shaped by a Charge Sensitive Amplifier (CSA). The CSA also hosts a DC leakage current compensation system for noise reduction [37].

The analog signal is then multiplexed to the two discriminators, where it is simultaneously compared to the Low Threshold (THL) and the High Threshold (THH).

The global thresholds THL and THH are set by an external 8-bit Digital-to-Analog Converter (DAC). To correct for local transistor mismatches and minimize the inter-pixel threshold variation, each discriminator is provided with a 3-bit local threshold adjustment current source. The procedure through which the optimal values of this current are determined is the threshold equalization described in section 3.4.

Shutter	Polarity	Threshold	Operation Mode
OFF	-	-	OFF
ON	LOW (e^-)	$THH > THL$	Energy Window
ON	LOW (e^-)	$THH < THL$	Single
ON	HIGH (h^+)	$THH > THL$	Energy Window
ON	HIGH (h^+)	$THH < THL$	Single

Table B.1: **Operation modes of the Medipix2 Double Discriminator Logic.**

Digital circuitry The Medipix2 chip can be operated in two modes: single threshold and two thresholds (energy window) mode. The discrimination logic is implemented in the Double Discriminator Logic (DDL) unit, and can be configured to operate in both polarities (electron collecting or hole collecting) via the Polarity input bit (see table B.1).

Single threshold mode is automatically accessed when THH is below THL. In this configuration, the Double Discriminator Logic produces a digital output only if the signal is above THL. Conversely, when THH is above THL, energy window operation is activated. In this case, the DDL signal is issued only if the signal falls in the threshold window defined by THL and THH.

The output eventually generated by the Double Discriminator Logic is sent to the Shift Register and Counter (SR/C). Depending on the status of the shutter signal, the SR/C can be operated as a 13-bit digital counter or as a shift register that can be used either to shift the data from pixel to pixel up to the periphery to read out the full matrix after acquisition, or to set the Pixel Configuration Register (PCR). In the former case the output signal of the Double Discriminator Logic itself acts as the clock of the counter, while in the latter case an external clock (Clk_Read) is activated, and the pixel matrix is read out, provided that the configuration input bit (Conf) is inactive. If the Conf signal is active, the Shift Register and Counter is used to load the configuration bits into the Pixel Configuration Register.

The Pixel Configuration Register stores the 8-bit pixel configuration data (the 7-bit logic for the analog side plus 1 bit for masking the pixel). The PCR is a static system: the stored data is kept in memory until new data are overwritten or the chip is reset or shutdown. Every time the chip is switched on, the matrix configuration needs to be loaded.

The digital part of the pixel occupies an area of 32 μm $\times$ 55 μm, and hosts 450 transistors [72], thus representing the largest portion of the circuitry.

Appendix C

X-ray data

A list of the targets used for the generation of fluorescence radiation, along with some relevant X-ray properties [46], is provided in table C.1. All targets are pure metal foils of 0.001 inch thickness, with the exception of Mo, which is 60 μm thick. The K yield is the fraction of radiative processes (fluorescence emission) occurring to fill the K shell vacancy over the total number of vacancies created in the K shell [31].

Element	Z	K edge [keV]	K_α [keV]	K_β [keV]	K yield
Ti	22	4.965	4.510	4.931	0.214
Ni	28	8.333	7.477	8.264	0.406
Cu	29	8.979	8.047	8.904	0.440
Zn	30	9.659	8.638	9.571	0.474
Ge	32	11.104	9.885	10.981	0.535
Zr	40	17.988	15.774	17.666	0.730
Nb	41	18.986	16.614	18.621	0.747
Mo	42	19.999	17.478	19.607	0.765
Pd	46	24.350	21.175	23.816	0.820
Ag	47	25.514	22.162	24.942	0.831
Cd	48	26.711	23.172	26.093	0.843
In	49	27.940	24.207	27.274	0.853
Sn	50	29.200	25.270	28.483	0.862

Table C.1: **List of calibration targets and their X-ray properties.**

Appendix D

Per-pixel fit to fluorescence spectra

The goal of the procedure described in this appendix is to establish a method that maximizes the convergence yield when fitting the single-pixel fluorescence spectra. The work has been the topic of a bachelor student project [66].

Experience has shown that the convergence of the fit might depend strongly on the initialization of the parameters of the function. In this cases, the problem can be solved through a procedure wherein the optimal initialization values are determined automatically for each pixel.

The underlying idea is to fit the data using successive functions whose complexity is increased step by step, and whose parameters are initialized by the result of the previous stage. The initialization of the first function is performed by identifying the position of the main peak directly from the histogram of the differential spectrum.

An example of the algorithm is illustrated in figure D.1, D.2 and D.3. With reference to this figure, the individual steps, starting from the raw cumulative spectrum in figure D.1a, are described in the following.

1. Figure D.1b; The threshold scan is differentiated in order to retrieve the spectrum.

2. Figure D.2a; The approximate position of the K_α peak is determined by coarsely binning the differential spectrum. $E^{\alpha}_{p,i}$(here i is the pixel index) is taken as the value at the center of the highest bin.

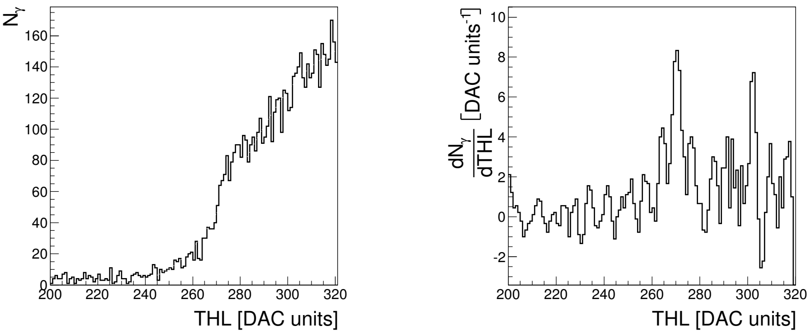

(a) **Cumulative spectrum.** (b) **Differential spectrum.**

Figure D.1: **Calibration of the low threshold (THL) of a Medipix2 based detector, per-pixel fitting procedure on fluorescence data from a silver target: differentiation of the raw scan.**

3. Figure D.2b; A second estimation of $E_{p,i}^{\alpha}$, plus a first evaluation of the Gaussian width $\sigma_{p,i}$ are realized by fitting the threshold scan via an error function modulated by a first degree polynomial

$$S_i(E) = \frac{A_i\left(x - x_i^0\right)}{2}\left[1 + \mathrm{Erf}\left(-\frac{E - E_{p,i}^{\alpha}}{\sqrt{2}\sigma_{p,i}}\right)\right], \tag{D.1}$$

where A_i and x_i^0 are the two temporary line parameters.

4. Figure D.3a; The scan is fitted via the K_α-only model, the integral version of function 3.30, whose full expression is

$$\begin{aligned} S(E) = N_p f_{cs}\Bigg\{ \frac{1}{2}\left(E - E_p + \frac{1}{f_{cs}}\right)\left[1 + \mathrm{Erf}\left(-\frac{E - E_p}{\sqrt{2}\sigma_p}\right)\right] \\ + \frac{\sigma_p}{\sqrt{2\pi}} e^{\frac{(E-E_p)^2}{2\sigma_p^2}} \Bigg\} + C_b E + S_0, \end{aligned} \tag{D.2}$$

with S_0 as an integration constant.

5. Figure D.3b; When the inclusion of the K_β peak is required (which is usually the case for targets with $Z \geq 32$) the scan is fitted via the 2-peaks

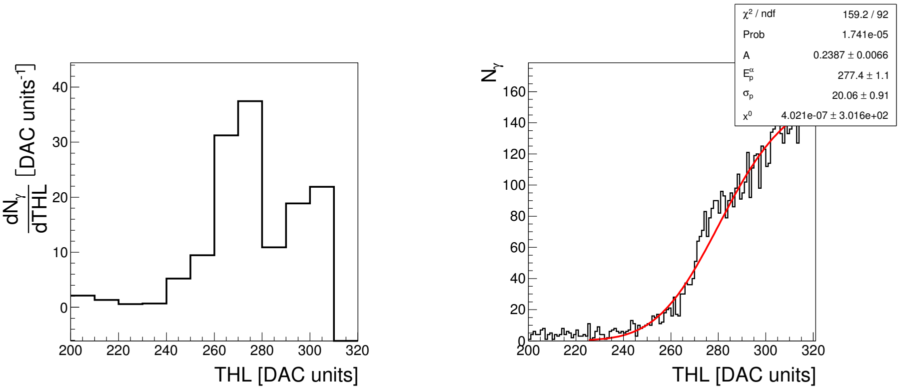

(a) **Rebinned differential spectrum.**

(b) **Fit of the scan via function D.1.**

Figure D.2: **Calibration of the low threshold (THL) of a Medipix2 based detector, per-pixel fitting procedure on fluorescence data from a silver target: rebinning and first fit.**

model defined by the integral of function 3.31. Explicitly:

$$\begin{aligned} S(E) = N_p f_{cs} \Bigg\{ & \frac{1}{2}\left(E - E_p^\alpha + \frac{1}{f_{cs}}\right)\left[1 + \mathrm{Erf}\left(-\frac{E - E_p^\alpha}{\sqrt{2}\sigma_p}\right)\right] \\ & + \frac{f_{\beta/\alpha}}{2}\left(E - E_p^\beta + \frac{1}{f_{cs}}\right)\left[1 + \mathrm{Erf}\left(-\frac{E - E_p^\beta}{\sqrt{2}\sigma_p}\right)\right] \\ & + \frac{\sigma_p}{\sqrt{2\pi}}\left[e^{\frac{\left(E - E_p^\alpha\right)^2}{2\sigma_p^2}} + f_{\beta/\alpha} e^{\frac{\left(E - E_p^\beta\right)^2}{2\sigma_p^2}}\right]\Bigg\} + C_b E + S_0. \end{aligned} \tag{D.3}$$

Notice that even after working out the integrals, expressions D.2 and D.3 are still algebraic summations of Gaussian and error function terms.

The performance of the algorithm is illustrated in figures D.4 and D.5, where the distributions of the (reduced) χ^2 from the fits to nickel and tin fluorescence data are shown as an example. The distributions are obtained as histograms over the χ^2 values over the full pixel matrix. Examples of the per-pixel fit they refer

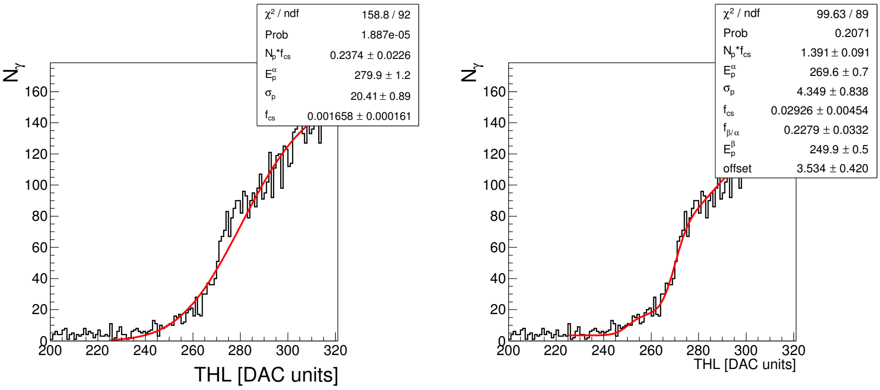

(a) **Fit of the scan via function D.2**

(b) **Fit of the scan via function D.3**

Figure D.3: **Calibration of the low threshold (THL) of a Medipix2 based detector, per-pixel fitting procedure on fluorescence data from a silver target: second and third fits.**

to were represented, respectively, in figures 3.5a and 3.5b in chapter 3. The cumulative versions D.6 and D.7 of the same distributions show that almost 100% of the pixels have $\chi^2 < 2$ in the case of Nickel, and $\chi^2 < 1.7$ in the case of Tin.

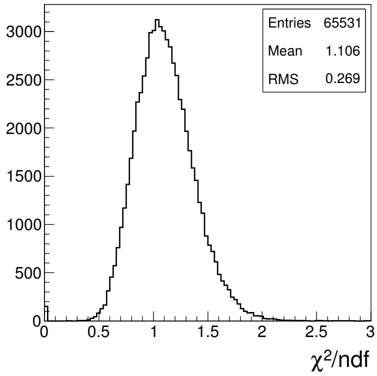

Figure D.4: χ^2 **distribution from the fit to Nickel fluorescence.**

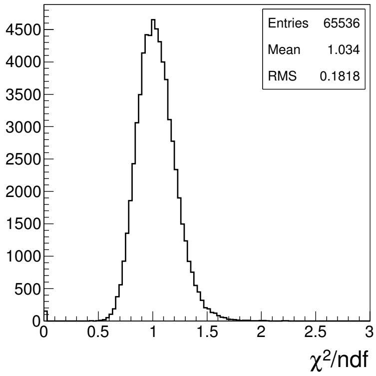

Figure D.5: χ^2 **distribution from the fit to Tin fluorescence.**

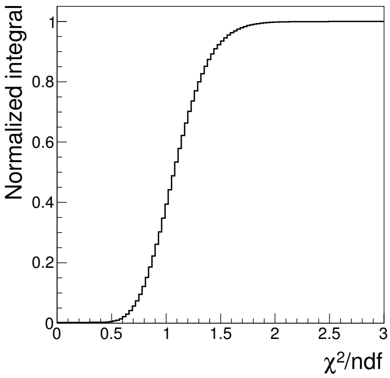

Figure D.6: **Normalized cumulative** χ^2 **distribution from the fit to Nickel fluorescence.**

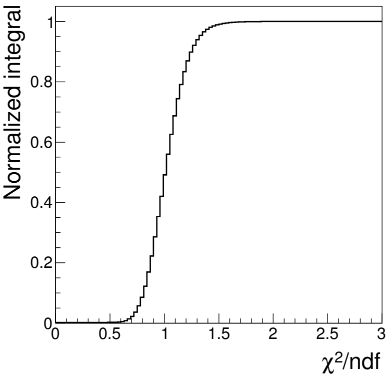

Figure D.7: **Normalized cumulative** χ^2 **distribution from the fit to Tin fluorescence.**

Appendix E

Diffusion in a uniform field gradient

In this appendix a simple model of diffusion and drift is developed assuming an ideal pn junction electric field increasing linearly as a function of the depth z in the sensor.

Using this assumption and the proportionality between the drift velocity and the electric field (relation 3.22), the drift velocity as a function of z can be written as

$$v(z) = \frac{z}{\tau} \tag{E.1}$$

for some time constant τ.

Since $v = dz/dt$, this formula leads to equation

$$\frac{dv}{dt} = \frac{v}{\tau}, \tag{E.2}$$

whose general solution is

$$v(t) = A + Be^{t/\tau}. \tag{E.3}$$

The condition $v(t = 0) = 0$ yields $A = -B$. By defining a dimensional constant $v_0 = -A$ then one can write

$$v(t) = v_0 \left(e^{t/\tau} - 1\right). \tag{E.4}$$

By comparing definition E.1 to relation 3.22, one sees that $\tau \propto (\mu \nabla E)^{-1}$. Using order of magnitude values for the mobility $\mu \sim 10^3 \mathrm{cm^2/Vs}$ and for the field gradient $\nabla E \sim 10^8 \mathrm{V/cm^2}$, one obtains $\tau \sim 10^{-11} s$, which corresponds to the typical time for a drift motion through 1 μm. Since here we are interested in distances of several tenths of microns, one can set $t \gg \tau$, and approximate formula E.4 with

$$v(t) = v_0 e^{t/\tau}. \tag{E.5}$$

The equation of motion is thus

$$z(t) = z_0 + v_0 \tau \left(e^{t/\tau} - 1 \right), \tag{E.6}$$

where z_0 is the initial value of z.

This formula can be inverted to give

$$t(z) = \tau \log \left(1 + \frac{z - z_0}{v_0 \tau} \right) \tag{E.7}$$

and therefore

$$\sigma(z) \propto \sqrt{\log \left(1 + \frac{z - z_0}{v_0 \tau} \right)}. \tag{E.8}$$

Bibliography

[1] L. Abate, E. Bertolucci, M. Conti, A. Di Cosmo, C. Di Cristo, G. Mettivier, M. C. Montesi, and P. Russo. Quantitative dynamic imaging of biological processes with solid state radiation detector. *IEEE Trans. Nuc. Sci.*, 47(6):1907–1910, 2000.

[2] R. E. Alvarez and A. Macovski. Energy-selective reconstructions in X-ray computerized tomography. *Phys. Med. Biol.*, 21(5):733–744, 1976.

[3] R. Ballabriga, M. Campbell, E. Heijne, X. Llopart, L. Tlustos, and W. Wong. Medipix3: a 64-k pixel detector readout chip working in single photon counting mode with improved spectrometric performance. *Nucl. Instr. Meth. A*, 633:S15–S18, 2011.

[4] W. Bambynek, B. Crasemann, R. W. Fink, H. U. Freund, H. Mark, C. D. Swift, R. E. Price, and P. Venugopala Rao. X-ray Fluorescence Yields, Auger, and Coster-Kronig Transition Probabilities. *Rev. Mod. Phys.*, 44(4), 1972.

[5] M. Beister, D. Kolditz, and W. A. Kalender. Iterative reconstruction methods in X-ray CT. *Phys. Med.*, 28:94–108, 2012.

[6] K. B. Berg, J. M. Carr, M. J. Clark, N. J. Cook, N. G. Anderson, N. J. Scott, A. P. Butler, P. H. Butler, and A. P. Butler. Pilot study to confirm that fat and liver can be distinguished by spectroscopic tissue response on a Medipix-All-Resolution-System-CT (MARS-CT). *AIP Conf. Proc.*, 1151(1):106–109, 2009.

[7] E. Bertolucci, T. Boerkamp, M. Maiorino, G. Mettivier, M. C. Montesi, and P. Russo. Portable system for imaging of α, β and X-ray sources

with silicon pixel detectors and Medipix1 readout. *IEEE Trans. Nuc. Sci.*, 49(4):1845–1850, 2002.

[8] J. Beutel, H. L. Kundel, and R. L. Van Metter. *Handbook of medical imaging.* SPIE Press, 2000.

[9] W. Blum, W. Riegler, and L. Rolandi. *Particle Detection with Drift Chambers.* Springer, 2008.

[10] F.E. Boas. Iterative reduction of artifacts in computed tomography images using forward projection and an edge-preserving blur filter, July 31 2012. US Patent 8,233,586.

[11] M. Borsboom and et al. The Dutch-Belgian beamline at the ESRF. *J. Synch. Rad.*, 5:518–520, 1998.

[12] W. S. Boyle and G. E. Smith. Charge Coupled Semiconductor Devices. *Bell Sys. Tech. J.*, 49(4):587–593, April 1970.

[13] M. Campbell, E. H. M. Heijne, G. Meddeler, E. Pernigotti, and W. Snoeys. A readout chip for a 64 × 64 pixel matrix with 15-bit single photon counting. *IEEE Trans. Nuc. Sci.*, 45(3):751–753, 1998.

[14] P. Colas, A. P. Colijn, A. Fornaini, Y. Giomataris, H. van der Graaf, E. H. M. Heijne, X. Llopart, J. Schmitz, J. Timmermans, and J. L. Visschers. The radout of a GEM or Micromegas-equipped TPC by means of the Medipix2 CMOS sensor as direct anode. *Nucl. Instr. Meth. A*, 535:506–510, 2004.

[15] ATLAS Collaboration. Observation of a new particle in the search for the Standard Model Higgs boson with the ATLAS detector at the LHC. *Physics Letters B*, 716:1–29, 2012.

[16] Medipix collaboration website. medipix.web.cern.ch/medipix/.

[17] A. M. Cormack. Representation of a function by its line integrals, with some radiological applications. *J. Appl. Phys.*, 34(9):2722–2727, 1963.

[18] A. M. Cormack. Representation of a function by its line integrals, with some radiological applications. II. *J. Appl. Phys.*, 35(10):2908–2913, 1964.

[19] A. P. Dempster, N. M. Laird, and D. B. Rubin. Maximum likelihood from incomplete data via the EM algorithm. *J. Royal Stat. Soc. B*, 39(1), 1977.

[20] W. Dewulf, Y. Tan, and K. Kiekens. Sense and non-sense of beam hardening correction in CT metrology. *CIRP Annals - Manufacturing Technology*, 2012.

[21] I. A. Elbakri and J. A. Fessler. Statistical image reconstruction for polyenergetic X-ray computed tomography. *IEEE Trans. Med. Im.*, 21(2):1–15, 2002.

[22] K. J. Engel, R. Steadman, and C. Herrmann. Pulse temporal splitting in photon counting X-ray detectors. *IEEE Trans. Nuc. Sci.*, 59:1480–1490, 2012.

[23] U. Fano. Ionization Yields of Radiations. The Fluctuations of the Number of Ions. *Phys. Rev.*, 72(1), 1947.

[24] J. A. Fessler. Method for statistically reconstructing images from a plurality of transmission measurements having energy diversity and image reconstructor apparatus utilizing the method, 06 2004.

[25] E. Gatti, A. Longoni, P. Rehak, and M. Sampietro. Dynamics of electrons in drift detectors. *Nucl. Instr. Meth. A*, 253:393–399, 1987.

[26] J. Giersch, D. Niederlöhner, and G. Anton. The influence of energy weighting on X-ray imaging quality. *Nucl. Instr. Meth. A*, 531:68–74, 2004.

[27] E. N. Gimenez, R. Ballabriga, M. Campbell, I. Horswell, X. Llopart, J. Marchal, K. J. S. Sawhney, N. Tartoni, and D. Turecek. Characterization of Medipix3 with synchrotron radiation. *IEEE Trans. Nuc. Sci.*, 99:323–332, 2010.

[28] P. Grangeat. *Tomography.* John Wiley & Sons, 2009.

[29] V. Gromov, M. van Beuzekom, R. Kluit, F. Zappon, V. Zivkovic, M. Campbell, T. Poikela, X. Llopart, C. Brezina, K. Desch, X. Fang, and A. Kruth. Development and applications of the Timepix3 readout chip. *Proc. Sc.*, SISSA:1–8, 2011.

[30] Z. He. Review of the ShockleyRamo theorem and its application in semiconductor gamma-ray detectors. *Nucl. Instr. Meth. A*, 463:250–267, 2001.

[31] J. H. Hubbel, P. N. Trehan, N. Singh, B. Chand, D. Mehta, M. L. Garg, R. R. Garg, S. Singh, and S. Puri. A review, bibliography and tabulation of K, L and higher atomic shell X-ray fluorescence yields. *J. Phyis. Chem. Ref. Data*, 23(2):339–364, 1994.

[32] H. M. Hudson and R. S. Larkin. Accelerated image reconstruction using ordered subsets of projection data. *IEEE Trans. Med. Im.*, 13(4), 1994.

[33] J. Jakůbek. Data processing and image reconstruction methods for pixel detectors. *Nucl. Instr. Meth. A*, 576:223–234, 2007.

[34] J. H. Jungmann, L. MacAleese, R. Buijs, F. Giskes, A. de Snaijer, J. Visser, J. Visschers, M. J. J. Vrakking, and R. M. A. Heeren. Fast, high resolution mass spectrometry imaging using a Medipix pixelated detector. *J. Am. Soc. Mass. Spec.*, 21:2023–2030, 2010.

[35] A. C. Kak and M. Slaney. *Principles of computerized tomographic imaging.* IEEE Press, 1988.

[36] M. O. Krause. Atomic radiative and radiationless yields for K and L shells. *J. Phys. Chem. Ref. Data*, 8(2):307–327, 1979.

[37] F. Krummenacher. Pixel detectors with local intelligence: an IC designer point of view. *Nucl. Instr. Meth. A*, 305:527–532, 1991.

[38] J. P. Kruth, M. Bartscher, S. Carmignato, R. Schmitt, L. De Chiffre, and A. Weckenmann. Computed tomography for dimensional metrology. *CIRP Annals - Manufacturing Technology*, 60:821–842, 2011.

[39] R. Kubo. The Fluctuation-Dissipation Theorem. *Rep. Prog. Phys.*, 29:255, 1966.

[40] L. D. Landau and E. M. Lifshitz. *Fluid Mechanics.* Pergamon Press, 2nd edition, 1987.

[41] A. Langenberg and J. van Eck. An Evaluation of K-shell Fluorescence Yields; Observation of Outer-shell Effects. *J. Phys. B; Atom. Molec. Phys.*, 12(8), 1979.

[42] X. Llopart, R. Ballabriga, M. Campbell, L. Tlustos, and W. Wong. Timepix, a 64k programmable pixel readout chip for arrival time, energy and/or photon counting measurements. *Nucl. Instr. Meth. A*, 581(1-2):485–494, 2007.

[43] X. Llopart, M. Campbell, R. Dinapoli, D. San Segundo, and E. Pernigotti. Medipix2: a 64-k pixel readout chip with 55-μm square elements working in single photon counting mode. *IEEE Trans. Nuc. Sci.*, 49:2279–2283, 2002.

[44] M. J. Bosma. *On the cutting edge of semiconductor sensors. Towards intelligent X-ray detectors.* PhD thesis, Universiteit van Amsterdam, 2012.

[45] B. De man, J. Nuyts, P. Dupont, G. Marchal, and P. Suetens. An iterative maximum-likelihood polychromatic algorithm for CT. *IEEE Trans. Med. Im.*, 20(10):999–1008, 2001.

[46] W. H. McMaster, N. Kerr Del Grande, J. H. Mallett, and J. H. Hubbell. *Compilation of X-Ray Cross Sections.* Lawrence Livermore National Laboratory Report UCRL-50174 Section II Revision I available from National Technical Information Services L-3, U.S. Dept. of Commerce, 1969.

[47] S. Nikitenko and et al. Implementation of a combined SAXS/WAXS/QEXAFS set-up for time-resolved in situ experiments. *J. Synch. Rad.*, 15:632–640, 2008.

[48] G. Nolet. *A breviary of seismic tomography.* Cambridge university press, 2008.

[49] R. Popilock, K. Sandrasagaren, L. Harris, and K. A. Kaser. CT Artifact Recognition for the Nuclear Technologist. *J. Nucl. Med. Tech.*, 36(2):79–81, 2008.

[50] J. L. Prince and J. M. Links. *Medical imaging signal and systems.* Pearson prentice hall bioengineering, 2006.

[51] R. Ballabriga. *The design and implementation in 0.13 μm CMOS of an algorithm permitting spectroscopic imaging with high spatial resolution for hybrid pixel detectors.* PhD thesis, Ramon Llull U., Barcelona, 2009.

[52] S. Ramo. Currents Induced by Electron Motion. *Proceedings of the IRE*, 27:584–585, 1939.

[53] A. J. Rockmore and A. Macovski. A maximum likelihood approach to transmission image reconstruction from projections. *IEEE Trans. Nuc. Sci.*, NS-24:1929–1935, 1977.

[54] RooFit. http://root.cern.ch/drupal/content/roofit.

[55] ROOT. http://root.cern.ch/.

[56] L. Rossi, P. Fischer, T. Rohe, and N. Wermes. *Pixel Detectors: from Fundamentals to Applications.* Springer, 2006.

[57] J. O. Schumacher and W. Wettling. *Device Physics of Silicon solar Cells, in Photoconversion of Solar Energy*, volume 3. M. Archer, Imperial College Press, London, 2000.

[58] L. A. Shepp and B. F. Logan. The Fourier reconstruction of a head section. *IEEE Trans. Nuc. Sc.*, NS-21:21–43, 1974.

[59] L. A. Shepp and Y. Vardi. Maximum likelihood reconstruction for emission tomography. *IEEE Trans. Med. Imaging*, M1-1(2), 1982.

[60] W. Shockley. Currents to Conductors Induced by a Moving Point Charge. *Journal of Applied Physics*, 9:635, 1938.

[61] W. Shockley. The Theory of p-n Junctions in Semiconductors and p-n Junction Transistors. *Bell Sys. Tech. J.*, 28:435–489, 1949.

[62] A. Stanton. Wilhelm Conrad Röntgen On a New Kind of Rays: translation of a paper read before the Würzburg Physical and Medical Society, 1895. *Nature*, 53:274–276, 1896.

[63] J. P. Stonestrom, R. E. Alvarez, and A. Macovski. A framework for spectral CT artifact corrections in X-ray CT. *IEEE Trans. Biom. Eng.*, BME-28(2):128–141, 1981.

[64] Y. Tan, K. Kiekens, F. Welkenhuyzen, J. P. Kruth, and W. Dewulf. Beam hardening correction and its influence on the measurement accuracy and repeatability for CT dimensional metrology applications. *Conference on Industrial Computed Tomography (ICT), 19-21 September 2012, Wels, Austria.*

[65] J. Uher and et al. X-ray beam hardening based material recognition in micro-imaging. *J. Instr.*, 6(P08015).

[66] R. P. M. van der Boog. *Energy calibration procedure of a pixel detector.* Bachelor thesis of applied physics (B. Eng.), The Hague university of applied sciences, 2013.

[67] R. van Grieken and A. Markowicz. *Handbook of X-ray spectrometry.* edited by R. van Grieken and A. Markowicz, 2nd edition, 2002.

[68] W. Verkerke and D. Kirkby. The RooFit toolkit for data modeling. *arXiv:physics/0306116*, 2003.

[69] J. Visschers. Timepix memo 24-10-2004/jv, private communication.

[70] J. Visser, B. van der Heijden, S. J. A. Weijers, R. de Vries, and J. L. Visschers. A Gigabit per second read-out system for Medipix Quads. *Nucl. Instr. Meth. A*, 633:S22–S25, 2011.

[71] J. Watt, R. Bates, M. Campbell, K. Mathieson, B. Mikulec, V. O'shea, M-S. Passmore, C. Schwarts, K. M. Smith, and C. Whitehill. Applications of pixelated GaAs X-ray detectors in a synchrotron radiation beam. *Nucl. Instr. Meth. A*, 460:185–190, 2001.

[72] X. Llopart Cudie. *Design and Characterization of 64k Pixels Chips working in single Photon processing mode.* PhD thesis, Mid Sweden University Doctoral Thesis 27, 2007.

Scientific output

The work presented in this thesis has led to the following scientific output:

Papers

Published:

- E. J. Schioppa, J. Uher and J. Visser, *Construction and test of an X-ray CT setup for material resolved 3D imaging with Medipix based detectors*, Journal of Instrumentation 7 C10007 (2013)
- E. J. Schioppa, S. Ellis, A. L. Bruinen, J. Visser, R. M. A. Heeren, J. Uher and E. Koffeman *Combined X-ray CT and mass spectrometry for biomedical imaging applications*, Journal of Instrumentation 9 C04029 (2014)
- E. J. Schioppa, D. Banerjee, J. Visser, T. Klaver, E. Koffeman and W. Bras *Measurement of the energy response function of a silicon pixel detector readout by a Timepix chip using synchrotron radiation*, Journal of Instrumentation 9 P08002 (2014)

Accepted:

- E. J. Schioppa, J. Visser and E. Koffeman, *Prospects for spectral CT with Medipix detectors*, Proceedings of Science

To be submitted:

- E. J. Schioppa, W. Verkerke, J. Visser and E. Koffeman, *Solving CT reconstruction with a particle physics tool (RooFit)*, Applied Numerical Mathematics, already published in the Proceedings of the NumAn2014 conference.

- E. J. Schioppa, E. Heijne, J. Idarraga, J. Uher, M. van Beuzekom, K. J. Engel, J. Visser and E. Koffeman, *Measurement of charge diffusion in a silicon detector using minimum ionizing particles* Journal of Instrumentation

Talks at international conferences

- *Construction and test of an X-ray CT setup for material resolved 3D imaging with Medipix based detectors*, 14th International Workshop on Radiation Imaging Detectors (IWoRID) 1-5 July 2012, Figueira de Foz, Coimbra, Portugal
- *Combined X-ray CT and mass spectrometry for biomedical imaging applications*, 15th International Workshop on Radiation Imaging Detectors (IWoRID) 23-27 June 2013, Paris, France
- *Prospects for spectral CT with Medipix detectors*, International Conference on Technology and Instrumentation in Particle Physics (TIPP) 2-6 June 2014, Amsterdam, The Netherlands
- *Solving CT reconstruction with a particle physics tool (RooFit)*, 6th International Conference on Numerical Analysis (NumAn) 2-5 September 2014, Chania, Crete, Greece

Other talks

- *The color of X-rays*, 2012 Nikhef annual jamboree, Utrecht, The Netherlands
- *Active pixel detectors for X-ray imaging applications*, 2013 annual meeting of the Dutch physics society, Lunteren, The Netherlands
- *Energy sensitive pixel detectors for X-rays imaging applications*, 2013 Nikhef annual jamboree, Amsterdam, The Netherlands

Teaching

- *Timepix; a hybrid pixel detector*, student lab at the 2nd International School on Intelligent Signal Processing in Frontier Research and Industry (INFIERI), July 2014, Paris, France

Summary

> *The retina of the eye is quite insensitive to these rays: the eye placed close to the apparatus sees nothing.*
>
> W. C. Röntgen, 1895 [62].

Professor Röntgen calls these rays “X-rays”, as he says, *for the sake of brevity* and probably to emphasize that, apart from the observation that *bodies behave to the X-rays as turbid media to light*, he knew very little about the nature of this phenomenon. To such an extent that he did not have any trouble in placing his own eyes just in front of what seems to have been a rather powerful radiation source if *Platinum 2 mm thick allows some rays to pass.* Today, we are well aware of the dangers of such an action, and radiation protection teams work hard in order to avoid such occurrences.

Apparently however, professor Röntgen was the first who, unwillingly, attempted to detect X-rays with an energy sensitive pixel detector: the human retina. Of course he could not see anything, because the retina is not at all sensitive to X-rays. The technology required to realize energy sensitive X-ray artificial retinas has become available only 100 years later. These detectors are made by connecting a semiconductor pixel sensor to an energy resolving readout chip and can be employed to achieve color, i.e. material resolved, X-ray imaging.

The principle of color vision in the retina relies on the presence of three types of “pixels”, the cone receptor cells, each having its sensitivity peak at a different wavelength. The incoming light spectrum is filtered by each receptor and the image is decomposed onto a basis of three colors (red, green and blue, see figure 7.1a).

Following a different concept, spectroscopic pixel readout chips for semiconductor X-ray detectors are able to separate an incoming radiation spectrum into multiple energy channels, at the level of single pixels. Compared to the retina principle, where three images in different color channels are obtained at the expense of spatial resolution (one out of three receptors are used to form each image), energy sensitive X-ray imaging devices allow for the formation of multiple simultaneous images with no resolution loss (figure 7.1b).

We are able to see more "colors" in X-rays than in visible light. The question that remains open is: what is color for X-rays?

In a similar way as different types of surfaces exhibit different reflection properties of visible light, different materials are characterized by different X-ray transmission properties. The X-ray spectrum reaching the detector pixel thus bears information on the material traversed by the radiation along its path from the source to the pixel.

Until recently, this information was completely lost, because X-ray detectors were only able to measure one integral value, be it the total deposited energy or, more recently, the total number of photons (the beam intensity). On the contrary, spectroscopic X-ray detectors give the possibility to measure the full energy spectrum, even if just coarsely binned, at single pixel level, which provides a handle to extract more significant knowledge on the material content of the sample than the one encoded in a simple grayscale radiograph.

Spectral information can be used to identify different materials and their distribution in the sample. If different colors are assigned to each material, color X-ray imaging is achieved.

The set of 3D X-ray imaging techniques exploiting energy information is called spectral Computed Tomography (CT). Spectral CT is a relatively new field, due to the fact that energy sensitive X-ray imaging detectors only appeared recently.

The main challenge in spectral CT is to answer the following question:

> What is the best way to process spectral information from a set of two-dimensional radiographs and realize color (i.e. material resolved) X-ray three-dimensional imaging?

The aim of this thesis has been to answer this question for a specific set of detectors, i.e. silicon sensors connected to the spectroscopic readout chips of the Medipix family. The work needed to reach this goal not only involves the

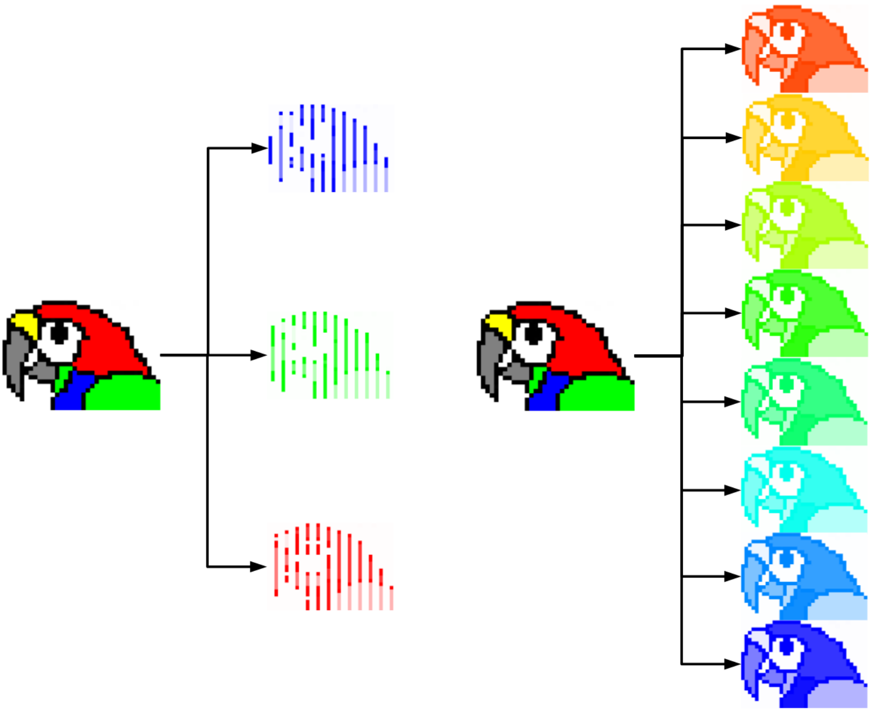

(a) **Human retina.** (b) **Medipix3 spectroscopic mode.**

Figure 7.1: **Image decomposition into color bases.**

implementation of dedicated image reconstruction algorithms capable of handling the spectral information measured by these detectors, but it also requires a precise characterization of the properties of the silicon sensor. This knowledge is necessary in order to implement the detector response in the reconstruction phase.

In the first place, a calibration method is developed, needed in order to define the detector energy scale. As monochromatic reference sources, the method exploits fluorescence X-ray radiation emitted from elements that are excited by the primary beam of an X-ray tube. A fitting procedure is designed to achieve an efficient calibration of single pixels, which is crucial to correct for variations due to inter-pixel mismatches and to reach an equal response of the full detector.

To understand how an incoming X-ray spectrum is distorted due to detector effects, the energy response function of the sensor has to be known. The strategy adopted in this thesis is to reach this result with a fully measurement based approach, in order to avoid biasing errors from the introduction of physics constants and to avoid the need to calculate the electric field configuration, which would require the precise knowledge of the doping profile of the sensor.

The measurement of the detector response function has been performed through a test beam with relativistic charged particles and a synchrotron test beam. Charged particles are used to study the transport properties of the sensor. Exploiting the energy information provided by the pixel readout, the energy deposition as a function of different positions in the pixel volume is determined. This information is used to extract the evolution of the charge profile as a function of the drift distance. The particle beam is thus used as a micro-probe to look at charge diffusion at microscopic level.

This information is exploited to implement a numerical framework for the calculation of the detector energy response function. The synchrotron test beam is needed to determine the values of the parameters of this model by comparing the calculations with measurements. Using monochromatic synchrotron radiation at different energies, the energy response function of the detector is measured directly over a wide spectral range.

The energy response function is used to calculate the detected spectrum, given an input spectrum coming from the transmission of an X-ray beam through an object. This step is crucial for the implementation of a spectral CT reconstruction algorithm suited for data taken with Medipix based silicon detectors.

As a proof of principle, an algorithm is derived by extending a conventional iterative method in order to incorporate spectral information. The algorithm, as formulated at this stage, is only applicable to a limited subset of sample geometries. Nonetheless, the results not only show an example of material resolved X-ray CT, but they also show the benefits arising from spectral CT with respect to conventional CT. The quality of the reconstruction improves as beam hardening artifacts are eliminated, which typically appear if spectral information is not accounted for.

To obtain a more efficient implementation, a statistical reconstruction algorithm is developed, based on a maximum likelihood principle. First results on simulated data show the validity of the method and hint at the necessity to further develop this research line in order to exploit the full potential of the Medipix chip (and similar technologies) in X-ray imaging applications. The algorithm is implemented using tools developed for the statistical treatment of large amount of data from high energy physics, thus giving a demonstration of how fundamental research can be exported to applications in other fields.

Although the results are derived only for a very specific type of detector operated in a specific state (a 300 μm silicon sensor read out by a Medipix chip and operated at 100 V bias) these devices, at these operating conditions, are standard for the majority of the applications. The results, and especially the methods, have thus a more general validity. First applications in several fields, including medical, are not far away. The general belief is that once fully understood and established, spectral CT will surely have a considerable impact in the field of X-ray imaging.

Enrico Junior Schioppa
Amsterdam
30 November 2014

Samenvatting

> *Het netvlies van het oog is niet gevoelig voor deze straling: het oog dat vlak voor het apparaat wordt gehouden ziet niks.*
>
> W. C. Röntgen, 1895 [62].

Professor Röntgen noemde de straling "X-straling", omdat, zoals hij zei: *kortheidshalve*, en waarschijnlijk om het te benadrukken, *lichamen reageren hetzelfde op X-straling als troebele media reageren op licht.* Behalve deze waarneming wist hij heel weinig over de aard van dit verschijnsel. Zelfs zo weinig dat hij er geen moeite mee had om zijn ogen vlak voor een bron te plaatsen, die behoorlijk krachtig is geweest, aangezien *een deel van de straling door 2 mm dik platinum heen kwam.* Tegenwoordig zijn we goed op de hoogte van de gevaren van deze X-straling, of Röntgenstraling, en stralingsbeschermingdiensten werken hard om dergelijke voorvallen te voorkomen.

Professor Röntgen was de eerste die Röntgenstraling wilde detecteren met een energiegevoelige pixeldetector: het menselijk oog. Natuurlijk kon hij niks zien, omdat de retina totaal niet gevoelig is voor Röntgenstraling. De technologie die nodig is om pixeldetectoren te maken die gevoelig zijn voor Röntgenstraling is 100 jaar later beschikbaar. Deze detectoren zijn gemaakt door een halfgeleidende pixelsensor te verbinden met een uitleeschip die energie gevoelig is. De detectoren kunnen worden gebruikt om gekleurde (de kleur correspondeert met de materiaalsamenstelling) Röntgenfoto's te maken.

Het principe van kleurherkenning op het netvlies is gebaseerd op de aanwezigheid van drie type "pixels", de kegelreceptoren. Elk type receptor is gevoelig voor een andere golflengte. Het inkomende licht wordt gefilterd door elke receptor en het beeld wordt ontleed op basis van drie kleuren (rood, groen en blauw, zie figuur 7.2a).

De pixelchips werken volgens een ander concept. De gebruikte pixelchips voor Röntgendetectoren zijn in staat om, op pixelniveau, het binnenkomende stralingsspectrum te scheiden in meerdere energieniveaus. In het netvlies worden er drie beelden in verschillende kleuren gemaakt, waarbij de ruimtelijke resolutie vermindert (één van de drie receptoren wordt gebruikt voor elk beeld), terwijl bij de pixel chips verschillende beelden tegelijk gemaakt kunnen worden, zonder verlies van ruimtelijke resolutie (figuur 7.2b).

We zijn in staat om meer "kleuren" te onderscheiden in Röntgenstraling dan in zichtbaar licht. Maar de vraag blijft: wat betekent kleur voor Röntgenstraling?

Zoals verschillende oppervlakten het zichtbare licht verschillend reflecteren, zo zijn verschillende materialen gekenmerkt door verschillende Röntgenstraling transmissie eigenschappen. Het spectrum van de Röntgenstraling dat de pixels van de detector bereikt, geeft dus informatie over het materiaal waardoor de straling is gegaan gedurende de reis van de bron naar de detector.

Tot voor kort ging deze informatie volledig verloren, omdat Röntgen detectoren alleen één integrale waarde konden meten. Dit was ofwel de totale afgegeven energie, of, recenter, het aantal fotonen (de intensiteit van de bundel). Spectroscopische Röntgen detectoren, daarentegen, hebben de mogelijkheid om het volledige energie spectrum te meten. Zelfs als de data op pixelniveau wordt opgeslagen, kunnen deze detectoren een beter idee geven van de materialen waaruit het monster bestaat, dan de Röntgenfoto's in grijstinten.

Informatie over het spectrum kan gebruikt worden om verschillende materialen in het monster te identificeren en om iets te zeggen over de distributie van deze materialen. Als elk materiaal een andere kleur krijgt toegewezen, leidt dit tot gekleurde Röntgendiagnostiek.

Alle technieken die 3D Röntgenfoto's maken en die daarbij gebruik maken van de informatie over het energie spectrum van de bundel, worden samen spectraal Computer Tomografie (CT). Spectraal CT is een relatief nieuw onderzoeksgebied, omdat energie gevoelige Röntgen detectoren pas recentelijk zijn verschenen.

De grootste uitdaging in spectraal CT is om antwoord te vinden op de volgende vraag:

> Wat is de beste manier om een set van twee dimensionale Röntgenfoto's te verwerken, zodat er een gekleurde drie dimensionale Röntgenfoto

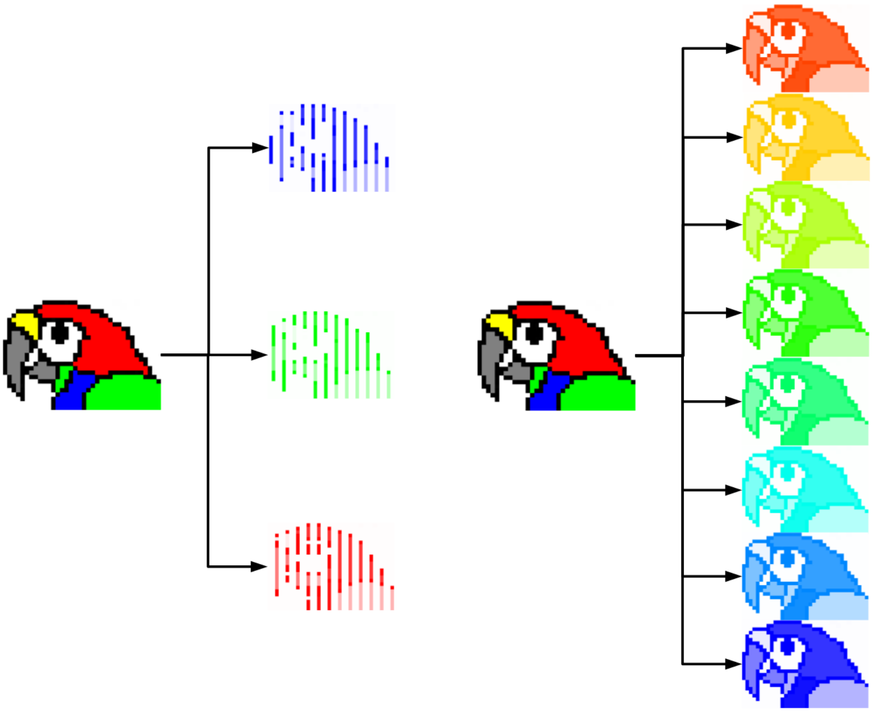

(a) **Het menselijk netvlies**

(b) **Medipix3 spectroscopische modus.**

Figure 7.2: **De ontleding van beelden in verschillende kleuren.**

kan worden gemaakt?

Het doel van dit proefschrift is om deze vraag te beantwoorden voor een specifiek type detectoren: siliciumsensoren die verbonden zijn met de spectroscopische uitleeschips uit de Medipix familie. Om dit doel te bereiken moet er niet alleen een algoritme worden toegevoegd dat in staat is om de informatie over het energie spectrum te verwerken, maar moet er ook onderzocht worden wat de eigenschappen van de silicium sensoren zijn. Deze kennis van de sensoren is nodig om de detectorrespons toe te voegen tijdens de reconstructie.

Allereerst is er een kalibratiemethode ontwikkeld om de energieschaal van de detector te kunnen definiëren. Als monochromatische bron wordt fluorescentie gebruikt: karakteristieke straling die wordt uitgezonden door elementen als deze zijn geëxciteerd door de primaire bundel van de Röntgenbuis. Er is een model ontwikkeld om een efficiënte kalibratie op pixel niveau te bereiken. Dit is cruciaal om de verschillen tussen de pixels te kunnen corrigeren en om een gelijke respons te krijgen van de gehele detector.

Om te kunnen begrijpen hoe een inkomend spectrum van de Röntgenstraling verandert door de detector, moet de energierespons-functie van de sensoren bekend zijn. Om dit te bereiken wordt er in dit proefschrift gebruik gemaakt van een op metingen gebaseerde methode. Hierdoor is het mogelijk om onzekerheden in fysische constanten te vermijden en is het niet noodzakelijk om de configuratie van het elektrische veld te berekenen.

De meting van de detectorrespons-functie is gedaan met een testbundel met relativistische, geladen deeltjes en met een synchrotron testbundel. Geladen deeltjes zijn gebruikt om de transporteigenschappen van de sensor te bestuderen. Door de informatie over de energie te gebruiken, kan de afgeleverde energie worden per pixel. Deze informatie wordt gebruikt om de ontwikkeling van het ladingsprofiel als functie van de driftafstand af te leiden. De testbundel wordt dus gebruikt als microsonde om te kijken naar ladingsdiffusie op microscopisch niveau.

De informatie over het ladingsprofiel wordt gebruikt als een numerieke structuur voor de berekening van de detectorrespons-functie. De synchrotron testbundel is nodig om de parameters voor dit model vast te stellen. Dit wordt gedaan door de berekening te vergelijken met metingen. De energierespons-functie van de detector kan gemeten worden over een groot energiespectrum door gebruik te maken van monochromatischesynchrotron straling van verschillende energieën.

Met de energierespons-functie is het mogelijk om het gedetecteerde spectrum te berekenen, uitgaande van het spectrum dat wordt gegenereerd door de transmissie van een Röntgenbundel door een object. Deze stap is cruciaal voor de implementatie van een spectraal CT reconstructie-algoritme dat geschikt is voor het nemen van data met siliciumdetectoren gebaseerd op Medipix.

Om te bewijzen dat deze procedure werkt, wordt een algoritme afgeleid waarvoor een bestaande iteratieve methode wordt uitgebreid met de informatie over het spectrum. Op dit moment is het algoritme alleen geschikt voor een beperkt aantal geometrieën van het monster. Toch laten de resultaten niet alleen een voorbeeld van spectrale Röntgen CT zien, maar laten ze ook de voordelen van spectraal CT boven de conventionele CT zien. De kwaliteit van de reconstructie verbetert door gebruik te maken van de informatie over het energie spectrum.

Om de implementatie van deze methode efficiënter te maken, is er een statistisch reconstructie algoritme ontwikkeld, op basis van de meest aannemelijke schatting. De eerste resultaten op gesimuleerde data laten de validiteit van deze methode zien en duiden aan dat het noodzakelijk is om deze methode verder te ontwikkelen om zo de volledige potentie van de Medipix chip (en andere vergelijkbare technieken) te kunnen benutten voor het maken van afbeeldingen met Röntgenstraling. Het algoritme is toegepast door gebruik te maken van methodes uit de hoge-energiefysica, waarbij grote hoeveelheden data met een statistische methode worden verwerkt, en toont hiermee aan hoe fundamenteel onderzoek gebruikt kan worden in toepassingen in andere velden.

Hoewel de resultaten alleen zijn afgeleid voor een specifiek type detector, gebruikt in een bepaalde toestand (een silicium sensor van 300 μm dik, uitgelezen door een Medipix chip en met een 100 V bias) is dit een veelgebruikte configuratie en vormt de standaard voor het grootste gedeelte van de toepassingen. De resultaten, en voornamelijk de gebruikte methodes, hebben een algemenere validiteit. De eerste toepassingen in verschillende velden, ook voor medische toepassingen, zijn niet ver weg. In het algemeen wordt aangenomen dat spectraal CT een grote invloed zal krijgen op het gebied van Röntgendiagnostiek.

Enrico Junior Schioppa
Amsterdam
30 November 2014